2-1-2016

A study of Asphalt Aging Behavior Using Molecular Dynamics Simulations

Jielin Pan

Jielin Pan
Candidate

Civil Engineering
Department

This dissertation is approved, and it is acceptable in quality and form for publication:

Approved by the Dissertation Committee:

Dr. Rafiqul Alam Tarefder, Chairperson

Dr. Yu-Lin Shen

Dr. Tang-Tat Ng

Dr. Guohui Zhang

A STUDY OF ASPHALT AGING BEHAVIOR USING MOLECULAR DYNAMICS SIMULATIONS

by

JIELIN PAN

B.Eng. (Mineral Resource Engineering), Wuhan University of Technology, 2008
M.Eng. (Mining Engineering), Wuhan University of Technology, 2011

DISSERTATION

Submitted in Partial Fulfillment of the
Requirements for the Degree of

Doctor of Philosophy
Engineering

The University of New Mexico
Albuquerque, New Mexico

December, 2015

DEDICATION

This dissertation is dedicated to my always encouraging, ever loving parents, Xiuling Pan and Ying Tang who led me to pursue a PhD degree, my faithful, loving and supportive husband, Changyi Li who never left my side, and our exuberant, sweet and kind-hearted little son, Albert Pan Li who filled my PhD study with full of amusement.

This dissertation is also dedicated to my American host family, my loving American parents, Regan and Susan Stinnett who have supported me throughout the entire doctoral program.

ACKNOWLEDGEMENTS

Firstly, I would like to express my sincere gratitude to my advisor Dr. Rafiqul A. Tarefder for his support of my PhD study and related research, for his outstanding mentorship and motivation. Dr. Tarefder taught me how to think critically and express ideas. Special thanks to him for encouraging me to grown as an independent thinker and giving me the freedom to explore on my own, and at the same time the guidance to recover when my steps faltered. Without his guidance and persistent help this dissertation would not have been possible.

Besides my advisor, I would like to gratefully and sincerely thank the rest of my dissertation committee: Dr. Yu-Lin Shen, Dr. Tang-Tat Ng, and Dr. Guohui Zhang, for their insightful comments and encouragement, but also for the hard question which incented me to widen my research from various perspectives.

I would also like to express my gratitude to the National Science Foundation (NSF) research project funding for initiating and supporting this research project and the New Mexico Department of Transportation (NMDOT) for continuing supporting my PhD study and research through their funding since I worked in one of their project about the field and laboratory evaluation of Warm Mix Asphalt (WMA). Special thanks go to the Department of Civil Engineering for supporting my last semester's PhD study by granting me the Civil Engineering Emeriti Fellowship.

My sincere thanks also go to the professors and staff at the University of New Mexico. Dr. Mahmoud R. Taha has been especially supporting and encouraging me through the

process. Dr. Julie E. Allred Coonrod, Dr. Walter Gerstle and Dr. John C. Stormont helped and guided me a lot in the PhD Qualifying Exam, who served on my exam committee. Josie Gibson, Nicole Bingham, Yolanda Sanchez, Rebekah Lucero, Marcus Panozzo, Brianne Lucero, Alicia Martinez and Ambrose Martinez have been especially kind in taking care of administrative needs and always providing me with a smile. Kenny Martinez was really helpful for arranging laboratory supplies. My special thanks go to Hope McVeety for her endless efforts on editing my journal and conference papers. She not only taught me how to write technical papers but also taught me how to be a better person.

I thank my colleagues and friends during my PhD study. Umme A. Mannan, Hansan Faisal and Mohiuddin Ahmad helped me a lot for Dynamic Shear Rheometer (DSR), nanoindentation and pyconometer testing, respectively, who helped me to eventually get to this point. Md R. Isam and Mesbah U. Ahmed also provided me many suggestions for my PhD study. Special thanks go to Dr. Mohammad I. Hossain for his help and suggestions for my research, and Dr. Mekdim Weldegiorgis and Naomi R. Waterman for their encouragements. Thank my Chinese friends Qiong Wu and Cong Chen for their support and suggestions during my PhD study.

Last but not the least, I would like to thank my family: my parents, my husband, my son and my American host family for supporting me spiritually throughout the PhD program and my life in general. This research work would not be completed without their encouragement and belief in me.

A Study of Asphalt Aging Behavior Using Molecular Dynamics Simulations

by

Jielin Pan

B.Eng. (Mineral Resource Engineering), Wuhan University of Technology, 2008

M.Eng. (Mining Engineering), Wuhan University of Technology, 2011

Ph.D. (Engineering), The University of New Mexico, 2015

ABSTRACT

Oxidative aging is a major issue in asphalt pavements that leads to hardening of the asphalt, which further contributes significantly to asphalt pavement embrittlement and eventually results in excessive pavement cracking. In addition, the performance of asphalt binder is also highly related to its service conditions which involve climatic conditions and traffic conditions, such as temperature, moisture and traffic loads. Generally, the mechanical properties of asphalt before and after oxidative aging can be tested in the laboratory; however, the fundamental material science of asphalt before and after oxidative aging is difficult to be investigated in the laboratory regarding chemical composition and property change due to the difficulties of studying the molecular structures and their dynamic behavior in asphalt. Therefore, Molecular Dynamics (MD) simulation method is used in this study to understand how the chemical composition and property changes of asphalt after oxidative aging affect the physical, thermodynamic, rheological and mechanical performance of the asphalt, and how the oxidized asphalt acts

under different conditions, such as loading, temperature, and moisture, compared to the unoxidized asphalt. MD simulation is a computational method used to simulate the physical movements of atoms and molecules depending on time and force field chosen under different conditions, such as temperature, pressure, and loading.

Asphalt models before and after oxidative aging are developed for MD simulations in this study under different temperatures, loading and moisture contents. Simulation results show that the oxidized functional groups in asphalt molecules increase the strength of intermolecular bonds of asphalt, which further contributes to the hardening of the oxidized asphalt. Specifically, the internal energy changes, especially for higher magnitude of intermolecular and lower kinetic energies, are responsible for the hardening of oxidized asphalt, and the higher potential energies and for oxidized asphalt further proves that oxidation increases the polarity of molecules in asphalt and forms strongly interacting components. The internal property change is consistent with the external physical and rheological property change after oxidation, which is revealed by the increase of density, bulk modulus and viscosity.

Considering the mechanical property of asphalt using MD simulations, both the unoxidized and oxidized asphalts deform more and fail faster with an increase in both compressive and tensile stress rates, especially under tensile stresses. However, the oxidized asphalt is stiffer than the unoxidized asphalt, which shows slower and less deformation, further validating the hardening of asphalt after oxidation.

Asphalt is significantly susceptible to temperature. Simulation results show that density, and zero shear viscosity of asphalt decrease with an increase in temperature. Isothermal

compressibility and bulk modulus also change under different temperatures. Moreover, the density, bulk modulus (inverse of isothermal compressibility) and zero shear viscosity of oxidized asphalt is higher than the unoxidized asphalt proving the hardening of asphalt during oxidation. The different change trends of isothermal compressibility and bulk modulus between unoxidized and oxidized asphalts under different temperatures indicate glass transition behavior changed after asphalt oxidation.

According to MD simulations, the moisture impacts on asphalt before and after oxidative aging are significant regarding bulk modulus and zero shear viscosity. Both bulk modulus and zero shear viscosity of asphalt decrease with an increase in moisture content in the asphalt. Moreover, moisture adversely impacts more on oxidized asphalt. The moisture impact on the density of asphalt before and after oxidation is not significant. Density of oxidized asphalt is constantly higher than the unoxidized asphalt under different moisture contents and the density fluctuations of oxidized asphalt is larger. This indicates that asphalt is more sensitive to moisture inclusion after oxidative aging.

Laboratory tests are used to validate MD simulation results. Pycnometer method, Dynamic Shear Rheometer (DSR) and nanoindentation are used to test density, zero shear viscosity, and nanomechanical properties including modulus, hardness and viscosity of asphalt binders with different degree of oxidative aging, respectively. Laboratory testing results are consistent with MD simulation results.

TABLE OF CONTENTS

LIST OF FIGURES

LIST OF TABLES

CHAPTER 1

INTRODUCTION

1.1 Problem Statement

Asphalt, also known as bitumen, is a petroleum product obtained by the distillation of crude oil and is widely used as a binder for roadway construction. Asphalt is a complex mixture of organic molecules that vary widely in composition from nonpolar saturated hydrocarbons to highly polar and highly condensed aromatic ring systems (Petersen 1984). The underlying chemical composition and chemical properties of the composition directly determine the physical properties of asphalt (Greenfield 2011). In other words, the stability and structure of asphalt's underlying chemical components directly determines the durability and serviceability of asphalt pavement.

In reality, there are two major chemical factors that affect asphalt's durability. They are (i) compatibility of the interacting components in asphalt and, (ii) the resistance of its molecules' chemical composition to change when reacting with atmospheric oxygen (Petersen 1984). The latter is also called oxidative aging that leads to hardening of the asphalt, which further contributes significantly to asphalt pavement embrittlement and eventually results in excessive pavement cracking (Tarefder and Yousefi 2015; Tarefder and Faisal 2013c).

The performance of asphalt binder is also highly related to its service conditions which involve traffic and climatic conditions, such as traffic loads, temperature, and moisture (Hossain and Tarefder 2013; Islam et al. 2015; Mannan et al. 2015). Specifically, the size

of traffic loading affects the strength of asphalt pavement, which causes asphalt deformation and eventually results in asphalt pavement cracking. Moreover, the physical, rheological and mechanical properties of asphalt changes with temperature variations, since asphalt, whether aged or not, is a thermoplastic material. This characteristic is quite significant during asphalt and aggregate mixing to guarantee adequately coating of the mixtures, and during asphalt pavement compaction to reach optimum pavement density. More importantly, the thermoplastic property is attributed to the rutting and cracking resistance of asphalt pavement (Nicholls 1998). Moisture damage is as well a major damage for asphalt pavement, which is caused by water penetrating into the asphalt-aggregate system and results in rheological property change of the asphalt binder, which shortens the binder's service life and debonds the asphalt from aggregates to accelerate pavement distresses (Chindaprasirt et al. 2009; Ma et al. 2011).

Therefore, it is important to understand how oxygen reacts with molecules in asphalt, how the oxidation products change the microstructures of asphalt and how the internal molecular interactions before and after oxidative aging in asphalt affect its external physical, thermodynamic, rheological and mechanical properties under different loads, temperatures, and moisture contents.

Because oxidation occurs at molecular scale, which is often difficult to capture using laboratory scale testing, however, it is suitable to be studied using molecular dynamics (MD) simulation method. MD simulation is a computational method used to simulate the physical movements of atoms and molecules depending on time and force field chosen under different conditions, such as temperature, pressure, and loading. This method can

be used to find the relationship between the chemical property change and the physical property change of asphalt systems before and after oxidative aging.

1.2 Hypothesis

1.2.1 Hypothesis One

It was observed that oxidative aging increased the viscosity and hardness of asphalt (Petersen and Glaser 2011). The physical properties of materials such as viscosity and hardness are related to the strength of attractive forces called intermolecular forces (Brown et al. 2011; Gilman 2009). It can be hypothesized that the intermolecular interactions in the asphalt systems govern the physical properties of asphalt before and after oxidative aging. Therefore, if oxidized asphalt shows an increase of viscosity after MD simulation, the magnitudes of intermolecular energies underlying the asphalt systems should increase while the kinetic energy should decrease.

1.2.2 Hypothesis Two

Asphalt pavement is subjected to traffic loading during service life. The asphalt concrete (AC) layer suffers from both compression and tension due to traffic loading as shown in Figure 1.1. Therefore it is important to understand the response of asphalt to different compressive and tensile stresses before and after oxidative aging. It can be hypothesized that both the unoxidized and oxidized asphalts deform more and fail faster with an increase in both compressive and tensile stress rates, especially under tensile stresses. It is hypothesized that the oxidized asphalt is stiffer than the unoxidized asphalt, which shows less deformation.

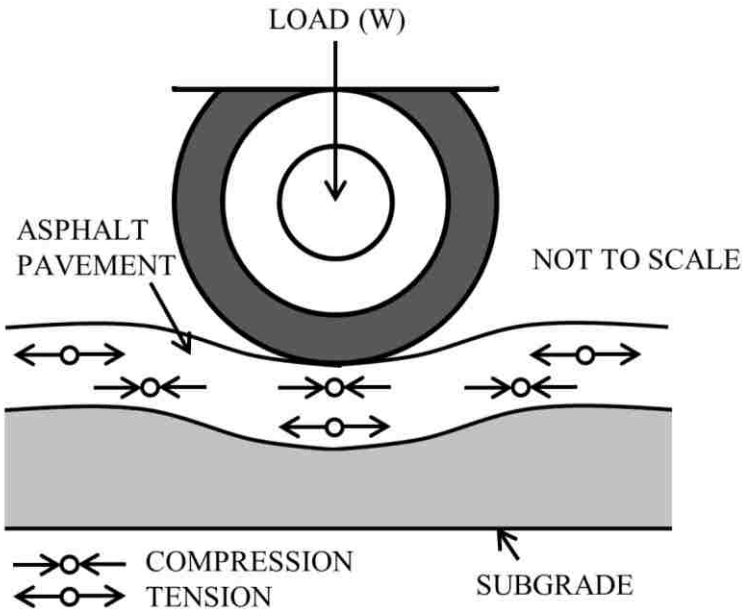

Figure 1.1 Effects of traffic loading on AC layer

1.2.3 Hypothesis Three

Asphalt is a temperature susceptible material and its physical properties change with the change of temperature. The responses of asphalt's thermodynamic properties to temperature before and after oxidation have not been comprehensively studied in terms of density, isothermal compressibility and bulk modulus. Moreover, the density of asphalt is important for the compaction of the asphalt-aggregate mixtures to achieve optimum density during paving construction. In addition, the glass transition behavior of asphalt can be interpreted by significant density, isothermal compressibility and bulk modulus change of asphalt under certain temperature range. It can be hypothesized that the density of asphalt decreases with an increase of temperature and the density of oxidized asphalt is higher than the unoxidized asphalt. Moreover, glass transition behavior of asphalt changes after oxidation due to the change of isothermal compressibility and bulk

modulus. It is hypothesized that the oxidized asphalt possesses lower isothermal compressibility and higher bulk modulus than the unoxidized asphalt.

1.3.4 Hypothesis Four

A major concern of asphalt pavement is moisture damage (Hossain and Tarefder 2013; Ma et al. 2011), which is caused by water penetrating into the asphalt-aggregate mixture and results in rheological property changes of asphalt binder that shorten binder's service life and accelerate pavement distresses (Chindaprasirt et al. 2009). Many attempts have been done to research the response of asphalt-aggregate mixture to moisture damage but few researches on evaluating the moisture effect on asphalt binder after oxidative aging. Therefore, this study is also focused on how the moisture affects the properties of oxidized asphalt, compared to the unoxidized asphalt by adding different percentages of water molecules into the model asphalt systems. It can be hypothesized that the moisture inclusion results in rheological property changes of asphalt: the density and viscosity of asphalt binder decrease with an increase of moisture content. Moreover, moisture brings more damage on the oxidized asphalt by decreasing its viscosity and density faster than the unoxidized asphalt.

1.3 Dissertation Organization

The dissertation consists of eight chapters. The organization of dissertation is as follows:

Chapter 1: The problem statement and hypotheses are presented.

Chapter 2: The current pool of literature on asphalt chemistry, modeling methods, and the studies related to asphalt using MD simulations is reviewed.

Chapter 3: The methodology of MD simulation and simulation parameter selections are explicated.

Chapter 4: The energy changes of asphalt before and after oxidative aging are studied.

Chapter 5: The mechanical properties of asphalt under different stress rates before and after oxidative aging are investigated.

Chapter 6: The asphalt property changes under different temperatures before and after oxidative aging are stated.

Chapter 7: The moisture impacts on asphalt before and after oxidative aging are discussed.

Chapter 8: The conclusions of this study are summarized and recommendations for further study are provided.

CHAPTER 2

LITERATURE REVIEW

2.1 Asphalt Chemistry and Structure

2.1.1 Definitions and Manufacture

Asphalt is defined as a "virtually involatile, adhesive and waterproofing material derived from crude petroleum, or present in nature asphalt, which is completely or nearly completely soluble in toluene, and very viscous or nearly solid at ambient temperatures" (European Committee for Standardization 2000). Currently, asphalt is essentially obtained by the distillation of crude oil and only one tenth of the available petroleum is found suitable for yielding sufficient amounts of asphalt, the heavier the crude oil, the higher its asphalt yield (Corbett 1965; Read and Whiteoak 2003).

The typical distillation process consists five steps as shown in Figure 2.1. The first step is separating the light components from the crude oil by atmospheric distillation at 350 ℃. The residue from the atmospheric distillation is further refined at a slightly higher temperature with a range of 350-425 ℃ and under vacuum with pressures of order 1-10 kPa, in a second step. The vacuum residue of the crude oil is the final asphalt product. The properties of the resulting asphalt depend on the crude origin and actual operating conditions (Read and Whiteoak 2003; Speight 1999).

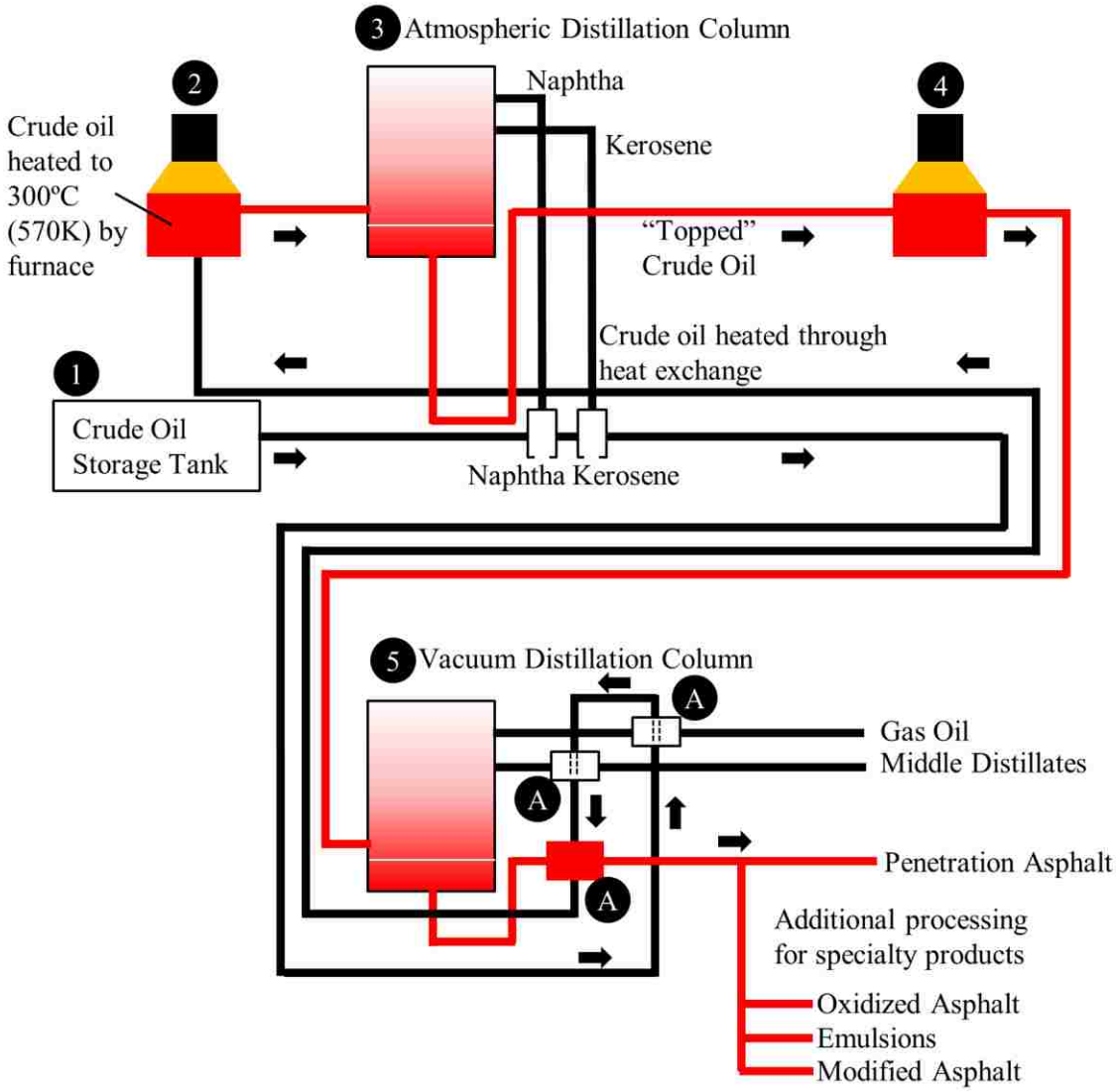

Figure 2.1 Typical distillation process of asphalt (Lesueur 2009)

2.1.2 General Physical and Chemical Properties

Asphalt density depends on its hardness, the harder it is, the denser the asphalt (Read and Whiteoak 2003). The glass transition of an asphalt varies in a very wide range from 5 ℃ down to -40 ℃ essentially based on the crude origin and slightly less on the manufacture process. The transition range generally spans 30 ℃ to 45 ℃, and -20 ℃ usually corresponds to the midpoint value (Claudy et al. 1992; Jiménez-Mateos et al. 1996;

Schmidt and Santucci 1966; Turner and Branthaver 1997). For that reason, asphalt is a very viscous liquid at room temperature from a thermodynamic perspective.

The elemental composition of an asphalt varies from its crude source. However, asphalt mainly consists in carbon (80-88% by weight) and hydrogen atoms (8-12% by weight). Moreover, heteroatoms such as sulfur (0-9% by weight), nitrogen (0-2% by weight) and oxygen (0-2% by weight) are generally present along with traces of metals such as vanadium (up to 2000 parts per million) and nickel (up to 200 parts per million) (Branthaver et al. 1993; Jiménez-Mateos et al. 1996; Mortazavi and Moulthrop 1993; Read and Whiteoak 2003; Speight 1999). To understand the properties of asphalt, researching asphalt chemistry on a general basis is not sufficient. Thus, molecules in asphalt usually separated into different chemical fractions, depending on their size and solubility in polar, aromatic or non-polar solvents (Lesueur 2009).

2.1.3 Components in Asphalt

With the advent of modern chromatographic methods, it is possible to separate asphalt into four chemical families. Generally, asphalt systems can be physically separated through the selective adsorption-desorption method which is proposed by Corbett (1969), according to different solubility classes. Figure 2.2 shows the schematic of Corbett's asphalt separation method. Asphalt systems are first separated into two broad groups: asphaltenes and maltenes, which are the dispersed phase and the continuous phase, respectively. Maltenes then can be further divided into a series of fractions with increasing polarity: saturates, aromatics also known as naphthene aromatics, and resins also known as polar aromatics (Lu and Wang 2010; Petersen 1984). The four fractions of

asphalt are also called SARA (Saturates, Aromatics, Resins and Asphaltenes). Nowadays, the American Society for Testing and Materials (ASTM) proposed a method similar to the Corbett procedure, which employs other solvents for asphalt separation that are preferred for safety reasons and convenience. The reference method is the ASTM D-4124 as shown in Figure 2.3 (ASTM International 2009a). Details of the four fractions in the asphalt systems are presented as follows.

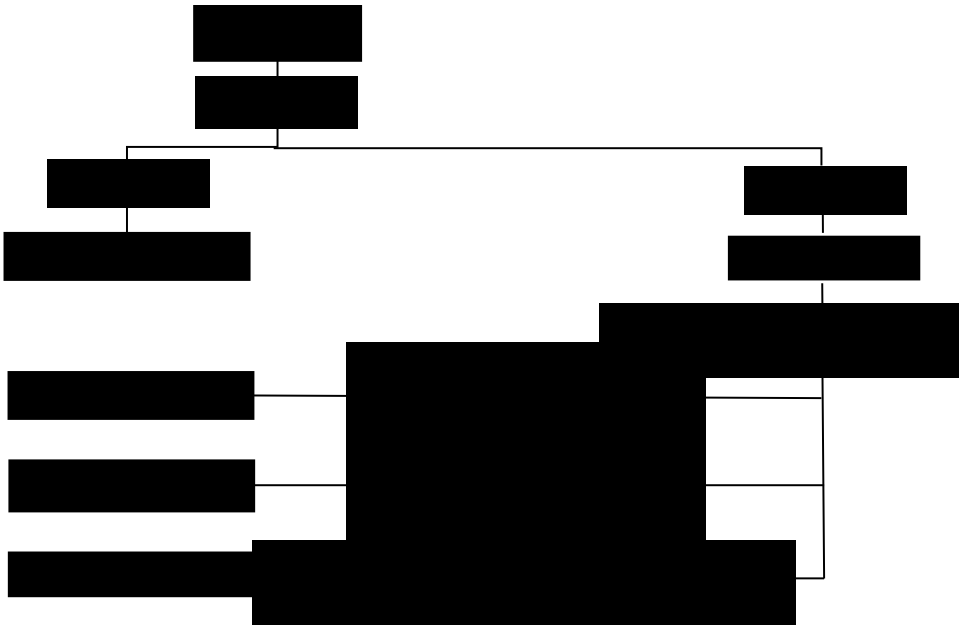

Figure 2.2 Schematic of Corbett's (1969) asphalt separation method

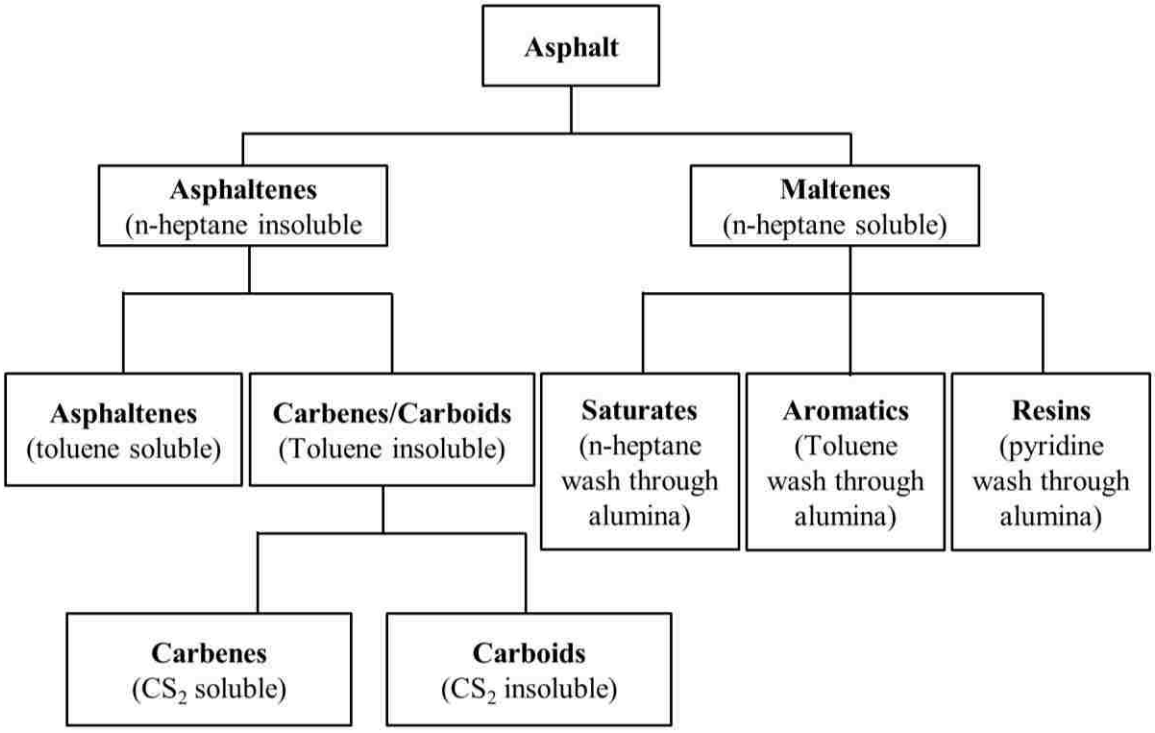

Figure 2.3 Schematic of ASTM method for asphalt separation (ASTM International 2009a)

2.1.3.1 Maltenes – Saturates

Saturates are composed of alkanes including normal (n-paraffins), branched (iso-paraffins), and cyclic alkanes (naphthenes), which are colorless or lightly color liquid at room temperature and usually amount for 5-15% by weight of a paving grade asphalt (Corbett 1969). The glass transition temperature of saturates is approximately -70 ℃, which is typically 40 ℃ lower than the parent asphalt. Saturate fraction lacks polar chemical functional groups and rarely changes with time (Roberts et al. 1996).

2.1.3.2 Maltenes – Aromatics

Aromatics, also called naphthene aromatics, are composed of condensed non-aromatic rings and at least one aromatic ring structure similar to benzene. Aromatics are most abundant components in an asphalt with amount of 30-45% by weight (Corbett 1969). They are the softening components in asphalt, which are good solvents for paraffin waxes with light molecular weight hydrocarbons minimal polarity. Aromatics form a yellow to red liquid at room temperature (Corbett 1969). Compared to saturates, aromatics are rather more viscous at the same temperature due to a higher glass transition temperature approximately -20 ℃, which is similar to that of the parent asphalt (Claudy et al. 1992). Moreover, aromatics are the aging fraction in asphalt, which easily react with oxygen over time (Lira-Galeana and Hammami 2000; Roberts et al. 1996).

2.1.3.3 Maltenes – Reins

Resins, also called polar aromatics, consist of a much higher polar end group than the other fractions in maltenes. As aromatic fraction, resins are numerous with 30-45% by weight in asphalt. Heteroatoms such as oxygen, sulfur and nitrogen, as well as long, nonpolar paraffinic groups can also be found in resins. Resins form a black solid at room temperature (Corbett 1969). Moreover, it is still unclear that if resins exhibit a glass transition (Claudy et al. 1992). The resin fraction, as asphaltenes and aromatics, is also one of the aging fractions in asphalt (Lira-Galeana and Hammami 2000; Roberts et al. 1996).

2.1.3.3 Asphaltenes

Asphaltenes are the most polar and largest components and act as the viscosity-building ("bodying") agents in asphalt systems, which represent 5-20% by weight of a paving grade asphalt (Branthaver et al. 1993; Corbett 1969; Speight 2004). Therefore, they are the most reactive fraction in asphalt that has a very high tendency to interact and associate with oxygen. Asphaltenes are not only composed of condensed aromatic and naphthenic molecules, but also contain a large amount of heteroatoms including O, S, and N and metal content including V and Ni from heavy oils incorporated in their polar molecules (Lira-Galeana and Hammami 2000; Roberts et al. 1996). Asphaltenes present a black powder at room temperature and are essentially responsible for the black color of the asphalt (Corbett 1969). Mover, they do not exhibit any thermal transition in the normally concerned temperature range, which is up to 200 ℃ (Lesueur 2009).

2.1.4 Asphalt Structure

Lesueur (2009) reviewed the researches on the structure of asphalt and indicated that asphalt possesses a colloidal structure with asphaltenes micelles compassed by resin shells and entrapped in saturate and aromatic solvent. Figure 2.4 illustrates the colloidal structure of asphalt.

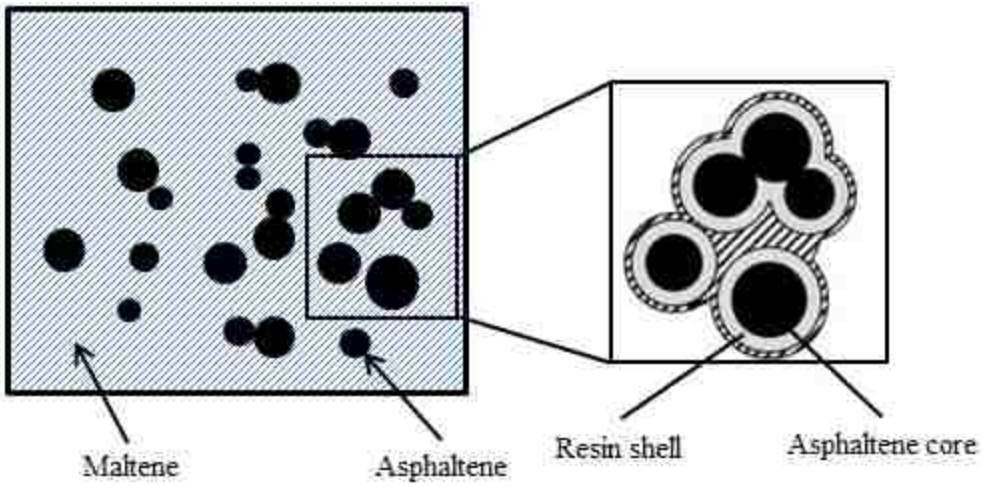

Figure 2.4 Colloidal structure of asphalt (Lesueur 2009)

Specifically, Small Angle X-Ray Scattering (SAXS) and Small Angles Neutrons Scattering (SANS) verify that asphaltenes form micelles in organic solvents, crude oil and asphalt (Bardon et al. 1996; Bodan 1982; Dwiggins 1965; Espinat et al. 1998; Henaut et al. n.d.; Mason and Lin 2003; Overfield et al. 1989; Ravey et al. 1988; Yen 1992). Moreover, viscoelastic studies also indicate that asphaltenes micelles are present in asphalt and they experience Brownian motion at high temperature (Lesueur et al. 1996, 1997). The colloidal structure is also proved by thermal analysis. Since asphalt undergoes a glass transition at a certain temperature very close to that of its aromatics and asphaltenes do not directly contribute to the glass transition as aforementioned, this strongly suggests that the asphaltenes are present as dispersed solid particles (Turner and Branthaver 1997). Among all the studies, diffusion experiment results are the most convincing evidence to confirm colloidal nature of asphalt, which show that an elementary structure existing in diffusive particles of radius 2-8 nm. This size corresponds to the crystal size of pure asphaltenes (Lesueur et al. 1997; Yen et al. 1961).

The resins, as the polar components in Maltenes, are believed to stabilize the asphaltene micelles. Koots and Speight (1975) confirmed that the asphaltenes would precipitate from the oily asphalt components (saturates and aromatics) without the resins, which are mainly responsible for preventing asphaltenes precipitation.

2.2 Oxidative Aging of Asphalt

2.2.1 Functional Groups in Asphalt

The analysis of asphalt oxidative aging can be narrowed down to a manageable number of types of functionalities, since many asphalt molecules of different composition have similar chemical functionalities that in turn cause similar effects on the physical properties of asphalt (Petersen 1986). According to Petersen's study (1984), when asphalt in pavements exposes to atmospheric oxygen, it rapidly oxidizes with the formation of polar, strongly interacting, oxygen-containing chemical functional groups that greatly increase viscosity and alter complex flow properties. The important chemical functionalities before and after aging are shown in Figure 2.5, which are an integral part of large asphalt molecules (Branthaver et al. 1993). The naturally existing functional groups in asphalt are shown in Figure 2.5 (a). The functional groups formed on oxidative aging are shown in Figure 2.5 (b).

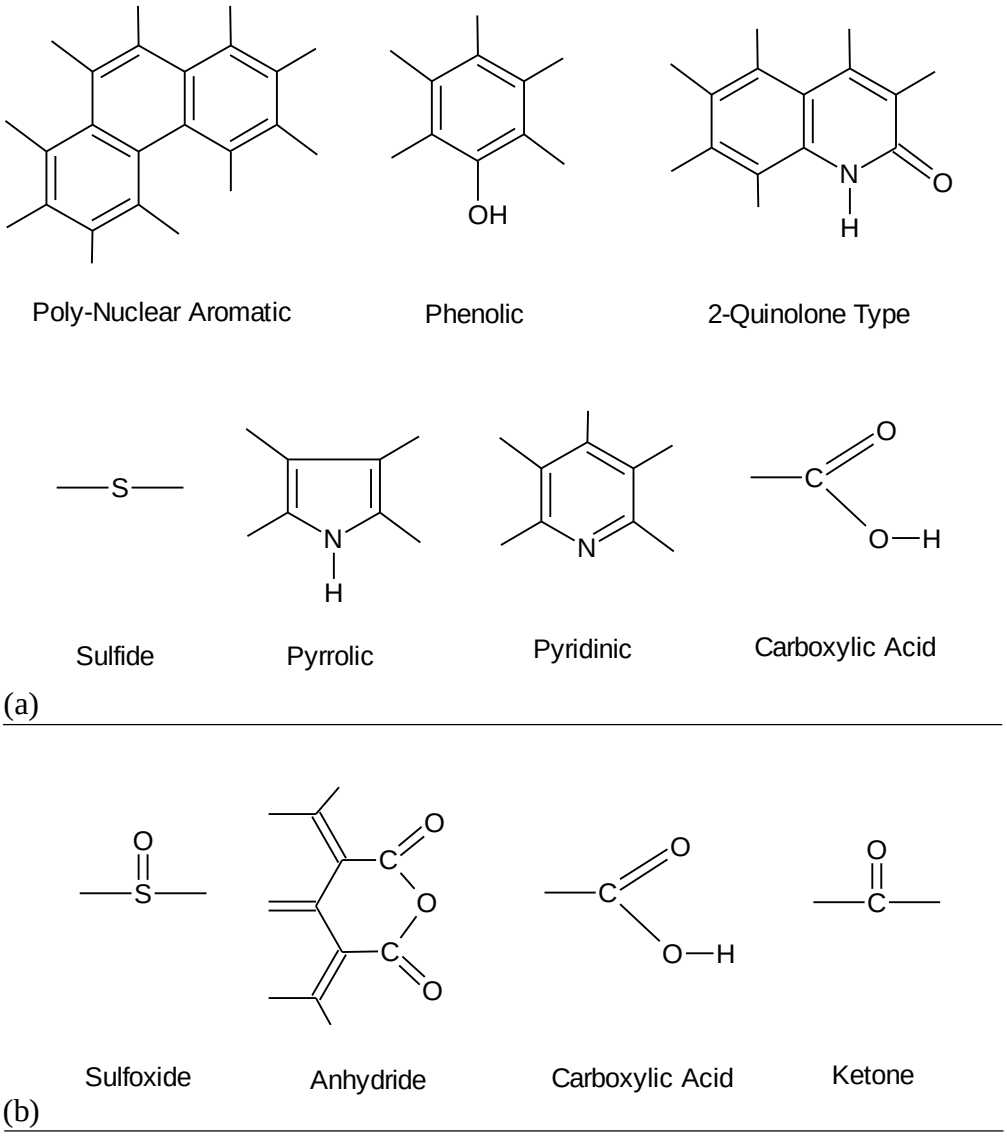

Figure 2.5 Important chemical functional groups in asphalt: (a) naturally existing functional groups and (b) functional groups formed on oxidative aging (Branthaver et al. 1993)

2.2.2 Dual Asphalt Oxidation Mechanism

According to Petersen and coworker's study, the oxidation products formed in asphalt are the general chemistry of hydrocarbon oxidation and are consistent and in good agreement with the hydrocarbon types (Petersen and Glaser 2011; Petersen 1984). The formation of

carbonyl compounds through the hydroperoxide intermediate is the major reaction pathway of hydrocarbon air oxidation (Petersen 1984). The kinetics of oxidation for all asphalts is similar, with an initial rapid reaction followed by a slower, constant rate reaction (Petersen and Glaser 2011). Ketones and sulfoxides are the major oxidation products produced at different rates for different asphalts and the amount of the products are highly source dependent (Branthaver et al. 1993). Specifically, the most sensitive hydrocarbon moiety present in asphalt is the carbon atom adjacent to an aromatic ring system – a benzylic carbon. The hydrogen atom attached to the benzylic carbon atom is relatively easy to displace by oxygen. The sulfur atoms in asphalt also account for most of the oxidative reactions. Generally, ketones formed at benzylic carbon atoms and sulfoxides formed at sulfur atoms (Pan et al. 2012a; b; Petersen 1984). Petersen and Glaser (2011) also suggested that the kinetics of ketones and sulfoxides produced corresponded to viscosity increase of asphalt.

As discussed above, asphalt oxidation experience a dual mechanism with an initial fast (spurt) reaction followed by a slow (long term) reaction. A condensed version of the chemistry of the dual asphalt oxidation mechanism is shown in Figure 2.6 (Petersen and Glaser 2011). It can be seen that during the spurt reaction stage, the oxidation products are mainly sulfoxides, while for the long term asphalt oxidation reaction, ketones and sulfoxides are both produced (Petersen and Glaser 2011).

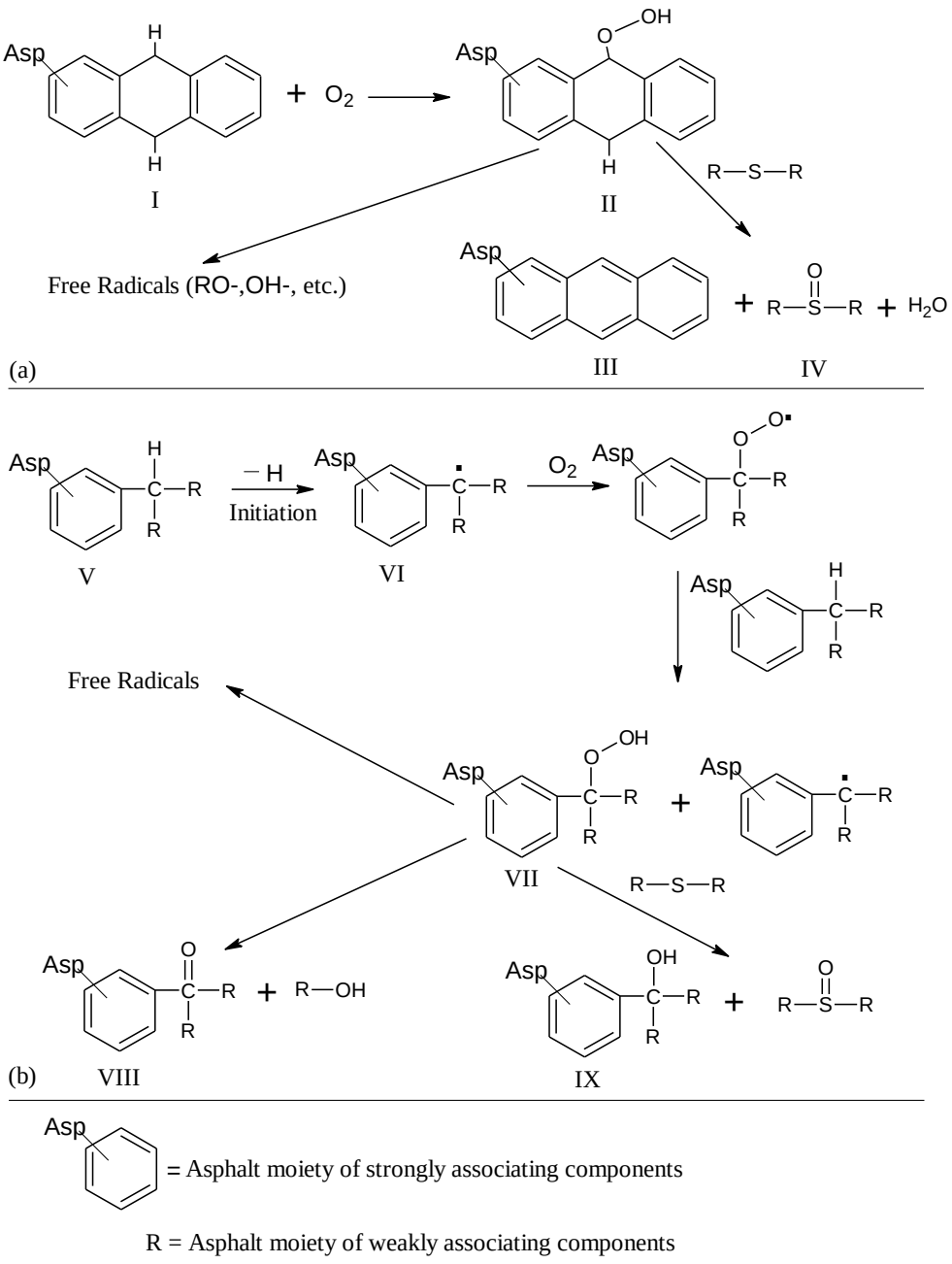

Figure 2.6 Dual asphalt oxidation mechanism: (a) fast (spurt) reaction and (b) slow (long term) reaction (Petersen and Glaser 2011)

2.3 Research Method Selection

2.3.1 Multi-Scale Modeling in Materials Science and Engineering

It is known to all that a multitude of materials-related phenomena are indispensable part of our daily life, whose essential role typically extends over many scales in time and space (E 2011). Materials are made up of electrons and atoms at the atomic scale, while meanwhile they are characterized by their own geometric dimensions that generally several orders of magnitude larger. Figure 2.7 illustrates the various techniques for the numerical simulation of a material with their corresponding characteristics length scales and time scale (Solar et al. 2012).

Figure 2.7 Schematic of Multi-Scale Modeling **(Solar et al. 2012)**

It can be seen that classical material mechanics such as finite element (FE) method is typically applied to continua and structures, which is concerned with the deformation of structures subjected to external mechanical forces. The material studied is considered as a continuous and homogeneous medium without gaps or empty spaces and is characterized on the macroscopic scale with the help of experimental tests to determine the mean behavior of the material. However, the heterogeneities of the material are usually neglected for the large system and long time scale simulations in order of meters and seconds, respectively (Solar et al. 2012; Zienkiewicz and Taylor 2000).

For this reason, the mechanics of a heterogeneous material is concerned using simulation methods in mesoscopic scale for predicting its macroscopic mechanical properties from heterogeneities in the microstructure. The material is seen as a continuous and heterogeneous medium with or without gaps or empty spaces and is characterized using mechanical tests on a representative volume element. The representative volume is the theoretically smallest volume of the material containing all information about the distribution and morphology of the heterogeneities in the material with periodic boundary conditions for solving homogenization problems (Besson et al. 2010). At the macroscopic level, the material is idealized as a continuous and homogeneous medium from the average mechanical behavior of the representative volume element. This type of technique takes into account heterogeneities but restricts to small systems in order of millimeter and micrometer such as discrete element method (DEM). Still, the analysis of the physical mechanics of a material lies at the hypothesis of the continuity of the material and the formalisms based on continuum mechanics and macroscopic thermodynamics due to the system size considered. Therefore, the molecular level and

microscopic thermodynamics of a material are disregarded by this technique (Solar et al. 2012).

All materials at the microscale are made up of the nuclei and the electrons, whose structure and dynamics are responsible for the macroscale behavior of the material. A proper linkage of electronic-structure, statistical, and mean-field theory is necessary to describe the physics and chemistry of a material that actually govern the properties and processes of the material under realistic temperature and pressure conditions. Moreover, at the microscale, most of materials are heterogeneous, such as polymer chains in an amorphous polymer; therefore the continuous and homogeneous assumption for the classical modelling methods such as FE analysis is not applicable to analyze microscale behavior of a material. Typical examples at the microscale are ab initio methods (quantum mechanics) including many-body electronic structure theory, density functional theory (DFT), and quantum chemistry. These approaches can elucidate the nature of the bonds and elementary excitations from which all material properties derive as shown in Figure 2.1. Atomistic dynamics and statistics are widely used above the scale of electrons, which are referred to as molecular dynamics (MD) or kinetic Monte Carlo (MC) methods. MD simulations are particularly suited to understand kinetically dominated mechanisms in the field of nanomechanics that studies the fundamental atomic mechanisms involved in the initiation and evolution of damage. However, the length size and time scale that MD can simulate are very much limited, which are in order of nanometer and picosecond or nanosecond, respectively (E 2011; Solar et al. 2012).

2.3.2 MD Simulation

According to the above discussions of multi-scale modeling methods and the structural and chemical properties of asphalt with heterogeneities, MD simulation is selected for the study of the physics of asphaltic materials that is concerned with the prediction of the material properties from the interactions and motion of the fundamental components or atoms of the material. The prediction of material behavior at nanometer length scales promises the development of physics-based "bottom-up" analyses (Saether et al. 2009). Compared to classical continuum mechanics methods such as the FE method that provide an economical numerical representation of material behavior at length scale in which continuum assumptions apply, MD simulation does not need assume all constitutive relationships, kinematics, etc. a priori (Saether et al. 2009). This allows understanding the material physical properties, such as density, viscosity, thermodynamic properties, etc., in a more realistic way. Moreover, MD simulation has some advantages over an actual experiment at nano-scale, since it is difficult to study a material's nano-electro-mechanical system which is less than a micron in size in a laboratory. Specifically, the mechanical behavior of structures at nanoscale investigated using MD simulation makes it possible to attain extremely high fundamental frequencies while simultaneously preserving very small force constants (Wu et al. 2006). According to Wu et al.'s (2006) studies, although FE method used for some mechanics problems at nano-scale can give an indicative result, an atomistic scale simulation is necessary to get more accurate results.

2.4 Researches on Asphalt Using MD Simulation

2.4.1 Asphalt Models for MD Simulation

2.4.1.1 Preliminary Models

Zhang and Greenfield (2007a) developed preliminary asphalt models for MD simulations. They (2007a) chose *n-docosane* (*n*-$C_{22}H_{46}$) to represent stature, according to Storm and coworkers' (Storm et al. 1994) measurements for molecular structures of asphalt components using nuclear magnetic resonance (NMR). 1,7-Dimethylnaphthalene was chosen to represent aromatic. Moreover, two proposed asphaltene structures, asphaltene 1 and asphaltene 2 were chosen from Artok and Su's (Artok et al. 1999) study and Groenzin and Mullins's study (Groenzin and Mullins 2000), respectively. The molecular structures of all the fractions are shown in Figure 2.8. Two types of asphalt mixtures were created by using the two different asphaltene structures, respectively. Table 2.1 lists the overall composition of the mixtures (Zhang and Greenfield 2007a). It can be seen that for this preliminary study, resin fraction is not included.

Table 2.1 Overall Composition of Zhang and Green field's (2007a) Asphalt Models

Mixture Type	Number of Molecules			Mass Fraction (%)		
	n-C_{22}	1,7-dimethylnaphthalene	Asphaltene	*n*-C_{22}	1,7-dimethylnaphthalene	Asphaltene
1	41	27	5	59.6	19.7	20.7
2	45	30	5	59.1	19.8	21.1

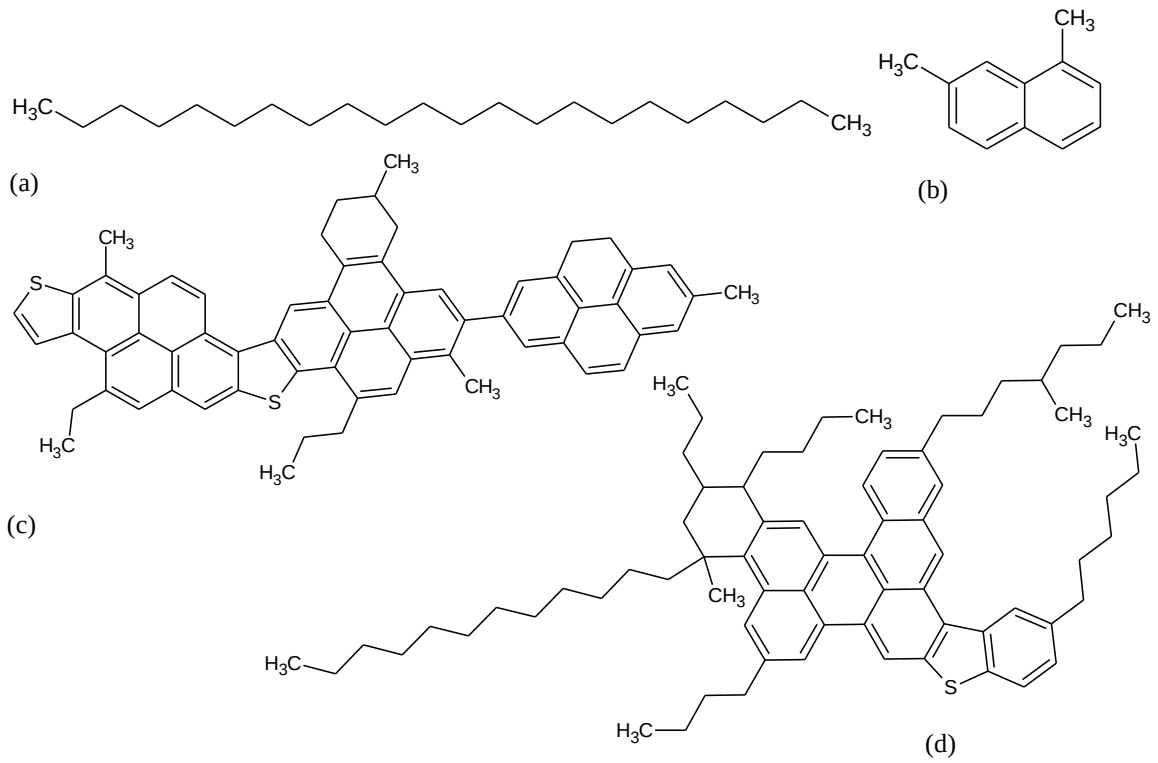

Figure 2.8 Preliminary asphalt component models of Zhang and Greenfield's (2007a) study: (a) *n-docosane* (*n*-$C_{22}H_{46}$), (b) 1,7-dimethylnaphthalene, (c) asphaltene 1, and (d) asphaltene 2

2.4.1.2 Improved Models

Subsequently, Li and Greenfield (2014) improved the model asphalt systems for MD simulation to represent the AAA-1, AAK-1, and AAM-1 asphalts of the Strategic Highway Research Program (SHRP), which are in good agreement with experimental data.

According to Li and Greenfield's (2014) study, the concentration of normal alkanes (n-paraffins) in saturate fractions is very low and the majority of alkanes are highly branched and cyclic alkanes. Thus, squalane and hopane are selected and the structures of

these two molecules are consistent with Netzel and Rovani's (Netzel and Rovani 2007) research on the saturate structures in neat SHRP asphalts. The hypothetical structures of saturate fraction are shown in Figure 2.9. The molecules are chosen to represent saturates are squalane and hopane (Li and Greenfield 2014).

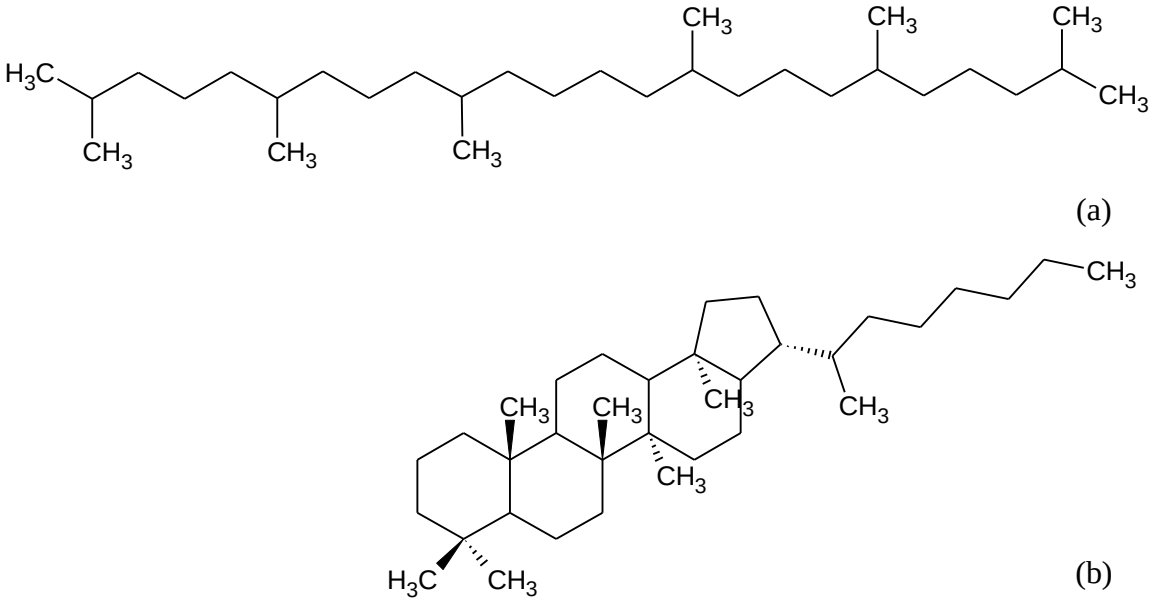

Figure 2.9 Structures of saturates: (a) squalane and (b) hopane (Li and Greenfield 2014)

Figure 2.10(a) and (b) shows the two hypothetical structures of aromatic fraction, with molecules named as dioctyl-cyclohexane-naphthalene (DOCHN) and perhydrophenanthrene-naphthalene (PHPN), respectively (Li and Greenfield 2014). The DOCHN structure was shown by Simanzhenkov and Idem (2003) as an average naphthene aromatic structure and the PHPN structure was proposed by Lira-Galeana and Hammami (2000).

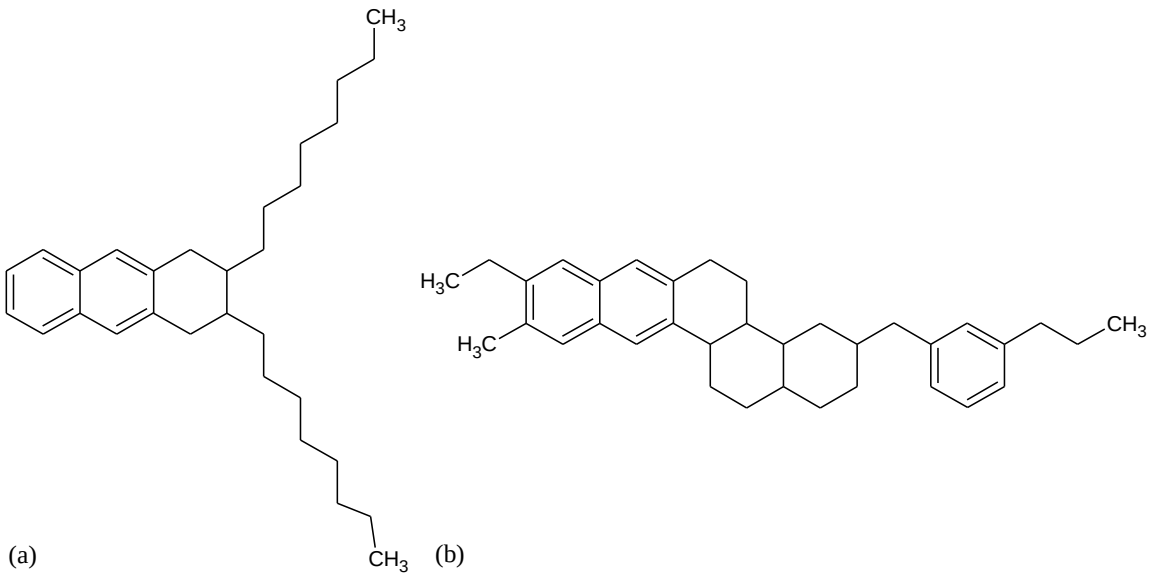

Figure 2.10 Structures of aromatics: (a) DOCHN and (b) PHPN (Li and Greenfield 2014)

Figure 2.11(a) to (e) are the hypothetical structures of resin fraction, with molecules named as benzobisbenzothiophene, pyridinohopane, quinolinohopane, trimethylbenzene-oxane, and thio-isorenieratane, respectively (Li and Greenfield 2014). These structures of resins are proposed by Li and Greenfield (2014) primarily from geochemistry literatures based on the analyses of petroleum found in sedimentary rock deposits.

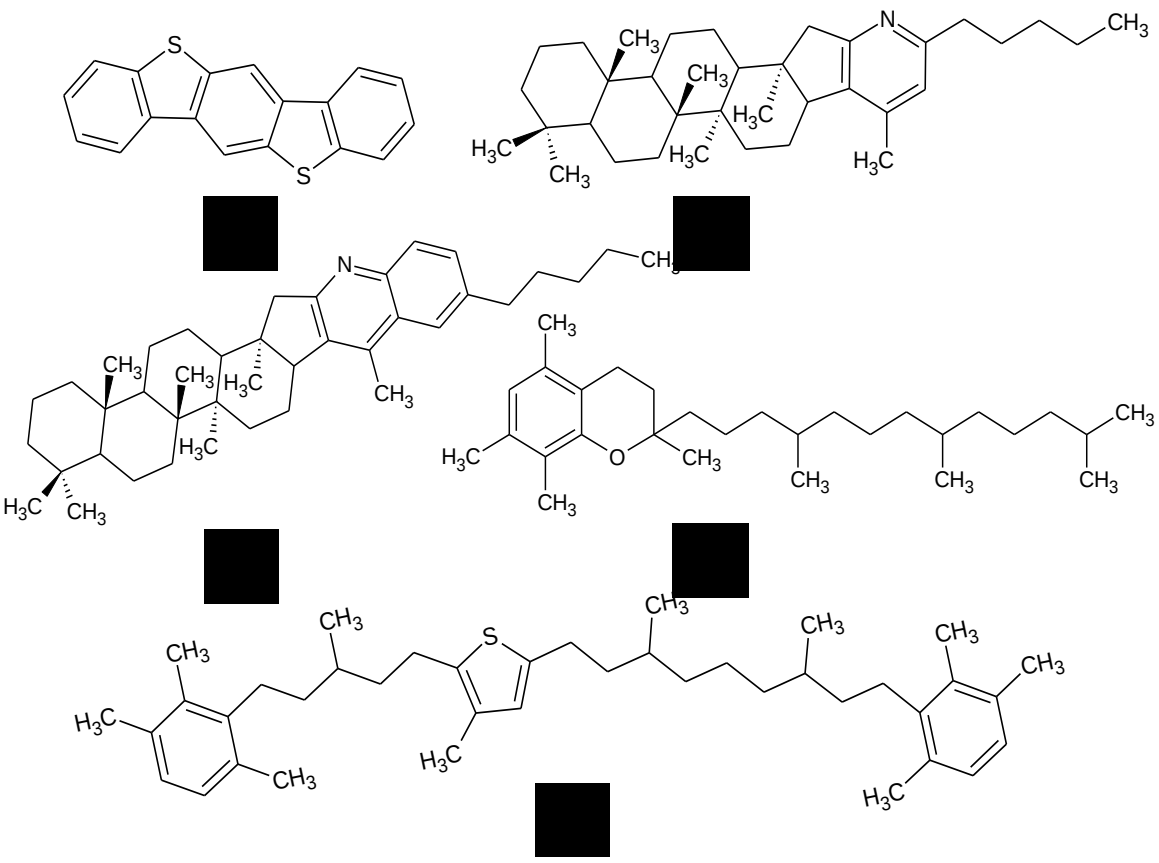

Figure 2.11 Structures of resins: (a) benzobisbenzothiophene, (b) pyridinohopane, (c) quinolinohopane, (d) trimethylbenzene-oxane, and (e) thio-isorenieratane (Li and Greenfield 2014)

The hypothetical structures of asphaltene fraction are illustrated from Figure 2.12(a) to (c), with molecules named as asphaltene-phenol, asphaltene-pyrrole, and asphaltene-thiophene, respectively (Li and Greenfield 2014). According to Li and Greenfield's (2014) study, the choices of asphaltene molecules were derived from Mullins's (2010) recent study which is more reflective of true asphaltene structures. However, the structures developed by Mullins have high internal energies due to "pentane effect" bonding conflicts; thus Li and Greenfield (2014) slightly modified the side group locations and Figure 2.12 show the final three structures of asphaltenes after Li and Greenfield's modifications.

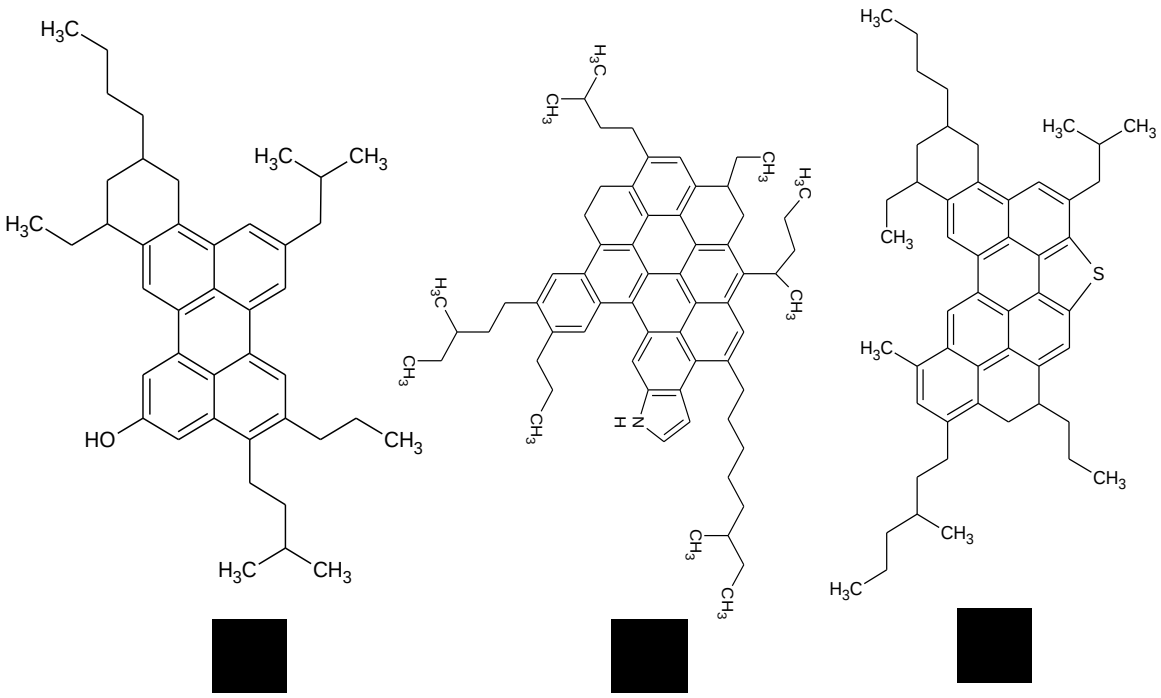

Figure 2.12 Structures of asphaltenes: (a) asphaltene-phenol, (b) asphaltene-pyrrole, and (c) asphaltene-thiophene (Li and Greenfield 2014)

2.4.2 Asphalt Property Studies Using MD Simulation: State of the Art

Zhang and Greenfield (2009; 2007a; b) used the two aforementioned preliminary models to conduct property calculations by MD simulations regarding density, viscosity, isothermal compressibility (inverse of bulk modulus), thermal expansion coefficient and heat capacity changes under different temperatures and found the results were consistent with experimental data. Results showed that density and viscosity decreased with an increase in temperature and the isothermal compressibility increased with an increase in temperature (Zhang and Greenfield 2007a). The MD simulation results also showed that the thermodynamic properties of the two asphalt models exhibited a high-frequency glass transition above 25 ℃. The model composed of more aromatic asphaltene showed a more pronounced transition and possessed a higher bulk modulus. Moreover, they added

a single polystyrene chain to one type of asphalt mixture to study the polymer modified asphalt. Noticeable changes in physical properties were found that the density increased and the thermal expansion coefficient shrank with an increase in temperature. The isothermal compressibility of polymer modified asphalt was lower than the unmodified asphalt, indicating stronger mechanical properties of asphalt by the presence of polymer modification (Zhang and Greenfield 2007a). Mart ń-Mart ńez et al. (2015) later modified the asphaltene structures in Li and Greenfield's asphalt model based on Clar sextet theory to better understand of the chemical structures of this class of materials.

Hansen et al. (2013) proposed a four-component united-atom model of asphalt, also called "Cooee-bitumen" model, including saturated hydrocarbon, resinous oil, resin and asphaltene, and characterized the asphalt model using graphic-processor-units based software in time spans order of microseconds regarding dynamical properties, relaxation time, stability of linear asphaltene nanoaggregates, and the rheology and molecular structure of the Cooee asphalt model under shear in the non-Newtonian regime using non-equilibrium MD simulations (Lemarchand et al. 2014, 2015). The chemical aging of Cooee asphalt was also investigated by Lemarchand et al. (2013). The aging reaction was modelled by the chemical reaction: "2 resins $\rightarrow$ 1 asphaltene" and the rheological and dynamical properties of the each composition were studied.

Tarefder and Arisa (Tarefder and Arisa 2011) studied density and energy changes of asphaltene and resin in asphalt with and without oxygen presence under different temperatures using MD simulations. Groenzin and Mullins's (2000) asphaltene model was selected and Murgich et al.'s (Murgich et al. 1996) two resin models were chosen.

Results showed that density had an inverse relationship with the temperature for both asphaltene and resin systems and higher temperature caused higher thermal energies of both asphaltene and resin molecules. The percentage of oxygen affected the glass transition temperature of asphaltene. At low oxygen content (less than 20%), asphaltene showed a constant glass transition temperature, while at high oxygen content (more than 20%), the vaulue of the glass transition temperature of asphaltene decreased. It was found that there was no definite relationship between the oxygen content and glass transition temperature.

Pan et al. (2012a; b) explored the possible chemical reactions between asphalt components and oxygen in an *ab initio* quantum chemistry (QC) based environment and used X-ray photoelectron spectroscopy (XPS) to validate their QC-based models. They concluded that ketones formed at benzylic carbon atoms and sulfoxides formed at sulfur atoms are the major oxidation products and saturates show the least change under oxidation.

However, none of the previous studies analyzed and compared the physical, thermodynamic, rheological and mechanical changes of asphalt before and after oxidative aging using MD simulations, which is done here.

CHAPTER 3

METHODOLOGY

3.1 Modeling of Asphalt Molecules

3.1.1 Asphalt Components Before Oxidative Aging

The improved model asphalt systems developed by Li and Greenfield (2014) was used in this study as previously discussed. Culgi 8.0.1 software was used to generate all the molecules. Details of the four fractions, saturates, aromatics, resins and asphaltenes, in the asphalt systems are presented in Figure 3.1 to Figure 3.4, respectively. In the figures, the black sphere is carbon; the white sphere is hydrogen; the red sphere is oxygen; the yellow sphere is sulfur; and the blue sphere is nitrogen.

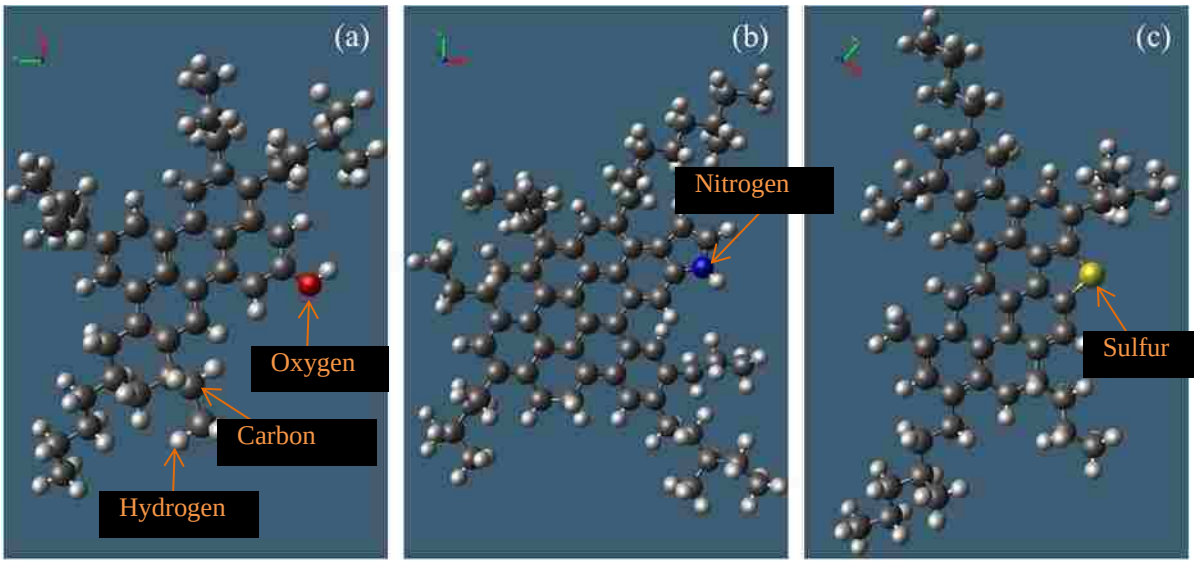

Figure 3.1 Molecular structures of asphaltene fraction: (a) asphaltene-phenol, $C_{42}H_{54}O$, (b) asphaltene-pyrrole, $C_{66}H_{81}N$, and (c) asphaltene-thiophene, $C_{51}H_{62}S$ (Li and Greenfield 2014)

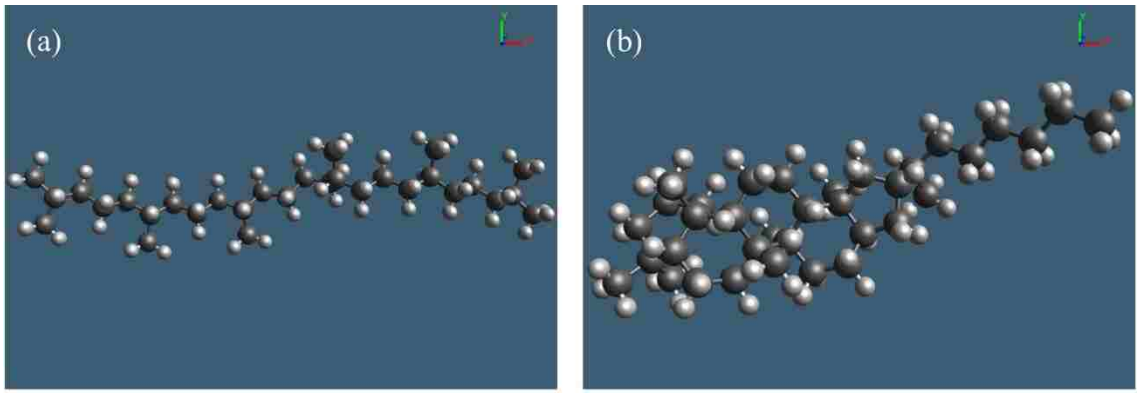

Figure 3.2 Molecular structures of saturate fraction: (a) Squalane, $C_{30}H_{62}$. (b) Hopane, $C_{35}H_{62}$ (Li and Greenfield 2014)

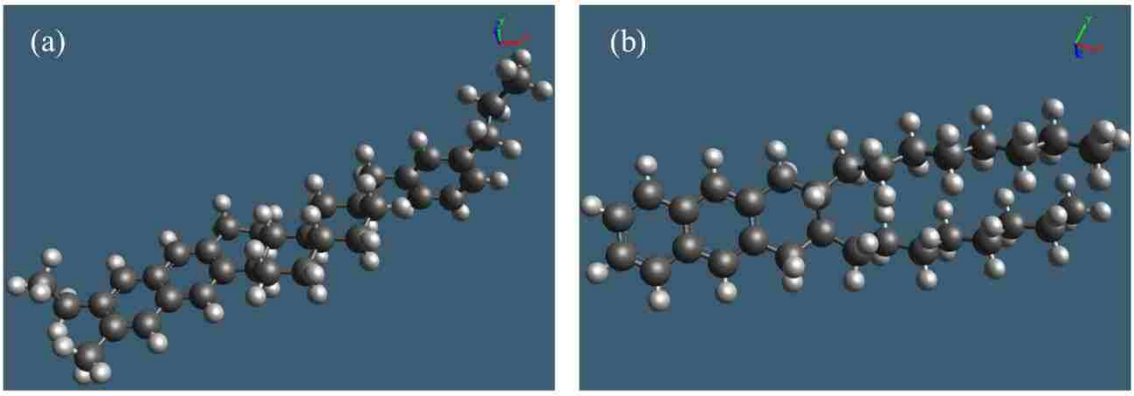

Figure 3.3 Molecular structures of aromatic fraction: (a) PHPN, $C_{35}H_{44}$ and (b) DOCHN, $C_{30}H_{46}$ (Li and Greenfield 2014)

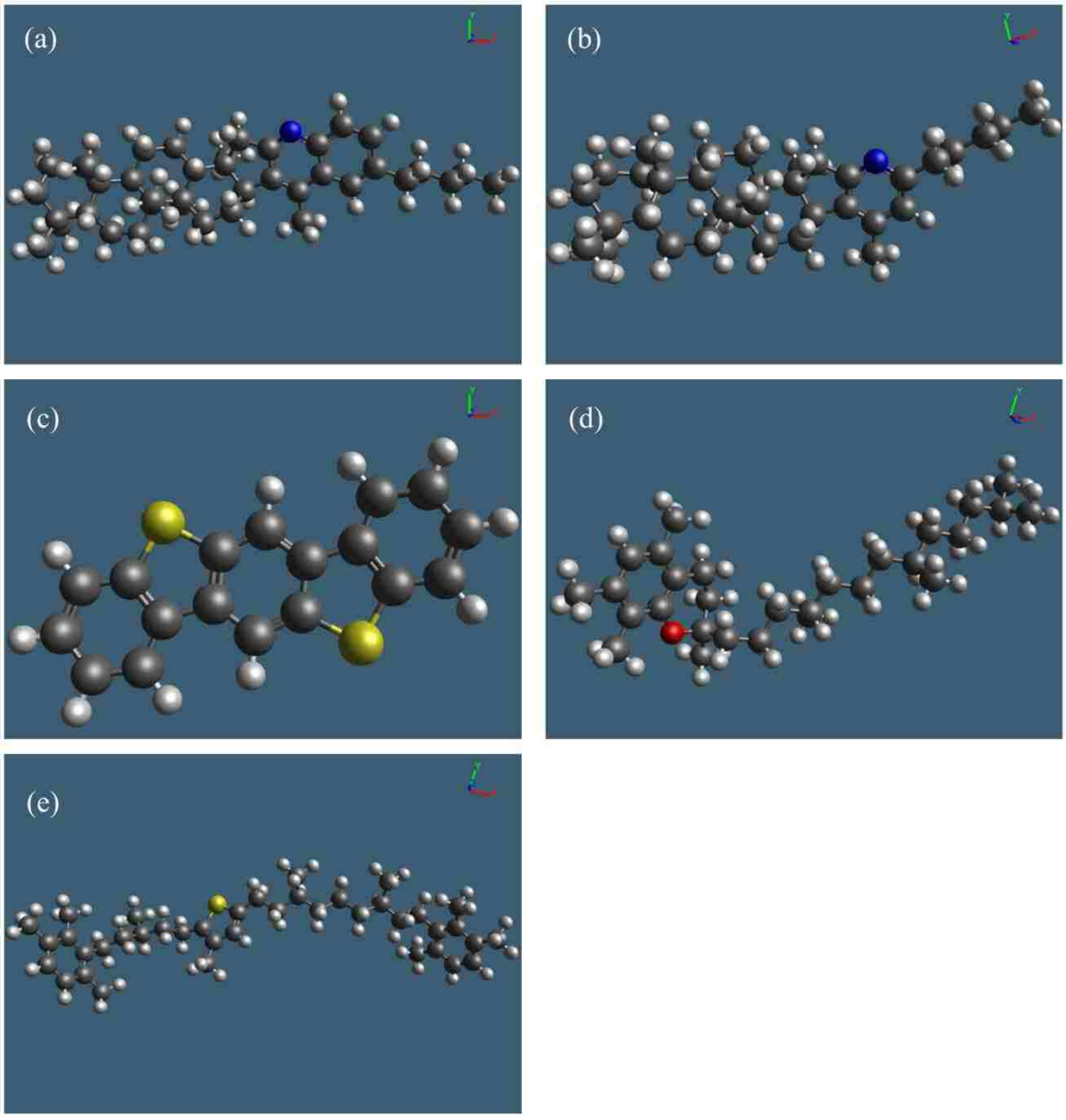

Figure 3.4 Molecular structures of resin fraction: (a) quinolinohopane, $C_{40}H_{59}N$, (b) pyridinohopane, $C_{36}H_{57}N$, (c) benzobisbenzothiophene, $C_{18}H_{10}S_2$, (d) trimethylbenzene-oxane, $C_{29}H_{50}O$, and (e) thio-isorenieratane, $C_{40}H_{60}S$ (Li and Greenfield 2014)

3.1.2 Asphalt Components After Oxidative Aging

The oxidation products in each asphalt component are determined by its existing sensitive chemical functional groups as previously mentioned. There are two major products formed in asphalt after oxidative aging: One is ketone formed at benzylic carbon position

which is the carbon atom adjacent to an aromatic ring system, and another one is sulfoxide formed at sulfide (Pan et al. 2012a; b; Petersen 2009). The reactions between the two most sensitive functional groups and oxygen are illustrated in Figure 3.5(a) and (b), respectively.

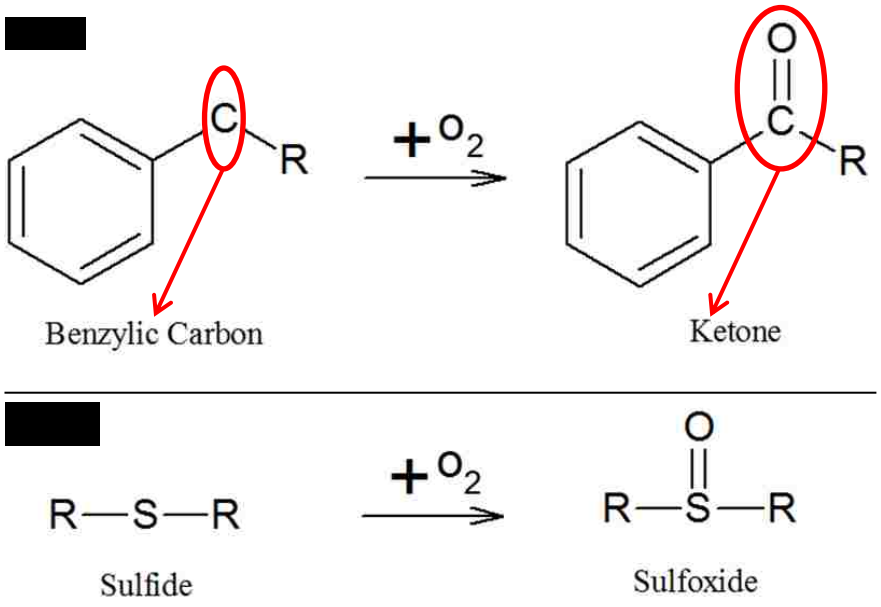

Figure 3.5 Major oxidation reactions and products in asphalt: (a) formation of ketone and (b) formation of sulfoxide

The molecular structures of aromatics, resins and asphaltenes after oxidative aging have been developed based on the previous unoxidized models, according to the sensitive functional groups existing in the asphalt and their major oxidation products as stated above, as shown in Figure 3.6 to Figure 3.8. It can be seen that the oxidation products are ketones and sulfoxides and the number of each oxidized functional groups is depending on the numbers of benzylic carbon atoms and sulfur atoms existing in each asphalt molecule. The saturates have no changes after oxidation due to lack of sensitive functional groups.

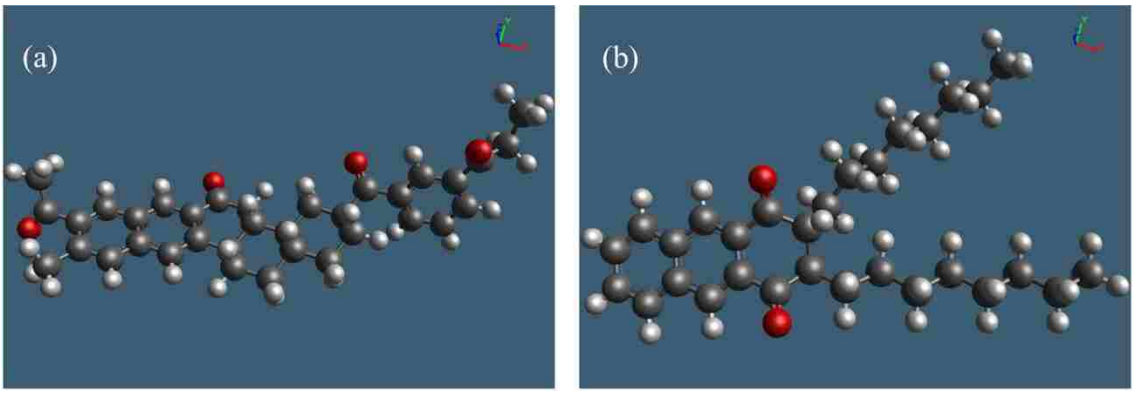

Figure 3.6 Aromatic fraction after oxidative aging: (a) oxidized PHPN, $C_{35}H_{36}O_4$ and (b) oxidized DOCHN, $C_{30}H_{42}O_2$

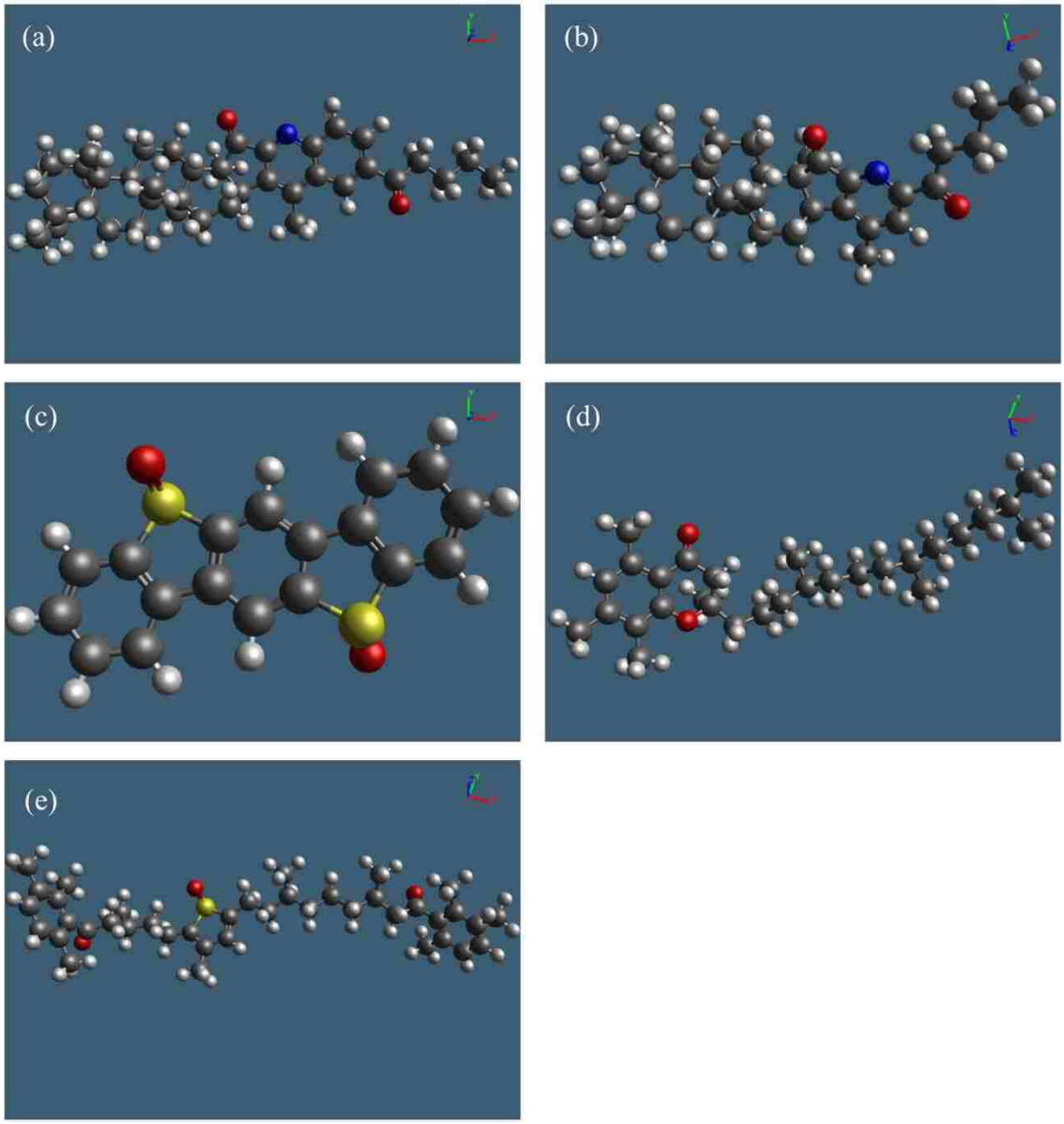

Figure 3.7 Resin fraction after oxidative aging: (a) oxidized quinolinohopane, $C_{40}H_{55}NO_2$, (b) oxidized pyridinohopane, $C_{36}H_{53}NO_2$, (c) oxidized benzobisbenzothiophene, $C_{18}H_{10}S_2O_2$, (d) oxidized trimethylbenzene-oxane, $C_{29}H_{48}O_2$, and (e) oxidized thio-isorenieratane, $C_{40}H_{56}SO_3$

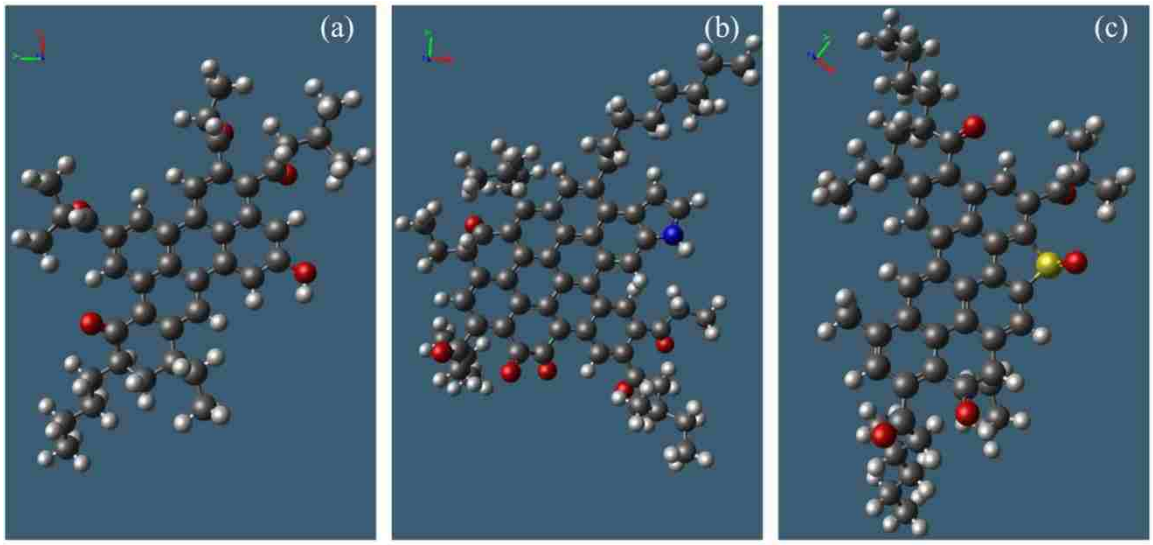

Figure 3.8 Asphaltene fraction after oxidative aging: (a) oxidized asphaltene-phenol, $C_{42}H_{46}O_5$, (b) oxidized asphaltene-pyrrole, $C_{66}H_{67}NO_7$, and (c) oxidized asphaltene-thiophene, $C_{51}H_{54}SO_5$

3.2 MD Simulation

3.2.1 Theory of MD Simulation

MD simulation computes, using a computer, the motion of a series of atoms, their co-ordinates in three-dimensional space, and their connectivity in a system as a function of time. It solves the classical equations of motion of *N* atoms interacting via a potential *U*, the sum of the pair potential of all the atoms. In Cartesian coordinates the equation of motion is simply the Newton's law of motion:

$$a_i(t) = \frac{dv_i(t)}{dt} = \frac{d^2 r_i(t)}{dt^2} = \frac{F_i}{m_i} \tag{3.1}$$

where, r_i is the position of an atom i, m_i is the mass of the atom, a_i is the resulting acceleration of the atom, v_i is the resulting velocity of the atom, and t is time. The force F_i acting on the atom is defined as the negative gradient of the potential U:

$$F_i = -\frac{dU_i(r)}{dr_i} \tag{3.2}$$

$$U_i(r) = U_{i_{bonded}}(r_i) + \sum_{j=1}^{N-1} U_{ij}(r_{ij}) \tag{3.3}$$

where, U is the combination of intramolecular and intermolecular potentials which describes the energies associated with both bonded interactions within the molecule and non-bonded molecules/atoms being in a particular conformation relative to each other, and r_{ij} is the distance between the interacting sites for the pair of atoms i and j.

In general, the above equations of motion are solved using Verlet integration algorithm. The most widely used for integrating molecular dynamics equations is the velocity Verlet algorithm, which gives positions, velocities and accelerations at the same time and does not compromise precision (Leach 2001). This method is used in this study. The position and velocity of atom i at the next step in time is determined by the following equations:

$$r_i(t+dt) = r_i(t) + v_i(t)dt + \frac{1}{2}a_i(t)dt^2$$

(3.4)

$$v_i(t+dt) = v_i(t) + \frac{1}{2}[a_i(t) + a_i(t+dt)]dt \tag{3.5}$$

where, dt is the time step.

The atoms in the simulation are treated as semi-hard spheres connected by springs, which represent covalent bonds. The potential U is quantified by the sum of energy terms calculated by empirical functions called valence force fields. These force fields describe the deviation of bond lengths, bond angles and torsion angles away from equilibrium values, and terms for non-bonded pairs of atoms including van der Waals, electrostatic, and other interactions. Nowadays, many different force fields are available for use depending on the research purposes. For organic molecules such as asphaltic materials, the most popular force fields used include DREIDING, OPLS-AA, and COMPASS, which use different force constants and geometry parameters (Fried 2007).

Moreover, a MD simulation needs to be performed under a specific ensemble for different purposes. The ensembles include microcanonical ensemble [NVE, with constant number of particles (N), system volume (V), and total energy (E)], canonical ensemble [NVT, with constant number of particles (N), system volume (V), and temperature (T)], isothermal-isobaric ensemble [NPT, with constant number of particles (N), system pressure (P), and temperature (T)], and anisotropic isothermal-isobaric ensemble ($NP_xP_yP_zT$, with stress applied on either x, y, or z direction). The MD simulation procedures are illustrated in Figure 3.9.

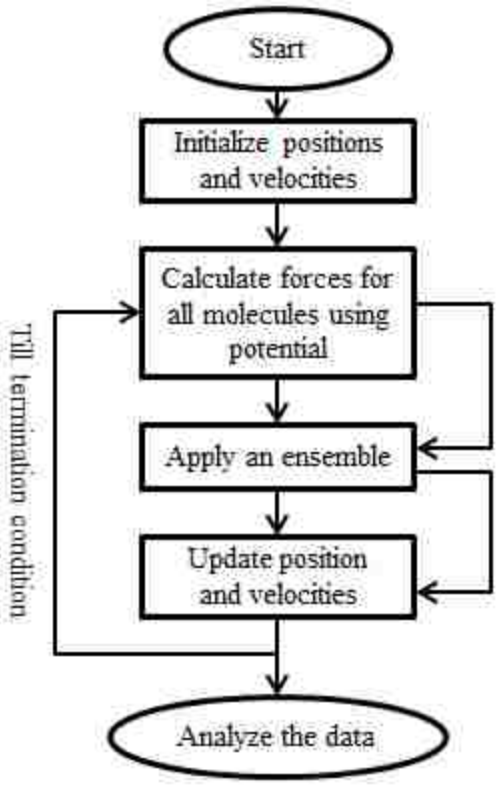

Figure 3.9 MD simulation flow chart

For this study, the MD simulation was conducted by Culgi 8.0.1 software and an all-atom model was used to explicitly represent each atom in a molecule. DREIDING force field was used to approximate the interactions among asphaltic molecules, which was first customizedly parameterized from semi-empirical data through calculations of model compounds of asphalt.

3.2.2 DREIDING Force Field

DREIDING is a simple but versatile and generic all-atom force field, which is developed to predict structures and dynamics of organic, biological, and main-group inorganic molecules (Fraaije et al. 2014; Fried 2007). It defined the potential energy, E_p for an arbitrary geometry of a molecule in MD simulation. The DREIDING force field is

expressed as a superposition of valence (or bonded) interactions, E_{val} that depend on the specific connections (bonds) of the structure and non-bonded interactions, E_{nb} that depend only on the distance between the atoms (Fraaije et al. 2014; Mayo et al. 1990):

$$E_p = E_{val} + E_{nb} \tag{3.6}$$

3.2.2.1 Bonded Interactions

The valence interactions include bond stretch (E_B), bond-angle bend (E_A), dihedral angle torsion (E_T), and inversion terms (E_I):

$$E_{val} = E_B + E_A + E_T + E_I \tag{3.7}$$

For bond stretch and bond-angle bend interactions, DREIDING uses a harmonic distance form and a harmonic angle form, respectively:

$$E_B = \frac{1}{2}\sum_{bonds} k_{ij}^{bond}(r_{ij} - r_{ij}^0)^2 \tag{3.8}$$

where, k_{ij}^{bond} is the bond stretch force constant, r_{ij} is the bond distance between atom *i* and atom *j*;

$$E_A = \frac{1}{2}\sum_{bends} k_{ijk}^{bend}(\theta_{ijk} - \theta_{ijk}^0)^2 \tag{3.9}$$

where, k_{ijk}^{bend} is the bond-angle bend force constant, for two bonds *ij* and *jk* sharing a common atom, θ_{ijk} is the angle between bonds *ij* and *jk*, θ_{ijk}^0 is the equilibrium angle.

The dihedral angle torsion is defined as:

$$E_T = \frac{1}{2} \sum_{dihedrals} V_{jk}^{tor} \left\{1 - \cos(n_{jk}(\varphi_{jk} - \varphi_{jk}^0)^2\right\} \tag{3.10}$$

where, V_{jk}^{tor} is the barrier to rotation, φ_{jk} is the dihedral or torsional angle between the *ijk* and *jkl* planes formed by two bonds *ij* and *kl* connected via a common bond *jk*, φ_{jk}^0 is the equilibrium angle.

The inversion potential is important for atoms that are bonded to three other atoms, which represents the favorability of keeping all the three bonds for atom *i* bonded to exactly three other atoms *j*, *k*, and *l*, in the same plane. The inversion potential for normal planar configurations is expressed in cosine form:

$$E_I = \sum_{inversion} K_I^{inv}(1 - \cos\Psi_I) \tag{3.11}$$

where, K_I^{inv} is the inversion force constant, Ψ_I is the angle between *il* bond and *jik* plane.

3.2.2.2 Non-bonded Interactions

The non-bonded interactions are composed of van der Waals or dispersion (E_{vdW}), electrostatic (E_Q), and explicit hydrogen bonds (E_{hb}) terms:

$$E_{nb} = E_{vdW} + E_Q + E_{hb} \tag{3.12}$$

Van der Waals interaction can be classified into intramolecular van der Waals energy and intermolecular van der Waals energy, which is the sum of the attractive or repulsive interactions between parts of the same molecule and the sum of the attractive or repulsive interactions between molecules, respectively. The equation for van der Waals energy is:

$$E_{vdW} = \sum_{vdW} \epsilon_{ij} \left[\left(\frac{\sigma_{ij}}{r_{ij}} \right)^{12} - 2 \left(\frac{\sigma_{ij}}{\sigma_{ij}} \right)^{6} \right] \tag{3.13}$$

where, r_{ij}, ϵ_{ij}, and σ_{ij} denote the distance between the interacting sites, the Lennard-Jones well depth, and the size parameter, respectively, for the pair of atom *i* and *j*.

Electrostatic interactions can be described as the electric interaction between two charged objects, and also can be classified into intra and inter molecular electrostatic energy. Electrostatic energies are calculated using the Coulomb interaction potential:

$$E_Q = \sum_{electro} \frac{1}{4\pi\epsilon_0} \frac{q_i q_j}{r_{ij}} \tag{3.14}$$

where, q_i and q_j are the point charges, and ϵ_0 is the electrical permittivity of the vacuum.

A hydrogen bond is the electromagnetic attractive interaction between polar molecules in which hydrogen (H) is bound to a highly electronegative atom. Under DREIDING force field, the explicit hydrogen bonding energy has a function as follows:

$$E_{hb} = D_{hb}\left[5\left(\frac{R_{hb}}{R_{D-A}}\right)^{12} - 6\left(\frac{R_{hb}}{R_{D-A}}\right)^{10}\right]\cos^4\theta \tag{3.15}$$

where, θ is the angle donor-hydrogen-acceptor, and R_{D-A} is the distance between donor and acceptor in Å. For the constant parameters, R_{hb} is 2.75 Å and D_{hb} has a different 'strength' depending on the type of partial atomic charges used in Culgi software (Fraaije et al. 2014).

3.2.3 Constant Temperature and Pressure Controls

The most common used temperature and pressure controls in MD simulations are Berendsen and Andersen thermostats and barostats (Fraaije et al. 2014). They were also used in this study.

3.2.3.1 Berendsen Thermostat and Barostat

To maintain a constant temperature in a simulation system, Berendsen et al. (1984) proposed a method via a weak coupling of the system to a heat bath with fixed reference temperature. The equation of motion in this technique is modified to:

$$m_i\mathbf{a}_i = -\frac{\partial U\left(\mathbf{r}^N\right)}{\partial \mathbf{r}_i} + \frac{m_i}{\tau_T}\left(\frac{T_0}{T} - 1\right)\frac{\partial \mathbf{r}_i}{\partial t} \tag{3.16}$$

where, τ_T is a damping constant that governs the strength of the coupling to the external bath, and T_0 is the reference (target) temperature. Here, τ_T is referred to as the thermal coupling parameter.

To setup a constant pressure system, Berendsen et al (1984) used the same principle as used to maintain a constant temperature system. They introduced a weak coupling of the system to a constant pressure bath via adding an extra term to the equation of motion:

$$\frac{\partial \mathbf{r}_i}{\partial t} = \frac{\mathbf{P}_i}{m_i} - \frac{\beta_T \left(P - P_0\right)}{3\tau_P} \tag{3.17}$$

where, β_T is the isothermal compressibility and τ_P is the pressure coupling parameter.

3.2.3.2 Andersen Thermostat and Barostat

Andersen (1980) thermostat describes a physical system with weak stray interactions between the molecules in the system and the particles of a heat bath at a specified temperature. A stochastic method is implemented, where the collision to the imaginary heat bath is simulated via resetting the velocity of a randomly selected atom from the Maxwell-Boltzmann distribution at a certain predefined interval.

The time between collisions is chosen from a Poisson distribution with a certain average collision time. When the collision interval is large, energy fluctuations will occur slowly along with the kinetic energy fluctuations simulating that of a conventional MD. If the collision interval is too small, the kinetic energy fluctuations could be too high and that in turn could slow down the speed at which the molecules in the system explore the configuration space. The recommended collision frequency from Andersen's (1980) study is provided by:

$$rate\ per\ particle \propto \frac{\gamma_T}{\rho^{1/3} N^{2/3}} \tag{3.18}$$

where, γ_T is the thermal conductivity of the system.

The pressure control developed by Andersen (1980) is based on an extended system method, in which, the system is coupled to an external variable, the volume of the system. This process simulates the action of a piston on a real system, which is a three-dimensional virtual piston. The kinetic energy related to the external variable is defined by:

$$\kappa_V = \frac{1}{2} M \left(\frac{\partial V}{\partial t} \right)^2 \tag{3.19}$$

where, V is the volume of the system and M is the mass of the piston.

The potential energy related to the external variable is:

$$U_V = PV \tag{3.20}$$

The equations of motion for the extended system are as follows:

$$\frac{\partial \mathbf{r}_i}{\partial t} = \frac{\mathbf{P}_i}{m_i} + \frac{1}{3} \mathbf{r}_i \frac{\partial \ln V}{\partial t} \tag{3.21}$$

$$\frac{\partial^2 \mathbf{r}_i}{\partial t^2} = -\frac{1}{m_i} \frac{\partial U\left(\mathbf{r}^N\right)}{\partial \mathbf{r}_i} + \frac{1}{3} \mathbf{r}_i \left(\frac{1}{V} \frac{\partial^2 V}{\partial t^2} - \frac{2}{3} \left[\frac{1}{V} \frac{\partial V}{\partial t} \right]^2 \right) \tag{3.22}$$

$$\frac{\partial^2 V}{\partial t^2} = \frac{P - P_0}{M} \tag{3.23}$$

3.3 Preprocessing Before MD Simulation

3.3.1 Geometry Optimization and Charge Calculation

For each asphaltic molecular structure, the semi-empirical quantum chemistry program MOPAC 2012 was used for geometry optimizations and calculation of partial charges and missing torsion parameters. These semi-empirical quantum mechanics-based parameters were used in the DREIDING force field for later energy minimization and MD simulation. Compared to quantum mechanics modeling program, the semi-empirical method solve problems much faster avoiding computational intensive steps by using approximations and empirically determined parameters that are used to obtain the best fit of predicted results to a training set of reference data (Stewart 2013). The semi-empirical Hamiltonians PM7 method in MOPAC 2012 is used in the electronic part calculation to obtain molecular orbitals, the heat of formation, and its derivative regarding molecular geometry (*MOPAC 2012 Software Manual* 2012). The PM7 method is a new method developed by Stewart to provide a more accurate parameterization for all the main group elements using experimental and high-level ab initio reference data (*MOPAC 2012 Software Manual* 2012).

Since the structure of asphaltic molecules are complex and asymmetric and even contain heteroatoms such as oxygen, the partial charges are necessary to be calculated due to the asymmetric distribution of electrons in chemical bonds and orbitals, which cause intra and inter molecular electrostatic interactions. The default MOPAC method is used to calculate the partial charges by summing up the density matrix elements for each atom's basis functions (*MOPAC Guide* 2010).

Overall, the estimated parameters from MOPAC calculation enabled the model asphalt systems more close to real asphaltic materials.

3.3.2 Asphalt Systems Modelling

According to Li and Greenfield's (2014) study, the SHRP AAA-1 model asphalt system was the closest to real asphalt among all model asphalt systems that they proposed. Therefore, the AAA-1 model asphalt system was chosen for this study. The number of each type of molecule and the solubility fractions to use in the model asphalt before and after oxidative aging is shown in Table 3.1 (Li and Greenfield 2014). The mass percentage of each fraction was normalized to match the experimental totals, which were obtained from literature experimental values by Jones' (1993) study. It can be seen that the mass percentage distributions of solubility fractions of the model system before oxidation match well with experimental values, while after oxidation, the mass percentage of the saturate fraction decreases in the oxidized asphalt system, along with an increase in the mass percentage of resin and asphaltene fractions. This indicates more polar fractions are formed in the asphalt after oxidation.

Table 3.1 Model Asphalt System Compositions Before and After Oxidative Aging

Asphalt Fraction	Molecule	Number in AAA-1 model system	Percentage of each fraction before oxidation[a]	Percentage of each fraction after oxidation[a]	Experimental data before oxidation[b]
Saturates	Squalane Hopane	4 4	10.7	9.9	10.6
Aromatics	PHPN DOCHN	11 13	38.1	38.0	37.3
Resins	Quinolinohopane Thio-isorenieratane Benzobisbenzothiophene	4 4 5	30.6	31.1	31.8

	Pyridinohopane	4			
	Trimethylbenzene-oxane	15			
	Asphaltene-phenol	3			
	Asphaltene-pyrrole	2			
Asphaltene	Asphaltene-thiophene	3	16.5	16.9	16.2

[a] Percentage of each fraction is normalized to match the experimental totals (Li and Greenfield 2014a).
[b] Literature experimental values are from Jones (1993).

All the molecules of unoxidized and oxidized asphalts were put into their individual simulation box to represent unoxidized asphalt system and oxidized asphalt system, respectively, with the same initial size of 100×100×100 $Å^3$. The size of simulation box was large enough for containing all the asphalt fractions. Amorphous asphalt systems were then built representing realistic initial conformations of asphaltic molecules. Condensed phases of both unoxidized and oxidized asphalt systems were obtained first along with energy minimization to remove all non-bonded overlapping between different particles and spread rings by a Monte Carlo minimization algorithm. The model asphalt systems before and after oxidative aging are shown in Figure 3.10.

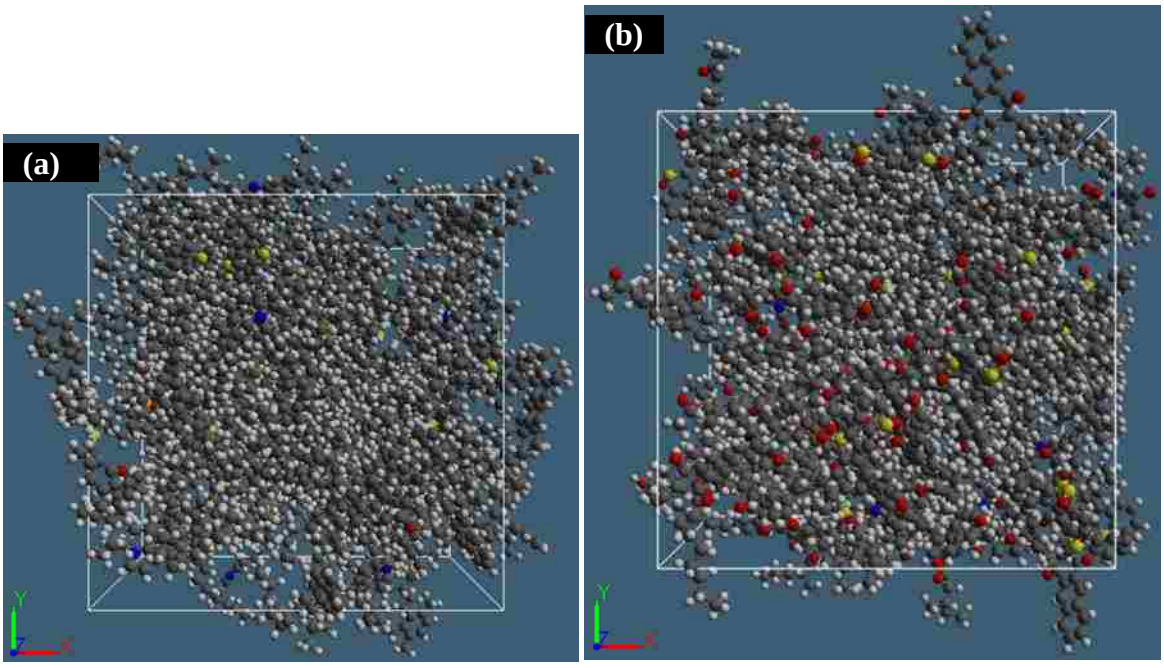

Figure 3.10 Simulation boxes of asphalt systems before and after oxidative aging with (a) unoxidized model asphalt system and (b) oxidized model asphalt system

3.3.3 Energy Minimization

Energies of atomistic structure generated from amorphous systems can be very high due to a high degree of intermolecular overlaps, which cannot be used directly as the starting configuration for later MD simulation. Therefore, molecular energy minimization simulations were conducted for the model asphalt systems before and after oxidative aging to remove any non-bonded overlap between different particles and speared rings with rings overlap or that molecular tails cross through the hole of the ring. This procedure was realized by a novel force-based Monte Carlo minimization algorithm, Quick-Min (QM) (Fraaije et al. 2014). The QM method follows the force vector from an initial configuration to a nil in the force by accelerating the system in the direction of the force. A projection of the velocity along the force serves as the damping parameter to rest the system in a local minimum. Euler integrator is used to couple with the QM method in Culgi for energy minimization, as described follows (Fraaije et al. 2014; Sheppard et al. 2008):

Step 1: Given the velocity $\boldsymbol{V}_j$ and force $\hat{\boldsymbol{F}}_j$ at iteration j, where $\boldsymbol{V}_j$ is the $3N$-dimensional cumulative velocity vector for N particles and $\hat{\boldsymbol{F}}_j$ is the $3N$-dimensional unit force vector for N particles; let

$$P = \boldsymbol{V}_j \cdot \hat{\boldsymbol{F}}_j \tag{3.24}$$

Step 2: If $P > 0$, project the velocity in the direction of the force, let

$$\boldsymbol{V}_j = (\boldsymbol{V}_j \cdot \hat{\boldsymbol{F}}_j)\hat{\boldsymbol{F}}_j \tag{3.25}$$

Step 3: If P <0, meaning the velocity is antiparallel to the force, set

$$\boldsymbol{V}_j = 0 \tag{3.26}$$

Step 4: Take an Euler step,

$$\boldsymbol{R}_{j+1} = \boldsymbol{R}_j + \Delta t \boldsymbol{V}_j \tag{3.27}$$

$$\boldsymbol{V}_{j+1} = \boldsymbol{V}_j + \Delta t \boldsymbol{F}_j \tag{3.28}$$

where, $\boldsymbol{R}_j$ is the configuration at iteration j, Δt is the time step between two iterations, and $\boldsymbol{F}_j$ is the force at iteration j.

Step 5: Check for convergence as defined by the software: if converged, stop; if not converged: repeat.

In this study, the maximum allowed step size for each particle translation is 0.2 Å in any single step to prevent wild steps in high force regions (Fraaije et al. 2014).

3.3.4 Periodic Boundary Condition

To create the bulk state (gas, liquid or solid) of asphalt systems before and after oxidative aging, periodic boundary conditions were implemented in this study. The mechanism of periodic boundary condition model is shown in Figure 3.11. In a periodic boundary condition model, molecules are initially placed within a simulation box, as A and B in Figure 3.11. The molecules not only interact with their neighbors in the same simulation box, but they also interact with images of molecules in neighboring simulation boxes, as

A1-A9 and B1-B9 in Figure 3.11. Thus, during the simulation, a molecule can diffuse to the edge of the simulation box and freely cross over into the next box. When this happens, an image molecule enters into the simulation box from other side to maintain the density of the system constant and eliminate edge effects (Fraaije et al. 2014).

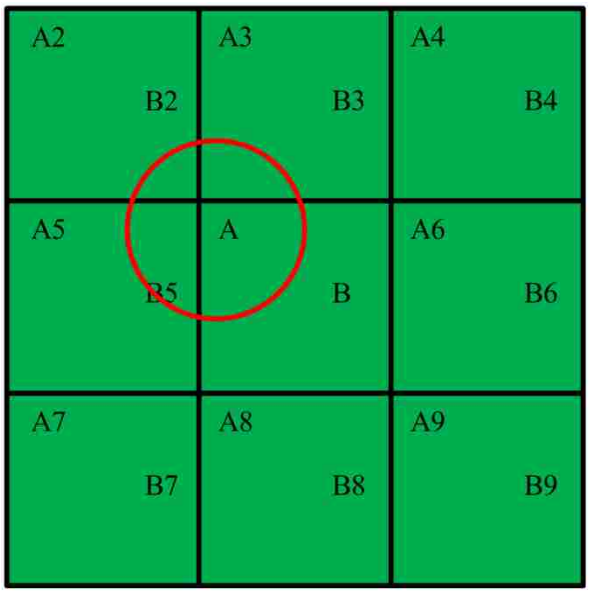

Figure 3.11 Periodic boundary condition model, showing the minimum image convention

One potential issue is that a molecule could meet multiple copies of itself and of other molecules in other boxes. To solve this problem, the *minimum image convention* is used by defining a cutoff radius, which is the distance that atoms only interact with other atoms within this cutoff value and is represented by the red circle in Figure 3.11. The cutoff distance is usually less than half of the box size to guarantee that an atom cannot meet two copies of another atom (Fraaije et al. 2014). The initial condensed simulation box sizes for both unoxidized and oxidized asphalts were approximately $36 \times 36 \times 36$ Å^3, so

the cutoff radius was set less than 17 $Å^3$. The suitable cutoff radius selection is discussed in Section 3.4 below.

3.4 Equilibrium Systems for MD Simulation

3.4.1 Parameters Setting

The effects of different parameters on the simulation results were investigated regarding cutoff radius and simulation time step. For all the MD simulations, system pressure was set at 101.325 kPa (1.0 atm) and system temperature was set at 25 ℃. The smooth particle mesh Ewald (SPME) method was used for handling long-range electrostatic and van der Waals interactions.

For the investigation of different cutoff radiuses effects on simulation results, the simulation time step was set the same for all the simulations. Two cutoff radiuses were considered as 7.5 Å and 17 Å. The MD simulation systems of both unoxidized and oxidized asphalts were first relaxed using a canonical ensemble, known as NVT ensemble. The simulation time step was set at 0.1 fs and with simulation duration of 20 ps (200,000 running steps). An isothermal-isobaric ensemble, also called NPT ensemble, was then used to simulate the realistic asphalt systems and to obtain the densities of asphalt systems. The simulation time step under the NPT ensemble was set at 0.5 fs with simulation duration of 500 ps (1,000,000 running steps) to guarantee the system could reach equilibrium.

The effects of different time steps on simulation results were also examined. The cutoff radius was set at 7.5 Å for all the simulations. The MD simulation systems of both

unoxidized and oxidized asphalts were first relaxed in a NVT ensemble at 0.1 fs time step and then simulated under a NPT ensemble at 0.5 fs to research equilibrium. For comparison, the initial systems were then simulated at 0.2 fs time step in a NVT ensemble and sequentially the systems were simulated at 0.3 fs time step in a NPT ensemble. The simulation duration under different ensembles were set as the same as stated previously.

3.4.2 Simulation Results

Figure 3.12 shows one example of simulation results of the asphalt density change before and after oxidative aging at 25 ℃ with 7.5 Å cutoff radius, 0.1 fs time step for NVT ensemble and 0.5 fs time step for NPT ensemble. It can be seen that simulations researched equilibrium after 400,000 simulation steps and it was the same for all other density simulations at 25 ℃ under different cutoff radiuses and time steps. The density values after 400,000 simulation steps under different cutoff radiuses and time steps were used for statistical analyses to determine the suitable cutoff radius and time step.

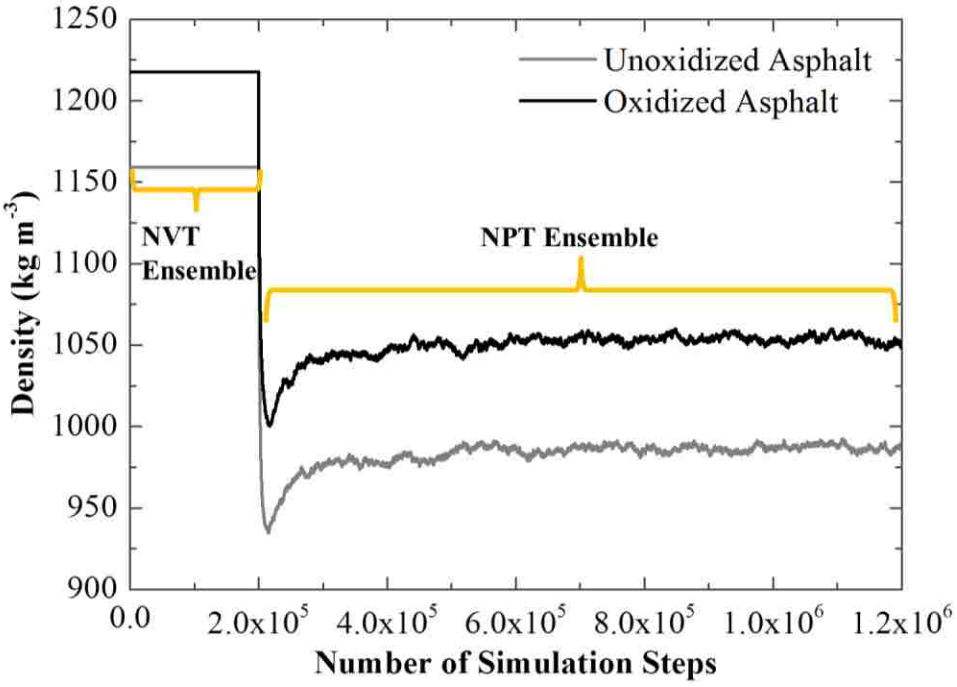

Figure 3.12 Density simulation results of asphalt before and after oxidative aging at 25 ℃

3.4.2.1 T-Test Results

In this study, two sample t-test was used to examine whether two simulations with different cutoff radiuses or time steps are different regarding density means in RStudio. The density values after equilibrium (after 400,000 simulation steps) were compared by randomly selecting 1000 groups of data. Satterthwaite's method was used with no requirement for equal population standard deviations. The significance level α of the test is set at 5%, which is the probability of rejecting the null hypothesis given that is true. P-value is used for testing the hypothesis, which is the probability of observing a test statistic at least at extreme as the one observed assuming the null hypothesis is true. If p-value is larger than 5% (0.05) after the test, it can be concluded that there is no significant difference between two simulations with different cutoff radiuses or time steps.

Table 3.2 lists the t-test results. It can be seen that there is no significant differences between different cutoff radiuses and different time steps. All the p-values after tests are larger than 0.05 and the average density values are similar to each other. Therefore, there are no significant difference between the simulation results using different cutoff radiuses and time steps.

Table 3.2 T-test Results

	Average Density ($kg\ m^{-3}$)	Standard Deviation	p-value
Different Cutoff Radiuses for Unoxidized Asphalt			
7.5 Å	973.73	1.63	0.24
17 Å	973.60	2.98	
Different Cutoff Radiuses for Oxidized Asphalt			
7.5 Å	1054.40	1.52	0.18
17 Å	1054.29	2.09	
Different Time Steps for Unoxidized Asphalt			
0.1 fs for NVT 0.5 fs for NPT	973.73	1.63	0.74
0.2 fs for NVT 0.3 fs for NPT	973.75	1.48	
Different Time Steps for Oxidized Asphalt			
0.1 fs for NVT 0.5 fs for NPT	1054.40	1.52	0.16
0.2 fs for NVT 0.3 fs for NPT	1054.49	1.13	

3.4.2.2 Parameter Selection

The selection of the cutoff radius and time step, especially for the time step is very important to perform the MD simulation. The cutoff radius shall be less than half of the box size as discussed above (maximum 17 Å in this study) and the larger the cutoff radius causes longer simulation time. In this study, The SPME method used for handling long-range electrostatic and van der Waals interactions allowed to set the cutoff radius as small

as 7.5 Å. Therefore, 7.5 Å and 17 Å were chosen for comparison. Since there was no significant difference between the simulation results using the two different cutoff radiuses as discussed above, 7.5 Å was selected as the cutoff radius for later MD simulations.

Similarly, if a large time step is used, the motion of molecule becomes unstable due to the very big error occurring in the integration. Conversely, if a very small time step is used, it will be very inefficient due to a very long calculation time (Ciccotti and Ryckaert 1986). The maximum time step that can be used in a MD simulation is determined by the highest frequency motion within the model. In this study, an all-atom model was used, which included hydrogen atoms, thus the time step shall be no greater than 1 fs and 0.5 fs is usually used as default time step (Fraaije et al. 2014). Moreover, for the relaxation simulation under NVT ensemble, the time step should be as small as possible to guarantee the accuracy of simulation. Therefore, 0.1 fs and 0.2 fs were chosen for NVT ensemble and 0.5 fs and 0.3 fs were chosen for NPT ensemble for comparison. Since there is no significant difference between the simulation results using the two different time steps for either the NVT or the NPT ensemble as discussed above, 0.1 fs and 0.5 fs were chosen as the time steps for NVT and NPT ensembles, respectively, for later MD simulations.

CHAPTER 4

ENERGY CHANGES OF ASPHALT BEFORE AND AFTER OXIDATIVE AGING

This chapter is part of a published paper entitled "Investigation of Asphalt Aging Behaviour Due to Oxidation Using Molecular Dynamics Simulation" in *Molecular Simulation*, which is published online on August 21th, 2015 (Pan and Tarefder 2015a).

4.1 MD Simulation Parameters

As stated in Chapter 3, the selections of MD simulation parameters are as follows: pressure for all the simulations was set at 101.325 kPa (1.0 atm). An NVT ensemble was first used to relax the systems under -173 ℃ (100.15 K) with 0.1 fs time step for 200,000 simulation steps (20 ps); an NPT was then used to simulate the realistic asphalt systems and to obtain the density of model asphalt systems at 25 ℃ (298 K) with 0.5 simulation time step was 0.5 fs for 1,000,000 simulation steps (0.5 ns), which were long enough to guarantee the system to reach the equilibrium state with stable volume and energy fluctuation. Berendsen thermostat and barostat were used for the purpose of maintaining the selected statistical ensembles at a constant temperature and pressure respectively. The Smooth particle mesh Ewald (SPME) method was used for handling long-range electrostatic and van der Waals interactions.

4.2 Calculation of Bulk Modulus and Zero Shear Viscosity

The bulk modulus, *K* was calculated after simulations, which measures the material's resistance to uniform compression by Tildesley and Allen's (1987) method:

$$K = -V\left(\frac{\partial P}{\partial V}\right)_T = \frac{< V > k_B T}{\left(< V^2 > - < V >^2\right)}$$

(4.1)

where, *V* is the system volume, *P* is system pressure, *T* is the temperature, and k_B is the Boltzmann constant. Bulk modulus was calculated under the NPT ensemble for the last 1,000,000 simulation steps (500 ps) as aforementioned.

Zero shear viscosity is a measure of the viscosity of a material when a shear stress is acting on it at a shear rate of almost zero, which is an indicator for both stiffness of asphalt binder and its resistance to permanent deformation under long term loading (De Visscher et al. 2004). The zero shear viscosity of equilibrium asphalt systems before and after oxidative aging was calculated by Green-Kubo method (Gordon 2003):

$$\eta = \frac{V}{k_B T}\int_0^\infty < P_{\alpha\beta}^s(0) P_{\alpha\beta}^s(t) > dt \qquad (4.2)$$

where, $P_{\alpha\beta}^S$ is the instantaneous value of the off-diagonal pressure tensor element $\alpha\beta$, *V* is the system volume, T is the temperature, k_B is Boltzmann constant, and *t* is time. The viscosity value was obtained by averaging over the three independent off-diagonal pressure tensor elements, which can improve the convergence of Equation (4.2)

(Tildesley and Allen 1987). The MD simulation for viscosity calculation was conducted under NPT ensemble after system reaching density equilibrium as stated previously at 25 ℃ (298 K). The time step and simulation steps were set at 0.5 fs and 2,000,000 (1 ns), respectively.

4.3 Simulation Results and Discussions

4.3.1 Energy Changes of Asphalt Before and After Oxidation

To prove that hardening happened during oxidative aging, intermolecular energies were examined since macroscopic hardness is generally characterized by strong intermolecular bonds (Callister and Rethwisch 2012). For DREIDING force field, the intermolecular energies include intermolecular van der Waals energy, intermolecular electrostatics energy, and intermolecular hydrogen bonding energy, which were investigated as the attractive intermolecular strength to represent hardness.

The intermolecular energies of model asphalt systems before and after oxidative aging are shown in Figure 4.1. It can be seen from the time dependent data that simulations have researched equilibrium after 400,000 simulation steps, when the data are slightly fluctuated around a fix number. The intermolecular van der Waals energies of asphalt before and after oxidative aging are similar as shown in Figure 4.1(b). However, intermolecular electrostatics energy and intermolecular hydrogen bonding energy of oxidized asphalt are greater in magnitude than the unoxidized asphalt as shown in Figure 4.1(c) and Figure 4.1(d), respectively. Overall, the magnitude of total intermolecular energy of oxidized asphalt is much greater than the unoxidized asphalt as shown in

Figure 4.1(a) and the negative sign indicates the work needs to be done to separate the molecules and bonds in the asphalt simulation system. This indicates that the intermolecular bonds in oxidized asphalt are stronger than in the unoxidized asphalt and further proves hardening happened after oxidative aging from molecular mechanics perspective. Moreover, the structures of the asphalt systems before and after oxidation after simulations have been further examined, which are shown in Figure 4.2(a) and (b), respectively. It can be seen that the oxidized asphalt system agglomerates more than the unoxidized asphalt after simulation due to more polar molecules in the oxidized asphalt attracting each other (Pan and Tarefder 2015a). This result is consistent with Lemarchand et al.'s (2013) research conclusion on the chemical aging of asphalt that as asphalt ages, the aggregation process is enhanced due to the nanoaggregation of asphaltene fraction and the diminishment of resin fraction.

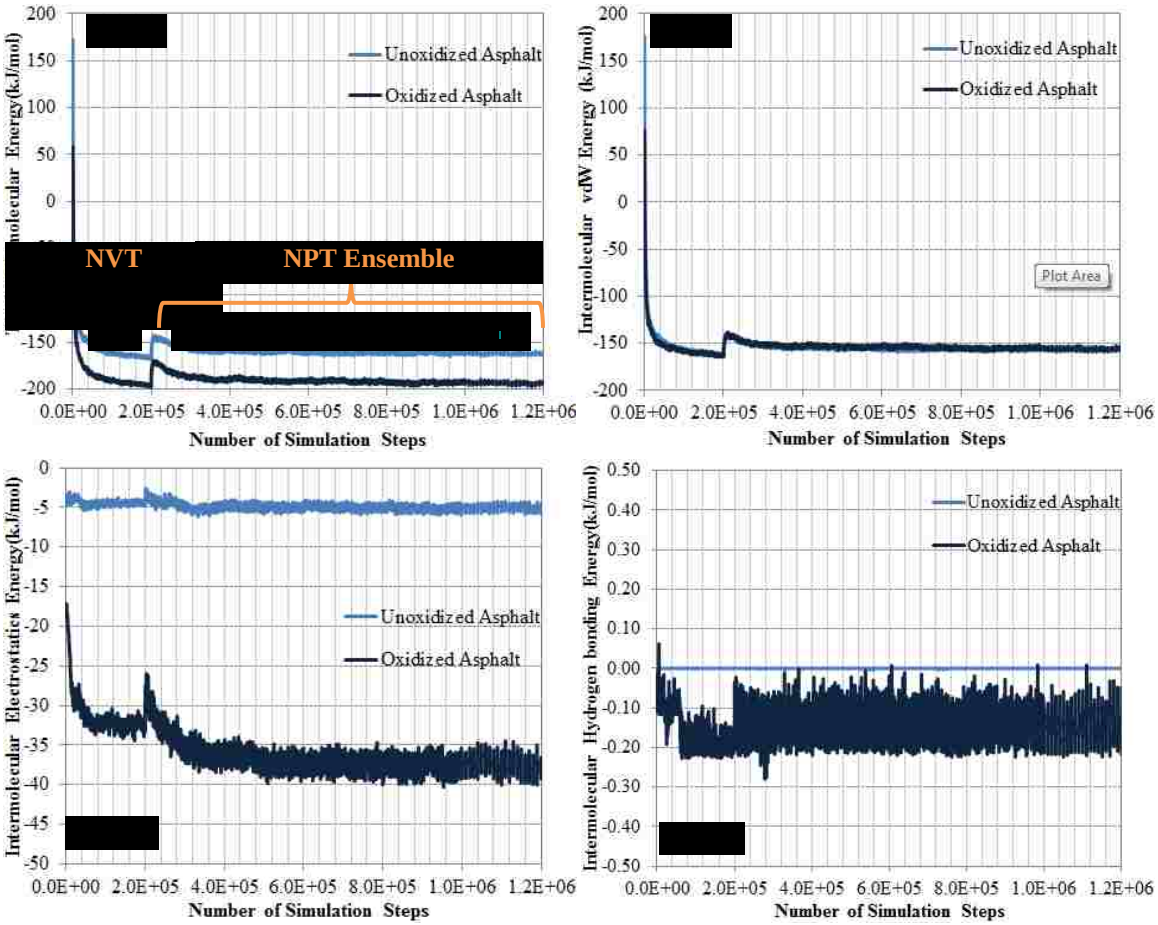

Figure 4.1 Intermolecular energy changes of asphalt before and after oxidative aging with (a) total intermolecular energy comparison, (b) intermolecular van der Waals energy comparison, (c) intermolecular electrostatics energy comparison, and (d) intermolecular hydrogen bonding energy comparison

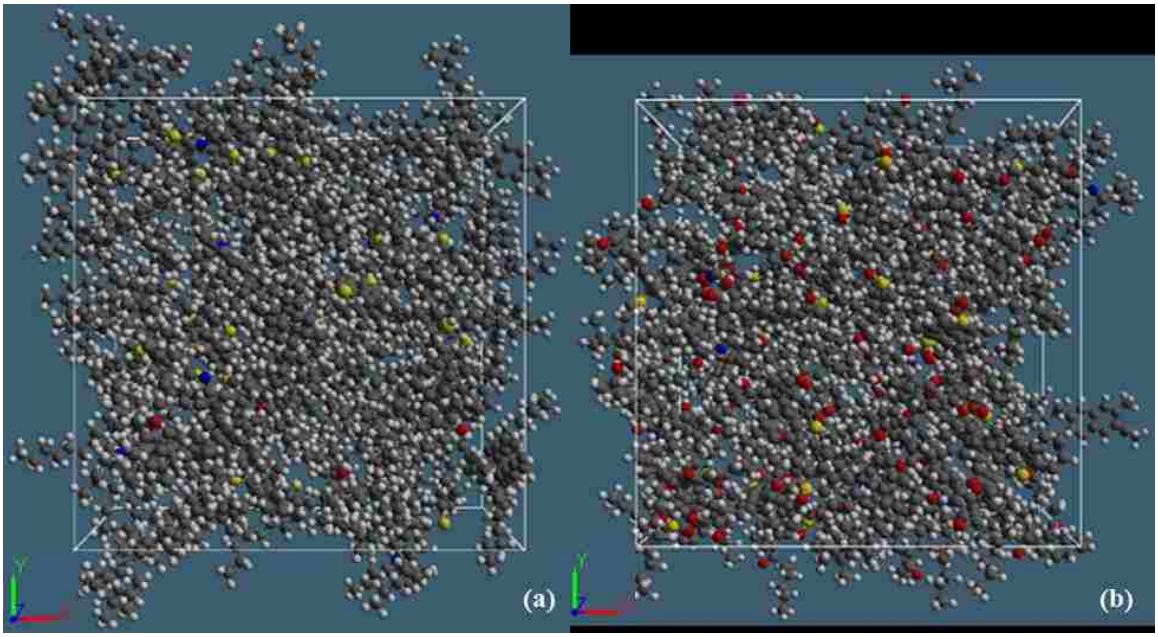

Fig. 4.2 Asphalt systems after MD simulations: (a) unoxidized model asphalt system and (b) oxidized model asphalt system

4.3.2 Density Changes of Asphalt Before and After Oxidation

Figure 4.3 shows the asphalt density change before and after oxidative aging. The average density of oxidized asphalt (approximately 1054 kg m^{-3}) after simulation equilibrium is higher than the unoxidized asphalt (approximately 988 kg m^{-3}). Higher density for oxidized asphalt is also consistent with the stronger intermolecular bonds in the oxidized asphalt system, which cause the molecules in asphalt more attractive to each other and condense the system more after oxidation.

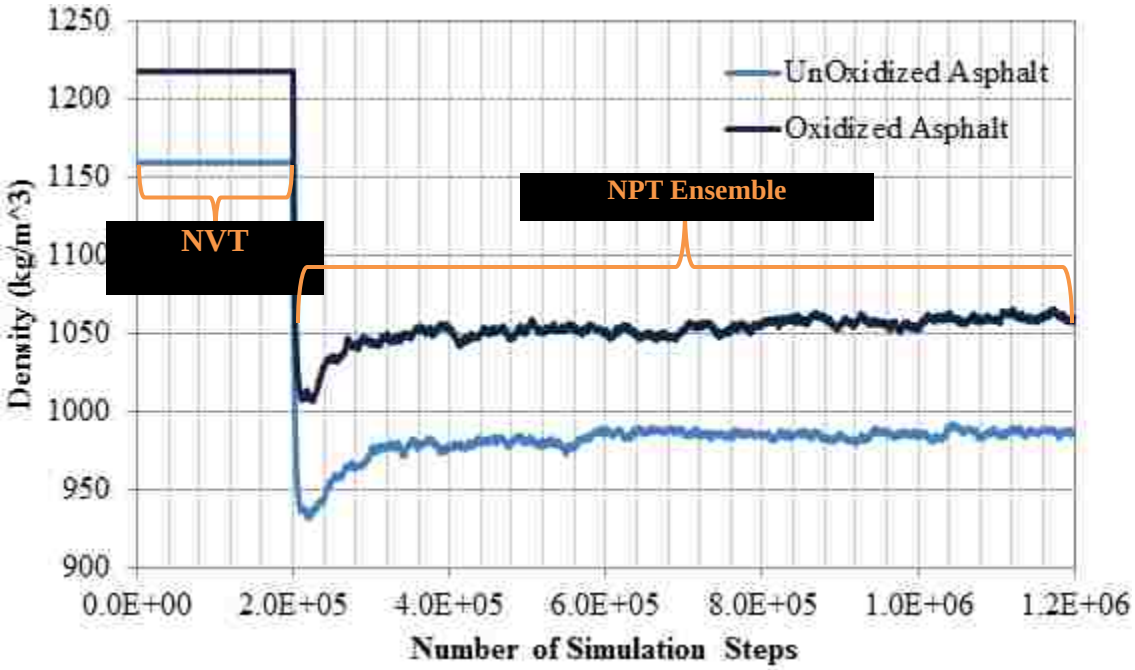

Figure 4.3 Density changes of asphalt before and after oxidative aging

4.3.3 Bulk Modulus Changes of Asphalt Before and After Oxidation

Bulk modulus of the asphalt system before and after oxidative aging was further calculated to understand the relationship between hardness and oxidation. All the calculation values were converged after the simulations as shown in Figure 4.4. The standard deviations for the bulk modulus of asphalt before and after oxidative aging at the last 10,000 simulation steps are 1.7 and 2.3, respectively. The final bulk modulus value of unoxidized asphalt is 730 MPa while the bulk modulus of oxidized asphalt is 829 MPa. Higher bulk modulus of asphalt after oxidative aging indicates that the oxidized asphalt is more resistance to uniform compression and proves that hardening happened in asphalt during oxidation.

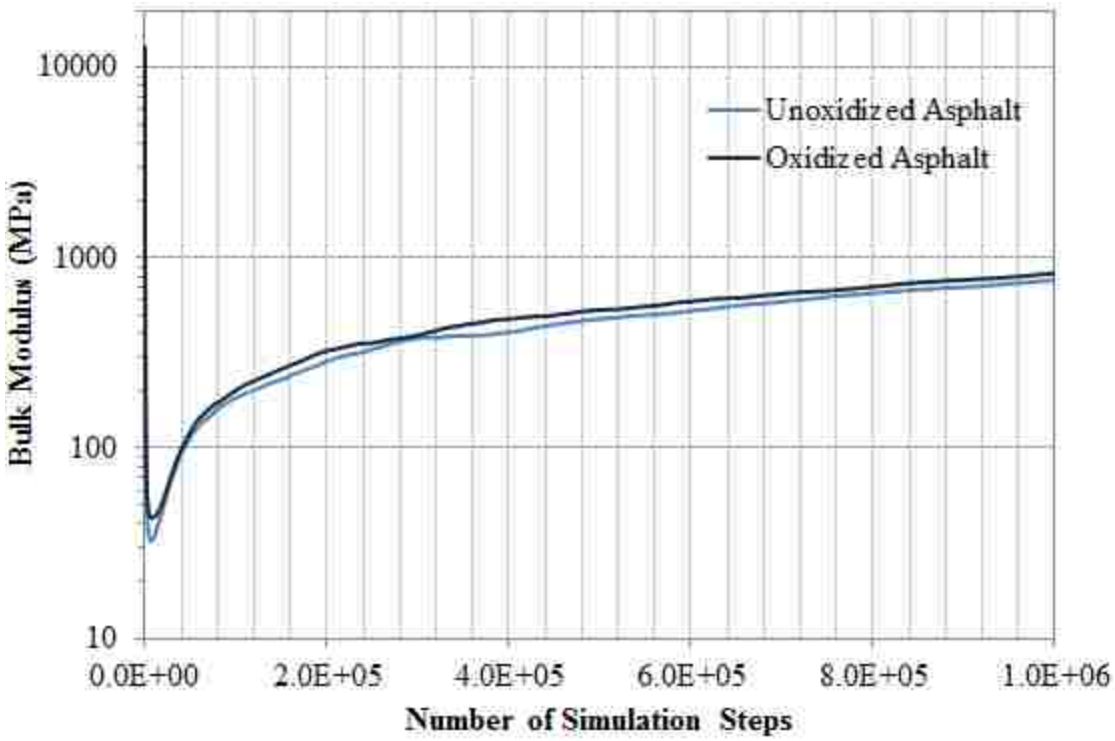

Figure 4.4 Bulk modulus of asphalt before and after oxidative aging

4.3.4 Total Energy and Viscosity Changes Before and After Oxidation

Energy changes in asphalt before and after oxidative aging reveal the physical property changes. Figure 4.5 shows the kinetic, potential changes of unoxidized and oxidized asphalts. It can be seen that the kinetic energy of oxidized asphalt is lower than the un-oxidized asphalt. However, the potential energies of asphalt after oxidative aging are much higher than the asphalt before oxidative aging. This suggests that the formation of strongly interacting components in oxidative aged asphalt, which might be responsible for increasing viscosity and altering complex flow properties (Pan and Tarefder 2015b).

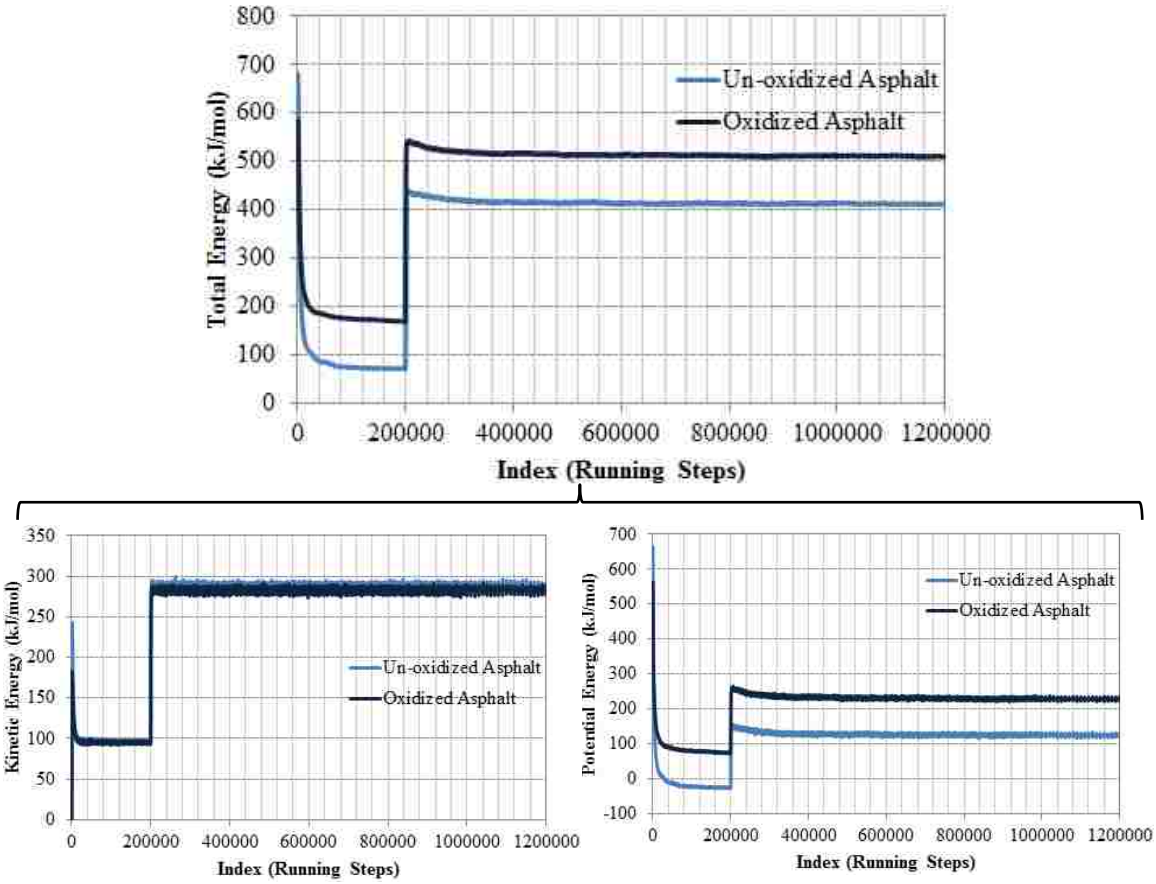

Figure 4.5 Total energy changes of asphalt before and after oxidative aging

Zero shear viscosities of asphalt before and after oxidative aging are shown in Figure 4.6. The viscosity of oxidized asphalt is substantially much higher than the unoxidized asphalt. This is consistent with Lemarchand et al.'s (2013) research on the chemical aging of the Cooee asphalt model, who concluded that enhanced aggregation process after asphalt aging resulted in a viscosity increase. The final viscosity value of unoxidized asphalt is approximately 5.6×10^4 Pa s while the viscosity of oxidized asphalt is approximately 7.8×10^4 Pa s. The standard deviations for the zero shear viscosities of asphalt before and after oxidative aging at the last 100,000 simulation steps are 1.2 and 5.3, respectively. This proves that the simulation steps were long enough to provide

stable viscosity values. These values are consistent with Traxler's (1962) research on the temperature-viscosity data on asphalt cements. The range of viscosity of asphalt under (25 ℃) 298 K is from 3.6×10^{4} Pa s to 1.44×10^{5} Pa s (Traxler 1962). The increase of viscosity indicates that asphalt is stiffer after oxidative aging.

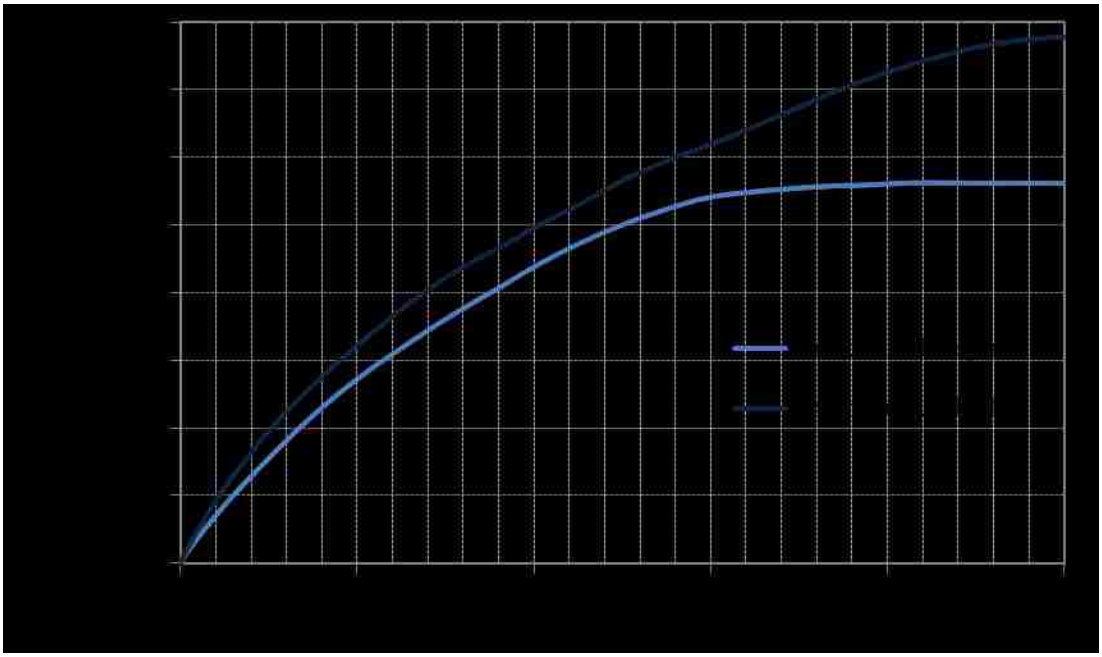

Figure 4.6 Zero shear viscosity changes of asphalt before and after oxidative aging

In sum, the intermolecular interactions in the asphalt systems govern the physical properties of asphalt before and after oxidative aging. Specifically, when the magnitudes of intermolecular energies underlying the oxidized asphalt system increase while the kinetic energy decreases after MD simulation, the oxidized asphalt shows an increase in viscosity.

4.4 Conclusions

Oxidized functional groups in asphalt molecules increase the strength of intermolecular bonds of asphalt, which causes agglomeration of the system and further contributes to the hardening of the oxidized asphalt. The internal property change is consistent with the external physical and rheological property change after oxidation, which is revealed by the increase of density, bulk modulus and viscosity. Specifically, it can be concluded that the internal energy changes, especially for higher magnitude of intermolecular and lower kinetic energies, are responsible for the hardening of oxidized asphalt, and the higher potential energies in oxidized asphalt further proves that oxidation increases the polarity of molecules in asphalt and forms strongly interacting components.

CHAPTER 5

MECHANICAL PROPERTIES OF ASPHALT BEFORE AND AFTER OXIDATIVE AGING

This chapter is part of a published paper entitled "Investigation of Asphalt Aging Behaviour Due to Oxidation Using Molecular Dynamics Simulation" in *Molecular Simulation*, which is published online on August 21th, 2015 (Pan and Tarefder 2015a).

5.1 Simulation Parameters

To analyze how the mechanical properties of asphalt change under the effects of oxidative aging, MD simulations were subsequently conducted for both unoxidized and oxidized asphalts under the NPxPyPzT ensemble and 25℃ (298 K) after density simulations, which enabled for applying stress on either the X, Y or Z direction of the simulation box. Three different stress rates for both compressive stress and tensile stress were selected and applied in Y direction as 284 GPa sec^{-1} (2,800,000 atm sec^{-1}), 709 GPa sec^{-1} (7,000,000 atm sec^{-1}), and 993 GPa sec^{-1} (9,800,000 atm sec^{-1}), which correspond to 0.002 mN s^{-1}, 0.005 mN s^{-1}, and 0.007 mN s^{-1} loading rates, respectively, according to the sizes of the simulation boxes after reaching the density equilibrium. These loading rates were selected from the Tarefder and Faisal's (2013a) study about the nanoindentation behavior of asphaltic materials to prevent the thin film of asphalt binder from hitting the glass substrate. Another reason for the selection of the above stress rates was that these stress rates were applied to detect the mechanical failure behavior of asphalt materials from slow rate to fast rate. 0.5 fs time step and 1,000,000 simulation steps (0.5 ns) were

used for each stress rate applied to guarantee enough simulation time to observe nanoscale failure of asphaltic materials. Andersen thermostat and barostat were used for the stress simulations. The Smooth particle mesh Ewald (SPME) method was also used for handling long-range electrostatic and van der Waals interactions.

5.2 Mechanical Property Changes Before and After Oxidative Aging

5.2.1 Effect of Different Compressive Stress Rates on Asphalt Before and After Oxidative Aging

Under the three different compressive stress rates in Y direction, the simulations for both unoxidized and oxidized asphalt systems failed under 709 GPa sec^{-1} and 993 GPa sec^{-1} (7,000,000 atm sec^{-1} and 9,800,000 atm sec^{-1}) within 1,000,000 simulation steps, because the lengths of both the unoxidized and oxidized asphalt simulation boxes in the Y direction had been compressed to less than the cutoff radius in the periodic boundary conditions to keep the number of the molecules in the simulation box constant for further simulations. The simulation results are shown in Figure 5.1. It can be seen that for both unoxidized and oxidized asphalts, the compressive depth in the Y direction increases faster with the increase of compressive stress rate and the simulation fails faster with the increase of compressive stress rate. Figure 5.2 shows the configurations of asphalt systems before and after oxidation under 284 GPa sec^{-1} stress rate in Y direction that the simulations did not fail. It can be seen that the unoxidized asphalt is compressed more than the oxidized asphalt in Y direction after simulation. The trend of the simulation results is consistent with the trend of laboratory test results obtained by the study of Tarefder and Faisal (2013a) about the nanoindentation behavior of long-term aged

asphalt under different compressive loading rates. In reality, it is difficult to test unoxidized (unaged) asphalt binder under nanoindenter because of its low stiffness and viscous behavior at room temperature. However, the MD simulation in nanoscale can successfully conduct the test at any temperature. Therefore, this study has a relative advantage in investigating the nanomechanical behavior of asphalt material at realistic temperature and pressure conditions.

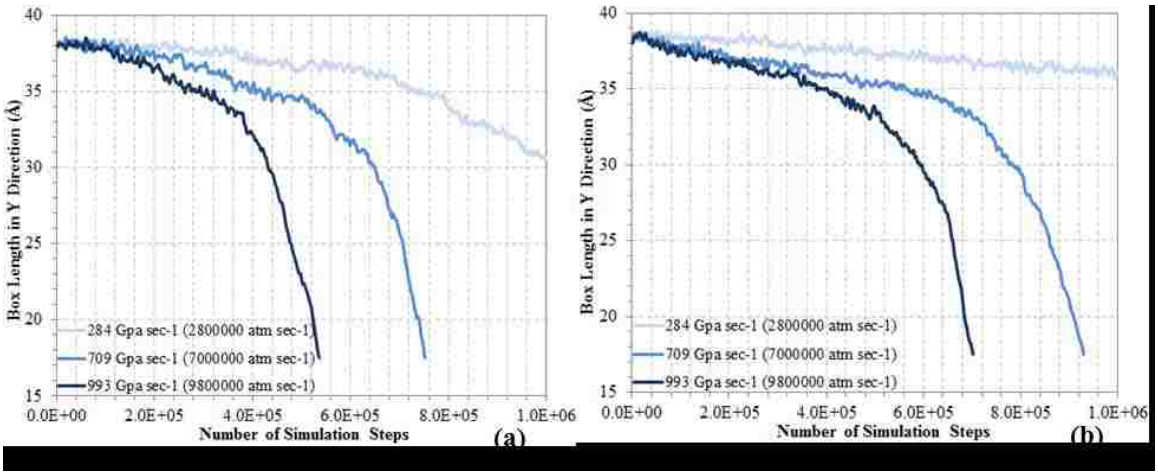

Figure 5.1 Simulation results of unoxidized and oxidized asphalts under different compressive stress rates in Y direction with (a) unoxidized asphalt and (b) oxidized asphalt

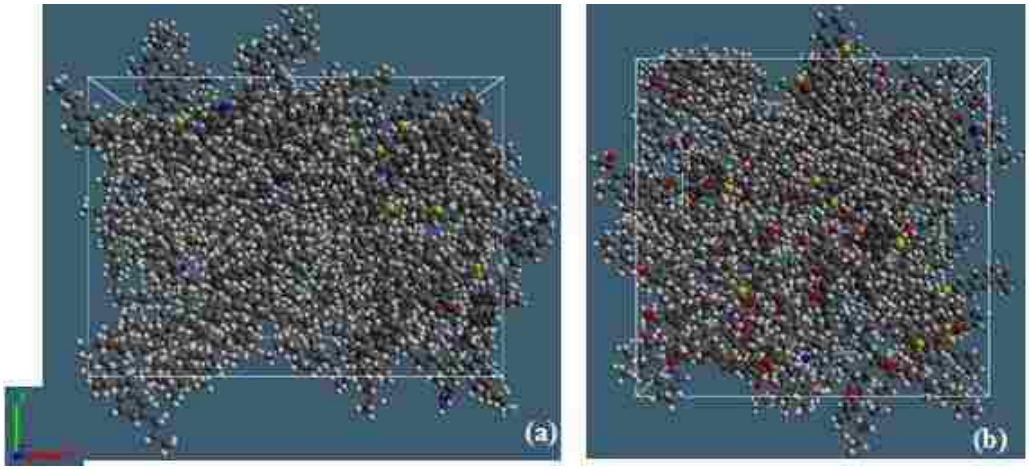

Figure 5.2 Configurations of asphalt systems before (a) and after (b) oxidation under compressive stress rate of 284 GPa sec^{-1}

The stress-strain curves of asphalt systems in Y direction before and after oxidative aging were also calculated after simulations as shown in Figure 5.3. It can be seen that oxidized asphalt is subject to higher stress to reach the same strain as the unoxidized asphalt, which suggests the stronger hardness of oxidized asphalt. Moreover, the stress-strain change trends for both unoxidized and oxidized asphalts are different under different stress rates.

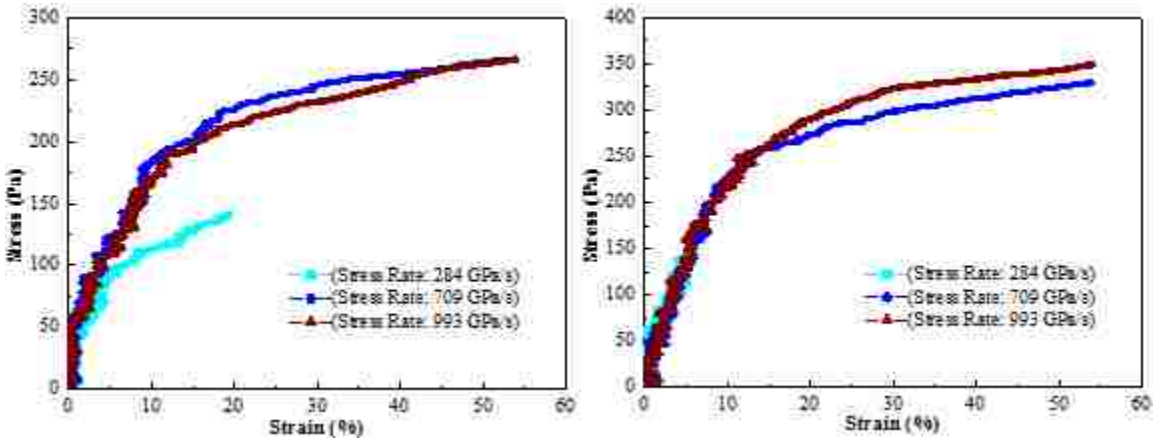

Figure 5.3 Stress-strain curves for asphalt system before (a) and after (b) oxidation under different compressive stress rates

Figure 5.4 shows the further comparison of the different mechanical behaviors of unoxidized and oxidized asphalts under different stress rates. It can be seen that oxidized asphalt is compressed slower than unoxidized asphalt. This further proves that the oxidative aging process increases the hardness of asphalt due to stronger intermolecular bonds. Figure 5.5 shows the stress-strain curves for unoxidized and oxidized asphalts under different stress rates. It can be seen that oxidized asphalt is stiffer or harder than unoxidized asphalt.

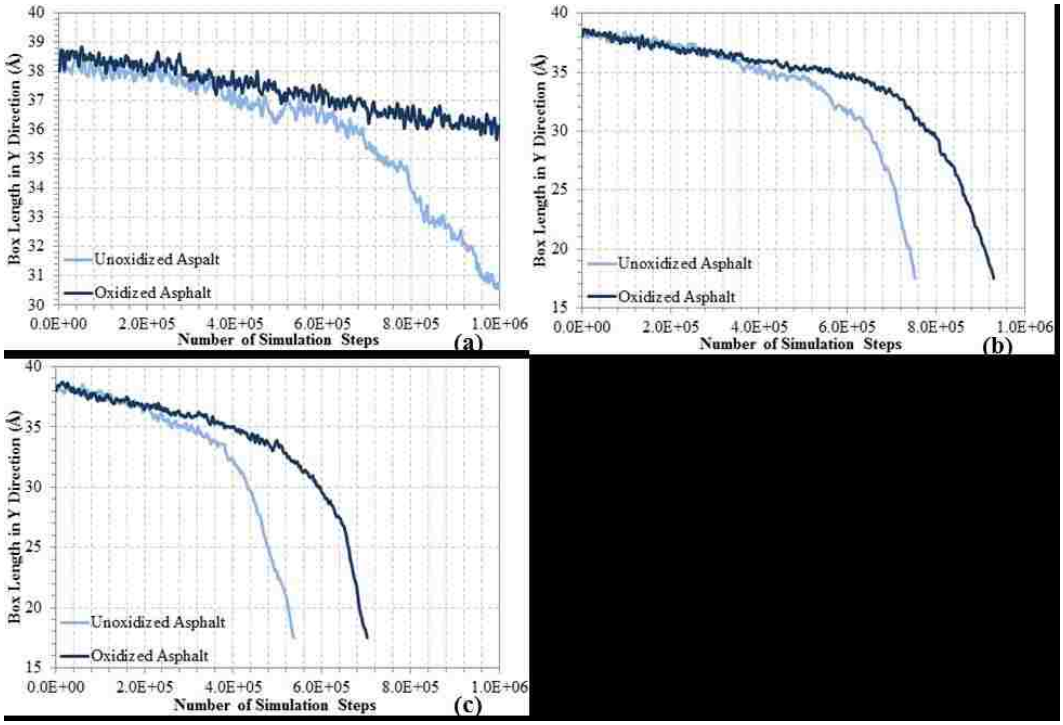

Figure 5.4 Comparison of unoxidized and oxidized asphalts under different compressive stress rates: (a) 284 GPa sec^{-1}, (b) 709 GPa sec^{-1}, and (c) 993 GPa sec^{-1}

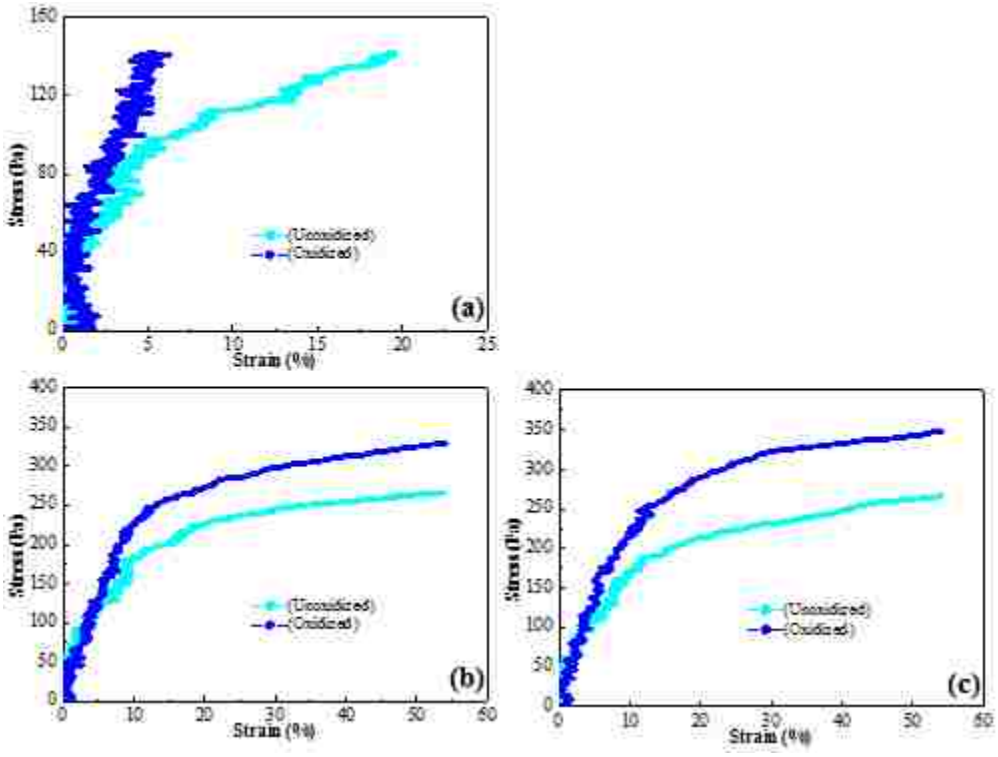

Figure 5.5 Stress-strain curves for unoxidized and oxidized asphalts under different compressive stress rates: (a) 284 GPa sec^{-1}, (b) 709 GPa sec^{-1}, and (c) 993 GPa sec^{-1}

5.2.2 Effect of Different Tensile Stress Rates on Asphalt Before and After Oxidative Aging

Under the three different tensile stress rates in Y direction, the simulations for both unoxidized and oxidized asphalt systems failed under 709 GPa sec^{-1} and 993 GPa sec^{-1} (7,000,000 atm sec^{-1} and 9,800,000 atm sec^{-1}) within 1,000,000 simulation steps, because the lengths of both the unoxidized and oxidized asphalt simulation boxes in the X or Z direction were compressed to less than the cutoff radius in the periodic boundary conditions to keep the number of the molecules in the simulation box constant for further simulations, according to the tension in the Y direction. Figure 5.6 shows the simulation results. It can be seen that for both unoxidized and oxidized asphalts, the tensile length in the Y direction increases with the increase of tensile stress rate from 284 GPa sec^{-1} to 709 GPa sec^{-1}. However, the simulation boxes fail at a shorter tensile length under stress rate of 993 GPa sec^{-1}, compared to the stress rate of 709 GPa sec^{-1}. Moreover, the simulation fails faster with the increase of tensile stress rate. Figure 5.7 shows the configurations of asphalt systems before and after oxidation under 284 GPa sec^{-1} stress rate in Y direction that the simulations did not fail. It can be seen that the unoxidized asphalt is elongated more than the oxidized asphalt in Y direction after simulation.

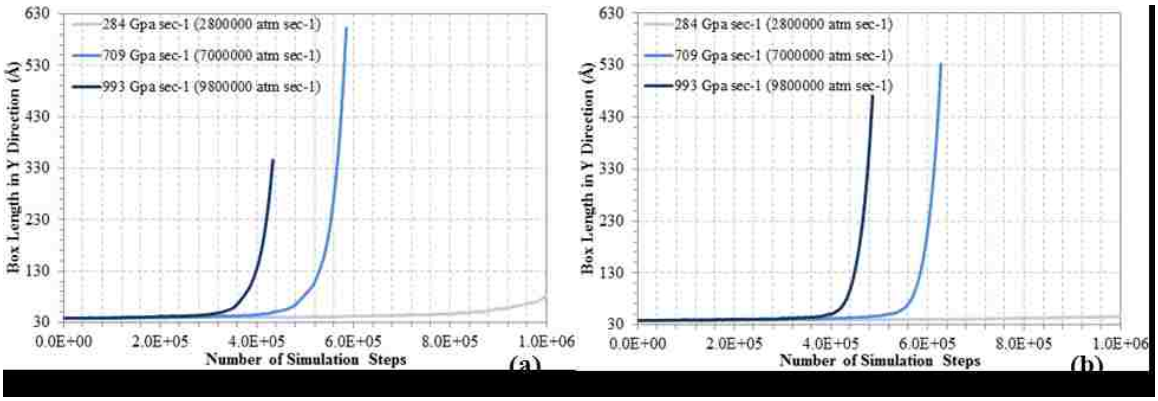

Figure 5.6 Simulation results of unoxidized and oxidized asphalts under different tensile stress rates in Y direction with (a) unoxidized asphalt and (b) oxidized asphalt

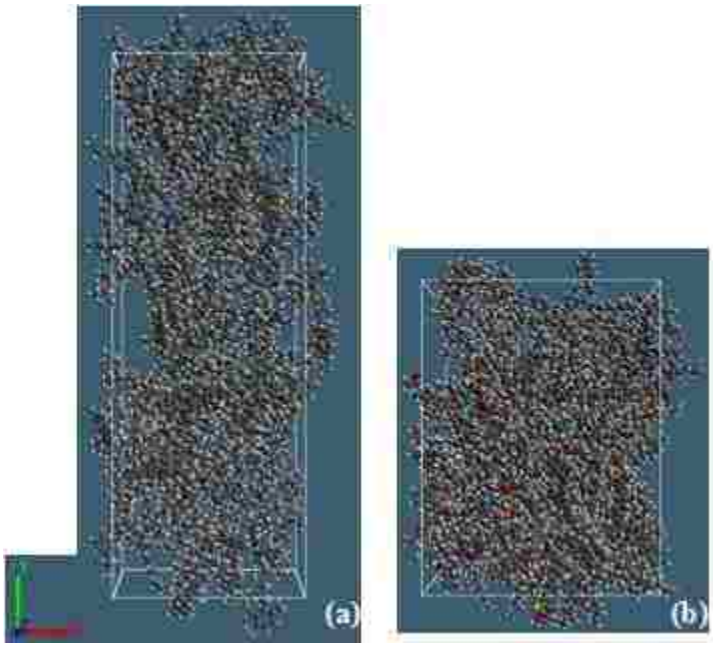

Figure 5.7 Configurations of asphalt systems before (a) and after (b) oxidation under tensile stress rate of 284 GPa sec^{-1}

The stress-strain curves of asphalt systems in Y direction before and after oxidative aging were also calculated after simulations as shown in Figure 5.8. It can be seen that oxidized asphalt is subject to higher stress to reach the same strain as the unoxidized asphalt and fails at a higher strain, which suggests the stronger hardness of oxidized asphalt. Moreover, the stress-strain change trends for both unoxidized and oxidized asphalts are

different under different stress rates. Both asphalt systems fail earlier with an increase in tensile stress rate.

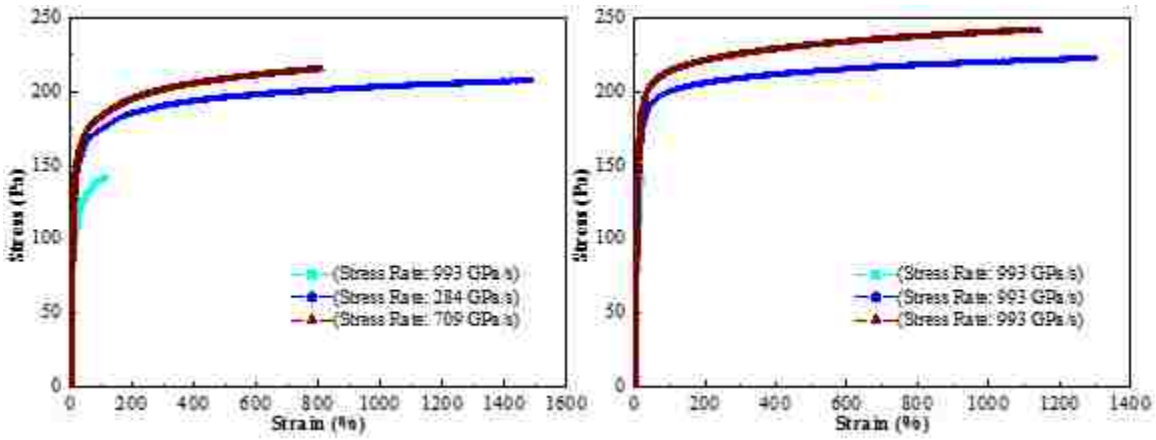

Figure 5.8 Stress-strain curves for asphalt system before (a) and after (b) oxidation under different tensile stress rates

To further compare the different mechanical behaviors of unoxidized and oxidized asphalts under different tensile stress rates, Figure 5.9 illustrates the comparison results. It can be seen that the unoxidized asphalt is easier to be damaged than the oxidized asphalt, which fail under a lower tensile strength. This indicates the stiffness of asphalt increases after oxidative aging. Another observation from Figure 5.9 is that the oxidized asphalt fails at a smaller tensile length, compared to the unoxidized asphalt from the stress rate of 284 GPa sec^{-1} to the stress rate of 709 GPa sec^{-1}, which proves the hardening of asphalt after oxidative aging. However, under the stress rate of 993 GPa sec^{-1}, the unoxidized asphalt fails at a shorter tensile length than the oxidized asphalt, which indicates that the unoxidized asphalt is less viscous than the oxidized asphalt to resist higher tensile stress rate due to weaker intermolecular bonds. Figure 5.10 shows the

stress-strain curves for unoxidized and oxidized asphalts under different stress rates. It can be seen that oxidized asphalt is stiffer or harder than unoxidized asphalt.

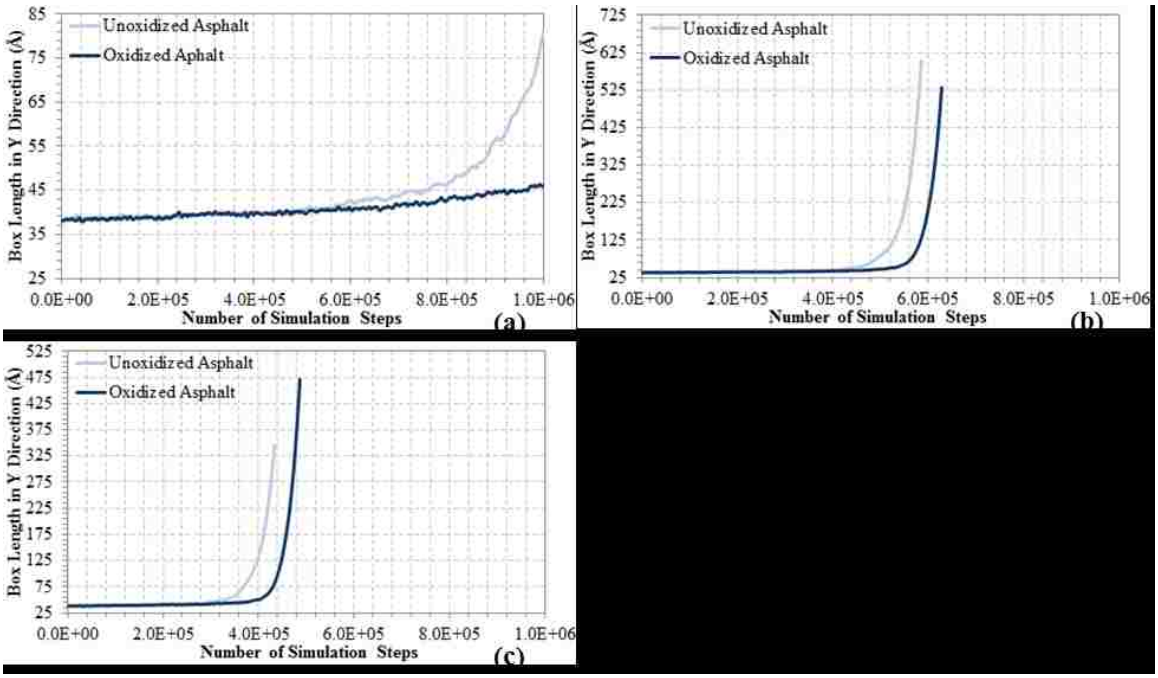

Figure 5.9 Comparison of unoxidized and oxidized asphalts under different tensile stress rates: (a) 284 GPa sec^{-1}, (b) 709 GPa sec^{-1}, and (c) 993 GPa sec^{-1}

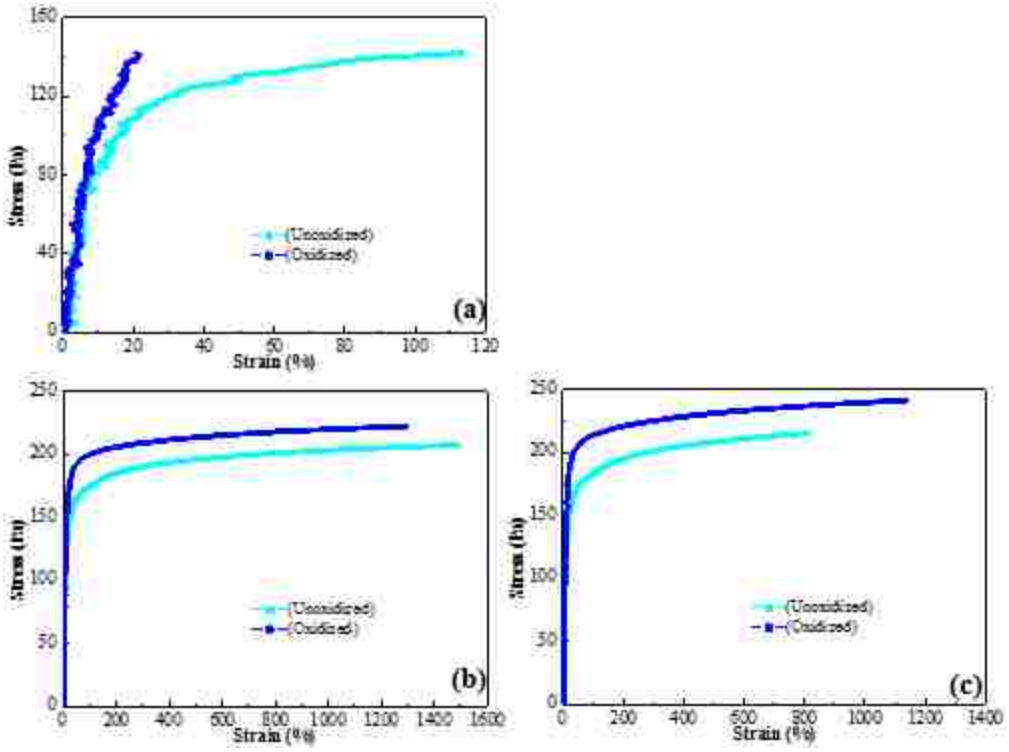

Figure 5.10 Stress-strain curves for unoxidized and oxidized asphalts under different tensile stress rates: (a) 284 GPa sec^{-1}, (b) 709 GPa sec^{-1}, and (c) 993 GPa sec^{-1}

The difference between compressive and tensile stresses applied on asphalt before and after oxidative aging is that asphalt fails easier under tensile stress. From Figure 5.4 and Figure 5.9, it can be seen that both unoxidized and oxidized asphalts fail sooner under tensile stress. The asphalts under the tensile stress rate of 709 GPa sec-1 fail before 630,000 simulation steps, while they fail after 750,000 simulation steps under the same magnitude of compressive stress rate. In the same way, the asphalts under the tensile stress rate of 993 GPa sec-1 fail before 490,000 simulation steps, while they fail after 530,000 simulation steps under the same magnitude of compressive stress rate.

5.3 Conclusions

For both unoxidized and oxidized asphalts under different compressive and tensile stress rates, the deformation increases faster with the increase of stress rates. The hardening of oxidized asphalt is also revealed by its mechanical property change. Overall, the oxidized asphalt deforms slower and less than the unoxidized asphalt under both compressive and tensile stresses.

The comparison between different compressive and tensile stress rates applied on both unoxidized and oxidized asphalts show that asphalts under different tensile stress rates fail faster than under the same magnitudes of compressive stress rates.

CHAPTER 6

RESPONSES OF ASPHALT BEFORE AND AFTER OXIDATIVE AGING TO TEMPERATURE CHANGES

This chapter is part of a submitted paper entitled "A Study of Temperature and Moisture Impacts on Asphalt Before and After Oxidation Using Molecular Dynamics Simulations" in *Computational Materials Science*, which was submitted on June 30th, 2015 with Manuscript Number "COMMAT-D-15-01027" (Pan and Tarefder 2015c). Another paper, entitled "Investigation of Oxidation Effect on the Properties of Asphalt under Different Temperatures Using Molecular Simulation and Laboratory Testing", is also partially included in this chapter, which was accepted for presentation at *Transportation Research Board (TRB) 95th Annual Meeting* with Manuscript Number "16-5680" (Pan et al. 2016a).

6.1 Simulation Parameters

As stated in Chapter 3, the simulation system was first relaxed using an NVT ensemble - 173 ℃ (100.15 K). The time step was set at 0.1 fs with 200,000 running steps (20 ps). An NPT ensemble was then used to simulate the realistic asphalt systems and to obtain the densities of the model asphalt systems under a temperature range from -35℃ to 160 ℃ (238.15 K to 433.15 K), with a temperature increment of 15 ℃. This temperature range covers the pavement conditions from cold winter to asphalt-aggregate mixing temperatures. The simulation time step was set at 0.5 fs with 1,000,000 running steps (500 ps) to guarantee the system could reach equilibrium.

6.2 Thermodynamic Properties of Asphalt Before and After Oxidative Aging

6.2.1 Density

The average density changes of asphalt systems before and after oxidative aging for the last 200,000 equilibrium simulation steps under the NPT ensemble and different temperatures are shown in Figure 6.1. It can be seen from the fitting linear lines that both unoxidized and oxidized densities decrease with an increase in temperature. The density of oxidized asphalt is higher than the unoxidized asphalt with an approximate difference of 60 kg m^{-3}. Another observation from the simulations is that the density of unoxidized asphalt decreases slightly faster than the oxidized asphalt with an increase in temperature. This indicates that temperature has a more adverse effect on unoxidized asphalt.

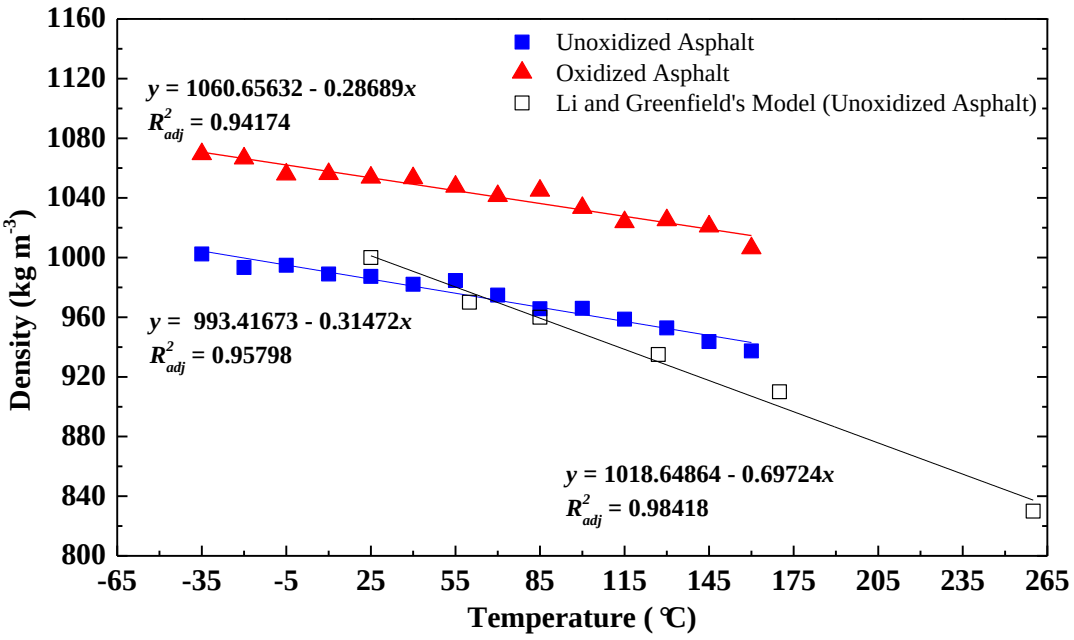

Figure 6.1 Density changes of asphalt before and after oxidative aging under different temperatures compared to Li and Greenfield's (2014) unoxidized asphalt model

Figure 6.1 also shows the comparison of the simulation results between this study and Li and Greenfield's (2014a) study for unoxidized asphalt. It can be seen that for both studies, trend of unoxidized asphalt density change under different temperatures are the same, showing that density of asphalt decreases with an increase in temperature. However, although the same unoxidized asphalt system was used in this study as Li and Greenfield's proposal, the simulation results are not exactly the same as shown in Figure 6.1. According to the linear fit results, the magnitude of slope for density vs. temperature equation in Li and Greenfield's study is higher than the one in this study. It indicates that the density of asphalt model in Li and Greenfield's study decreases faster with an increase in temperature than the density change in this study. The difference might be caused by different simulation parameter and force field selections in the two studies.

Moreover, higher density of oxidized asphalt might be caused by the hardening of asphalt after oxidative aging. Later in this study, this is investigated by the changes of isothermal compressibility and bulk modulus that are used to interpret glass transition behavior change of asphalt due to oxidation.

6.2.2 Isothermal Compressibility and Bulk Modulus

6.2.2.1 Calculation of Isothermal Compressibility and Bulk Modulus

Isothermal compressibility, β_T, measures the fractional change in volume of a system as the pressure changes at constant temperature. The bulk modulus, K, is the inverse of the isothermal compressibility which measures the material's resistance to uniform

compression as mentioned in Chapter 4 using Equation (4.1). These two physical quantities are calculated by Tildesley and Allen (1987):

$$\beta_T = \frac{1}{K} = -V^{-1}\left(\frac{\partial V}{\partial P}\right)_T = \frac{1}{Vk_BT}\left(<V^2> - <V>^2\right) \tag{6.1}$$

where, V is the system volume, P is system pressure, T is the temperature, and k_B is the Boltzmann constant. The simulation parameter selections and procedures are the same as previously mentioned and all the simulations reached equilibrium after 600,000 running steps in volume (after 400,000 running steps in the NPT ensemble with a simulation duration of 1,000,000 running steps). Therefore, both the isothermal compressibility and bulk modulus were calculated under the NPT ensemble for the last 600,000 simulation steps (300 ps). To avoid errors and noises affecting the calculation results for a single temperature point, larger temperature interval were used for analysis. The volume fluctuations after equilibrium under -35 ℃, 40 ℃, 115 ℃, and 160 ℃ (238.15 K, 313.15 K, 388.15K, and 433.15 K) were selected for calculations.

All calculation values were converged after the simulations. One example of the isothermal compressibility and bulk modulus calculation for asphalt before and after oxidative aging under different simulation times at -35 ℃ is shown in Figure 6.2(a) and (b), respectively. It can be seen that the values have converged after 150 ps.

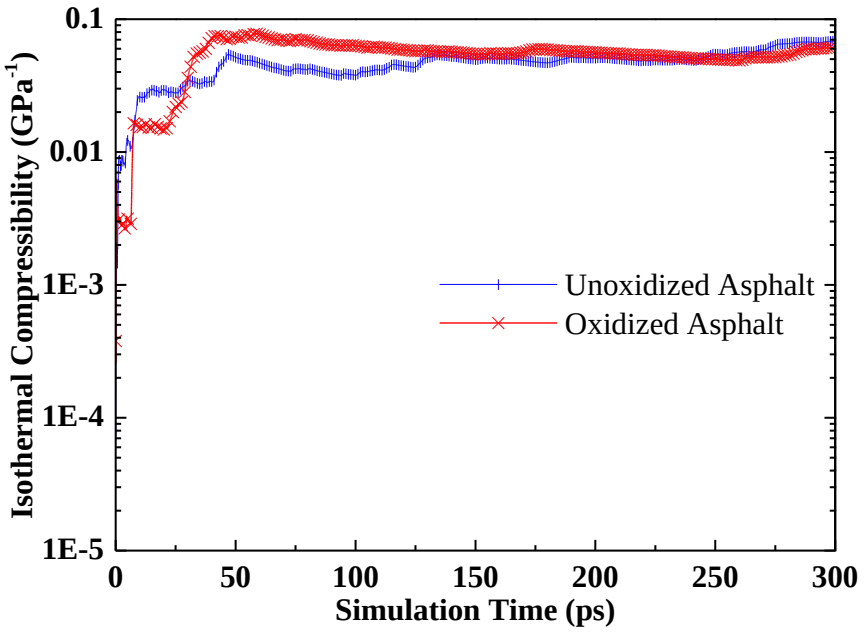

(a)

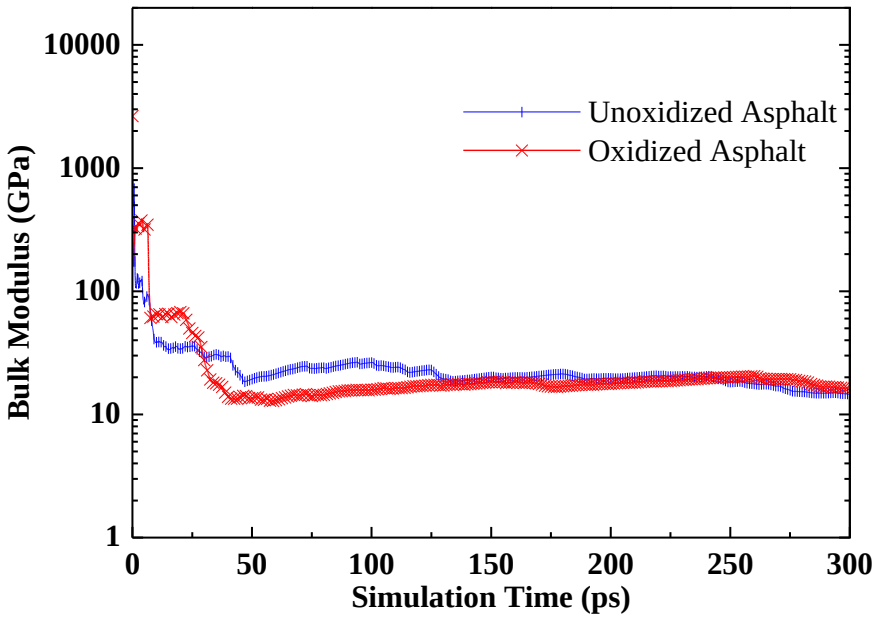

(b)

Figure 6.2 Isothermal compressibility (a) and bulk modulus (b) calculation result versus simulation time at -35 ℃

6.2.2.2 Simulation Results and Discussions

The average values of isothermal compressibility and bulk modulus at the last 50 ps simulation duration under different temperatures are shown in Figure 6.3(a) and (b), respectively. It can be seen that the oxidized asphalt has lower isothermal compressibility and higher bulk modulus compared to unoxidized asphalt, which indicates hardening happened after asphalt oxidation. Moreover, the change trend of isothermal compressibility or bulk modulus under different temperature is different between the unoxidized and oxidized asphalts, which indicates the glass transition behavior of asphalt changes after oxidation. Generally, the isothermal compressibility of both unoxidized and oxidized asphalts increases with an increase in temperature and the bulk modulus shows the opposite trend.

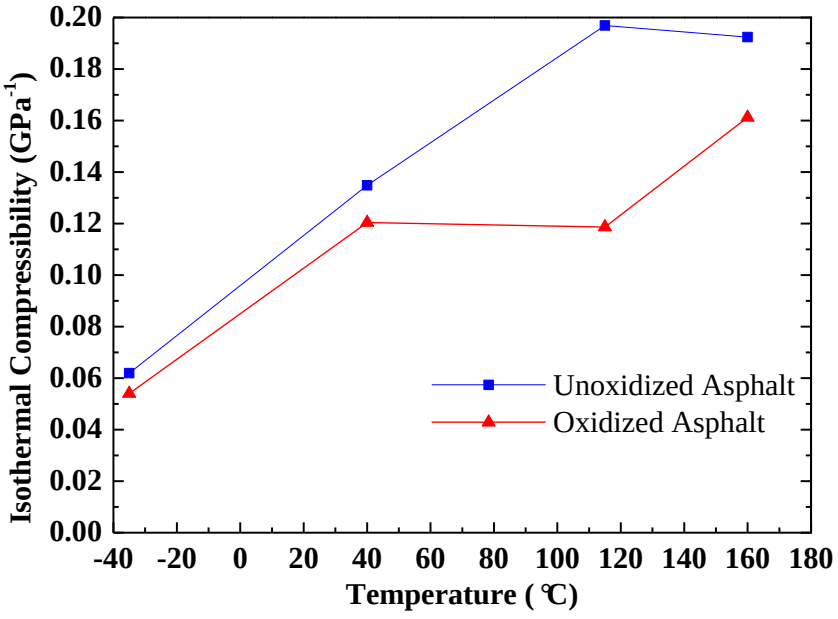

(a)

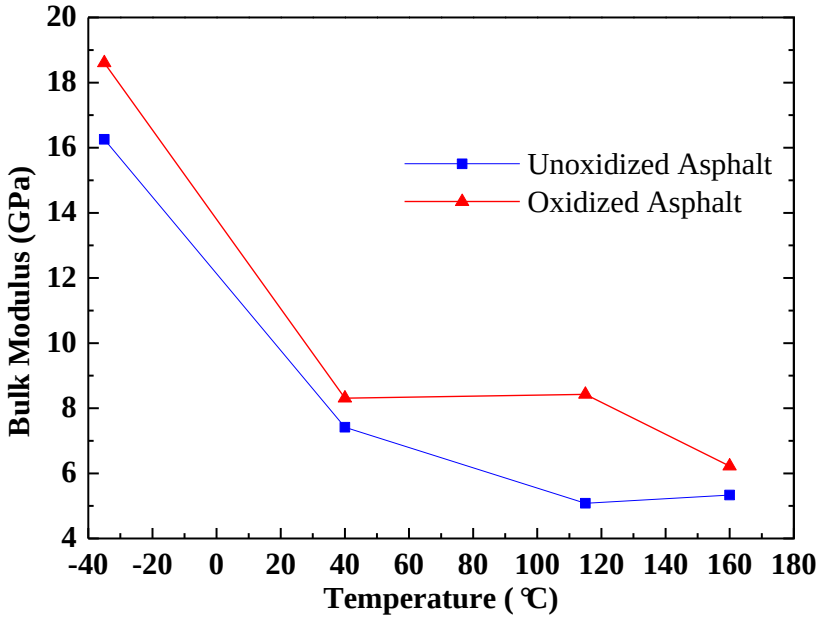

(b)

Figure 6.3 Isothermal compressibility (a) and bulk modulus (b) changes of unoxidized and oxidized asphalts under different temperatures

6.3 Viscosity Responses of Asphalt Before and After Oxidative Aging to Temperature Change

6.3.1 Zero Shear Viscosity Calculation

The zero shear viscosity was calculated in the equilibrium asphalt systems before and after oxidative aging by the Equation (4.2) as discussed in Chapter 4, which is an indicator for both stiffness of asphalt binder and its resistance to permanent deformation under long term loading (De Visscher et al. 2004). The MD simulation for viscosity calculation was conducted under the NPT ensemble after density simulation as stated previously at 25 ℃ and 58 ℃. The time step was set at 0.5 fs with simulation time duration 1000 ps (2,000,000 time steps) with the exception of the viscosity simulation of oxidized asphalt at 25 ℃, which is simulated at 0.5 fs time step with 3000 ps simulation

time duration (6, 000,000 time steps) due to the need of longer simulation time to reach equilibrium for higher viscosity material at low temperature.

6.3.2 Simulation Results and Discussions

Figure 6.4 shows one example of the zero shear viscosity calculation of the unoxidized asphalt using MD simulation at 25 ℃. It can be seen that the simulation has reached equilibrium after 800 ps and it is the same for all other MD simulations. The zero shear viscosity values of asphalt before and after oxidative aging calculated from MD simulations at 25 ℃ and 58 ℃ are shown in Figure 6.5. It can be seen that the zero shear viscosity decreases with an increase in temperature and increases with an increase in the degree of oxidation. The higher viscosity in the higher oxidized asphalt indicates that hardening happens during oxidative aging. The viscosity difference between the two considered temperatures for each type of asphalt is shown in Figure 6.6. It can be seen that the zero shear viscosity decreases more substantially for the oxidized asphalts at higher temperature, for MD simulation. This indicates that the oxidized asphalt is more sensitive to temperature than the unoxidized asphalt regarding viscosity change.

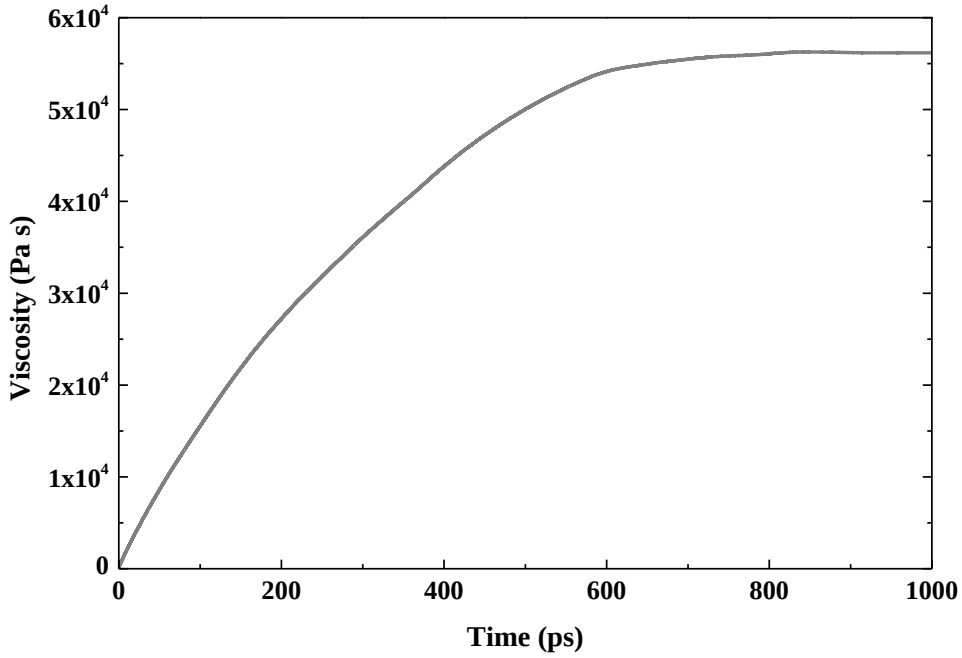

Figure 6.4 Zero shear viscosity of unoxidized asphalt vs. simulation time at 25 ℃

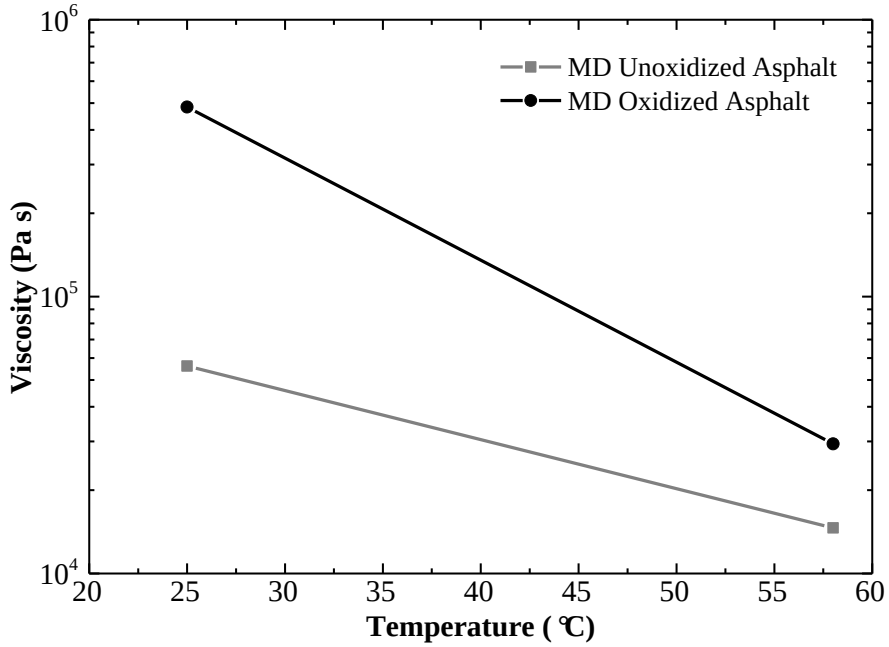

Figure 6.5 Zero shear viscosity of asphalt before and after oxidative aging under different temperatures

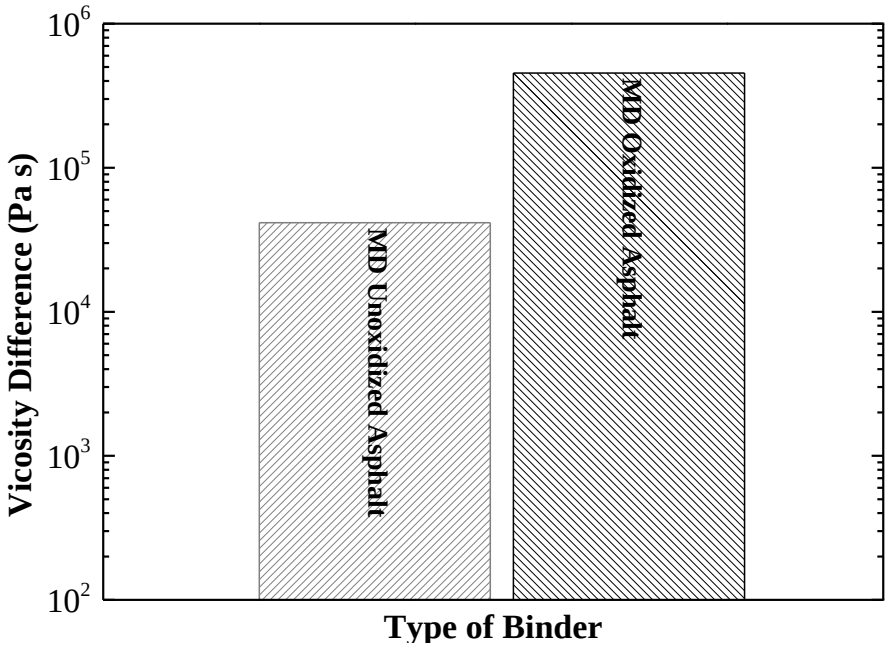

Figure 6.6 Zero Shear Viscosity difference of asphalt between the values under 25 ℃ and 58 ℃

6.4 Laboratory Validation

6.4.1 Density Changes of Asphalt Before and After Oxidation under Different Temperatures

6.4.1.1 Pycnometer Method for Laboratory Testing of Asphalt Density

Superpave performance grading (PG) binders, PG 58-28 and PG 58-22 binders before and after aging has been used for laboratory validations of simulation results. 58 is the high temperature in PG binder to represent average seven-day maximum pavement temperature and -28 and -22 are the low temperatures in the individual PG binder to represent the expected minimum pavement temperature. PG 58-28 was polymer modified binder and PG 58-22 was non-modified binder. The two types of binder was selected because they are close to the SHRP AAA-1 asphalt model proposed in this study,

according to the SHRP Materials Reference Library (Jones 1993). Pycnometer method was used for the density tests under different temperatures. The densities of both unaged/unoxidized and aged/oxidized asphalts under 25 ℃ and 58 ℃ were investigated by Laboratory tests. The testing temperatures were chosen considering the PG binder's high temperature and common ambient temperature. Due to the limitation of temperature control, other temperatures were not considered. PG 58-28 and PG 58-22 binders have been aged through Rolling Thin-Film Oven (RTFO) and Pressure Aging Vessel (PAV) to represent short-term and long-term aging, respectively. The American Society for Testing and Materials (ASTM) standard: ASTM D70, *Standard Test Method for Density of Semi-Solid Bituminous Materials (Pycnometer Method)*, was used for the laboratory density tests of unaged, RTFO aged and PAV aged binders (ASTM International 2009b). There were 3 samples of each type of asphalt binder tested. Figure 6.7 shows the scheme of the laboratory testing for asphalt densities under different temperatures.

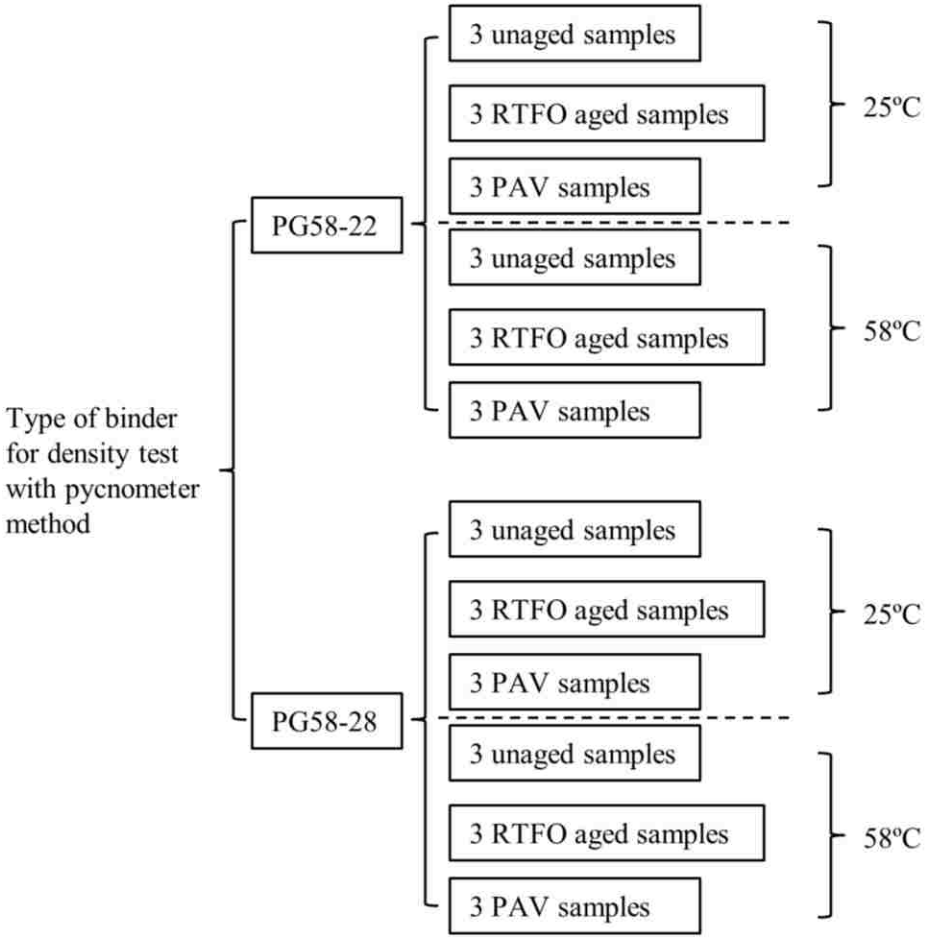

Figure 6.7 Scheme of the laboratory testing for asphalt densities under different temperatures

6.4.1.2 MD Simulation

The densities of both unoxidized and oxidized asphalts models under 25 ℃ and 58 ℃ were investigated by MD simulations. The simulation procedures and parameters are the same as the aforementioned description for asphalt density simulations under different temperatures.

6.4.1.3 Density Validation Results

The average density changes of asphalt systems before and after oxidative aging for the last 200,000 MD simulation steps after equilibrium and the average density changes of unaged, RTFO aged, and PAV aged PG 58-28 and PG 58-22 binders under 25 ℃ and 58 ℃ are shown in Figure 6.8. It can be seen that the simulation results are consistent with the experimental results. The density values of model asphalt systems calculated from MD simulation are close to the density values measured from laboratory tests, which validates the credibility of MD simulations. The density of asphalt decreases with an increase in temperature. Both simulation and experimental results show that the density of asphalt increases with an increase in the degree of oxidation. Another observation is that the density difference for simulation results before and after oxidative aging is larger than the experimental results due to the simulation assumption that there is no any loss of the oily components (saturate fraction) in asphalt by volatility after aging. For laboratory experiment, the RTFO and PAV aged binders must have some oily components loss due to their high temperature and pressure aging conditions (Petersen 1984).

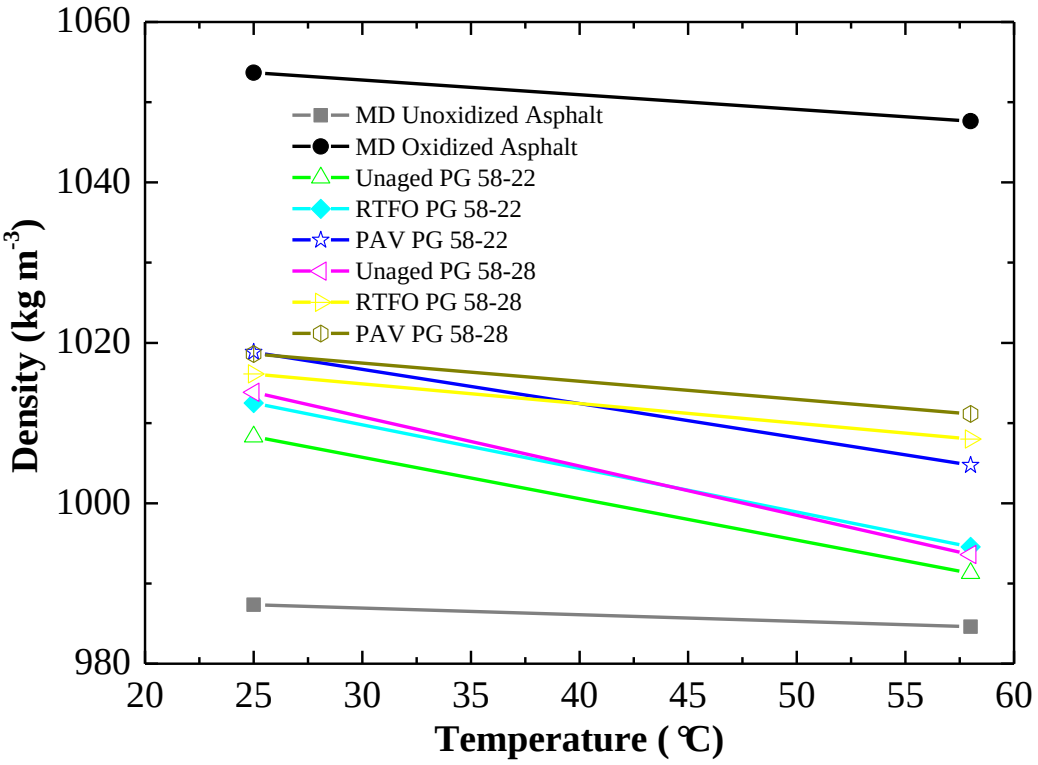

Figure 6.8 Density vs. temperature results from MD simulations and experiments

Moreover, as discussed before, higher density of oxidized asphalt is proved to be caused by the hardening of asphalt after oxidative aging according to MD simulation results in previous chapters regarding isothermal compressibility, bulk modulus and zero shear viscosity changes before and after oxidation. Later in this chapter, laboratory testing results for zero shear viscosity changes in asphalt before and after oxidation are used to validate simulation results and conclusions.

6.4.2 Zero Shear Viscosity Changes of Asphalt Before and After Oxidation under Different Temperatures

6.4.2.1 Dynamic Shear Rheometer (DSR) Testing for Zero Shear Viscosity of Asphalt

Dynamic shear rheometer (DSR) was used for the zero shear viscosity tests of asphalt binders before and after oxidative aging. The DSR is commonly used to characterize the viscous and elastic behavior of asphalt binders at medium to high temperatures. Figure 6.9(a) and (b) show the DSR machine used in this study and the schematic of DSR, respectively. It can be seen that DSR test uses a thin asphalt binder sample sandwiched between two circular plates. The lower plate is fixed while the upper plate can oscillate back and forth across the sample at a certain frequency and temperature by applying a certain stress to create a shearing action.

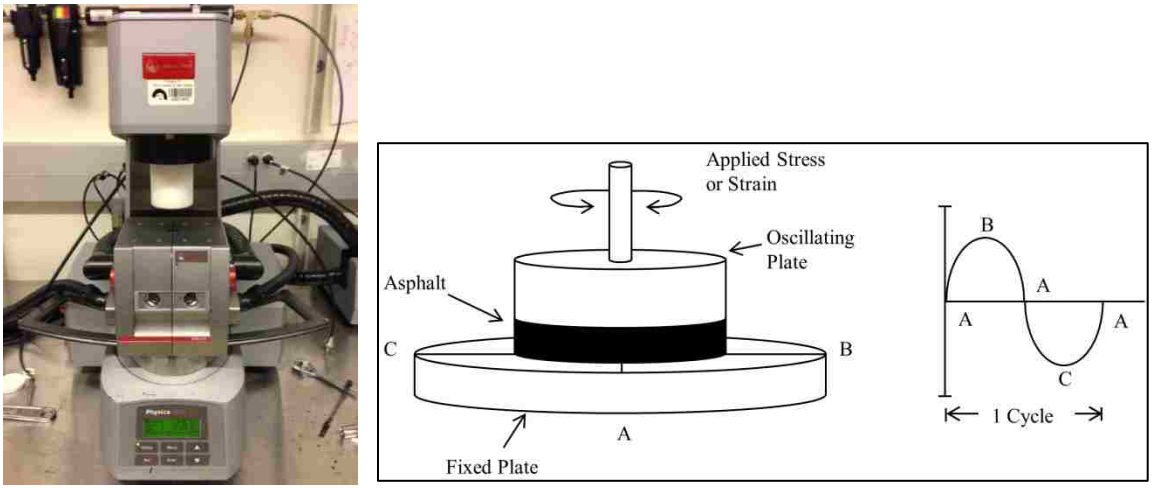

(a) (b)

Figure 6.9 DSR machine (a) and schematic of DSR (b)

The zero shear viscosity measured in this study is being given more attention by researchers recently as a possible and more accurate measure for the rutting resistance of asphalt binders, compared to the traditional parameter, G*/sin δ, specified by SHRP. Here, G* is the complex modulus of the binder to indicate its deformation resistance under repeated pulses of shear stress and δ is the time lag between the applied stress and the resulting strain in the binder. Since the G*/sin δ parameter is obtained at a fixed temperature and frequency of testing, it is ineffective in capturing the rutting of asphalt pavements due to the fact that the viscosity of asphalt binder changes with temperature and its elastic properties change with the frequency of loading (Shenoy 2002). However, zero shear viscosity is a measure of the viscosity of a material when a shear stress is acting on it at a shear rate of almost zero. Therefore, the binder experiences deformation so slowly at such low shear rates, that it can adjust continuously to maintain equilibrium. The zero shear viscosity is an indicator for both stiffness of asphalt binder and its resistance to permanent deformation under long term loading (De Visscher et al. 2004).

A rheological test, static creep test at 25 ℃ and 58 ℃, was conducted for unaged PG 58-22, RTFO PG 58-22 and PAV PG 58-22 binders using DSR with a 25 mm diameter plate-plate geometry, and 1 mm gap. PG 58-22 binder was chosen for the validation because it is a non-polymer modified binder which is close to the proposed asphalt model used in this study. In the static creep test, a constant shear stress is applied to the sample and the resultant strain is monitored for a predetermined amount of time. The deformation in the binder reaches to the steady state flow with a constant value when the stress has been applied for a sufficiently long duration of time. The viscosity of the binder at this state is known as zero shear viscosity (Biro et al. 2009). In this study, to guarantee

the deformation of sample asphalt binders that reaches steady state, a constant stress of 100 Pa was applied for 4 h. The zero shear viscosity can be extrapolated from the Burger's model by measuring the creep compliance *J(t)* during the last phase of the test, where the binder deformation is in the steady state (Giuliani et al. 2006). The equation of Burger's model is shown below:

$$\gamma(t) = \frac{\tau_0}{G_0} + \frac{\tau_0}{G_1}\left(1 - e^{\frac{-tG_1}{\eta_1}}\right) + \frac{\tau_0}{\eta_0}t \tag{6.2}$$

where, γ is deformation, t is testing time in second, τ_0 is shear stress value before the strain step (in relaxation), and G_0 and G_1 are shear modulus values of the springs, η_1 is shear viscosity of an individual Maxwell or Kelvin-Voigt element, and η_0 is zero shear viscosity.

When the binder has reached a state flow, the only change portion of the Burger's model is the t/η_0 viscous portion, according to Ciuliani's (2006) study. Therefore, the zero shear viscosity of the tested asphalt binders can be calculated by the following equation:

$$\eta_0 = \frac{\Delta t}{\Delta J} = \frac{900}{J_f - J_{15}} \tag{6.3}$$

where, η_0 is zero shear viscosity, J_{15} is the compliance measured at 15 min before the stress is unloaded, J_f is the compliance measured at the end of the test, and 900 is the time interval in second (15 min) between the two compliance readings.

6.4.2.2 MD Simulation

The MD simulation for viscosity calculation was conducted under NPT ensemble after density simulation as stated previously at 25 ℃ and 58 ℃. The simulation procedures, parameters, and results have been described and discussed previously.

6.4.2.3 Zero Shear Viscosity Validation Results

Figure 6.10(a) and (b) show one example of the zero shear viscosity calculation of the unoxidized asphalt using MD simulation and the results of static creep test for PG 58-22 binders at 25 ℃, respectively. It can be seen that the simulation has reached equilibrium after 800 ps and it is the same for other MD simulations. The zero shear viscosity values of asphalt before and after oxidative aging calculated from MD simulation and experimental results at 25 ℃ and 58 ℃ are shown in Figure 6.11. It can be seen that the zero shear viscosity decreases with an increase in temperature and increases with an increase in the degree of oxidation. The trend of MD simulation results is consistent with experimental results, although the values of zero shear viscosities are in different orders of magnitude due to the different sample sizes (Å vs mm) and calculation methods. The higher viscosity in the higher oxidized asphalt indicates that hardening happens during oxidative aging. The viscosity difference between the two considered temperatures for each type of asphalt is shown in Figure 6.12. It can be seen that the zero shear viscosity decreases more substantially for the oxidized/aged asphalts at higher temperature, for both MD simulation and laboratory testing. The difference increases with an increase in the degree of oxidation. This indicates that the oxidized/aged asphalt is more sensitive to temperature than the unoxidized/unaged asphalt regarding viscosity change.

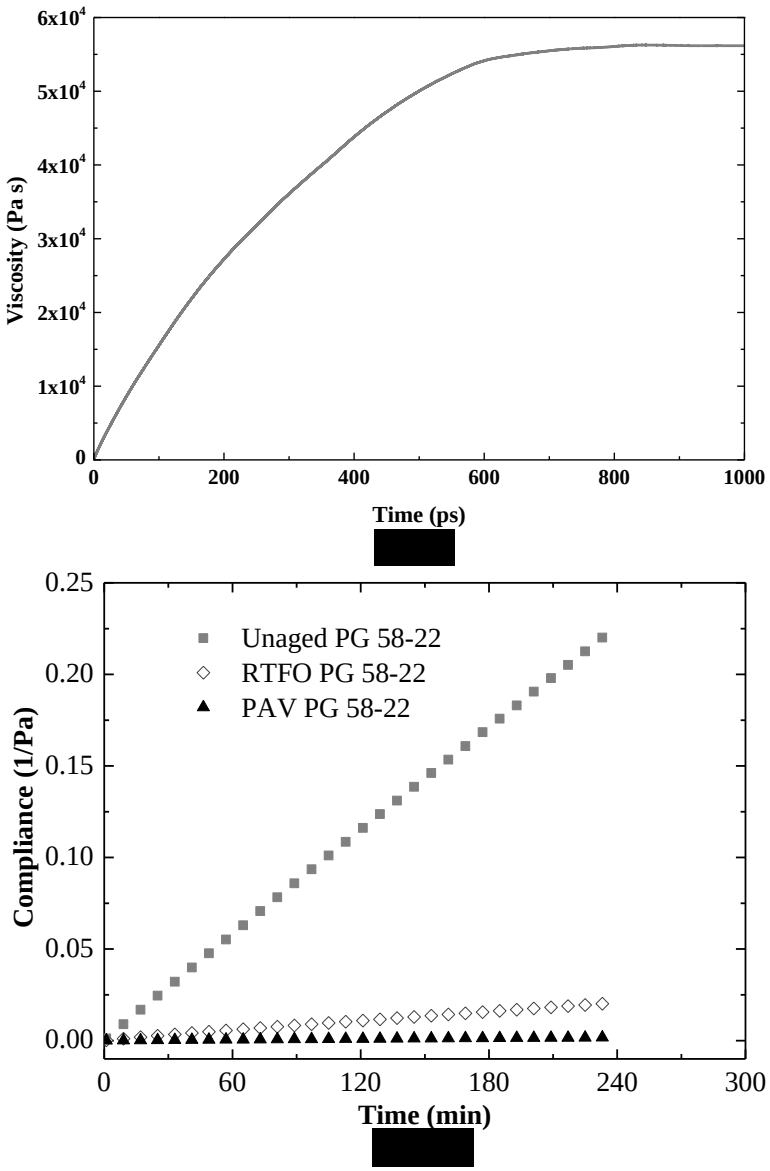

Figure 6.10 Example of zero shear viscosity calculation at 25 ℃ using (a) MD simulation and (b) creep test

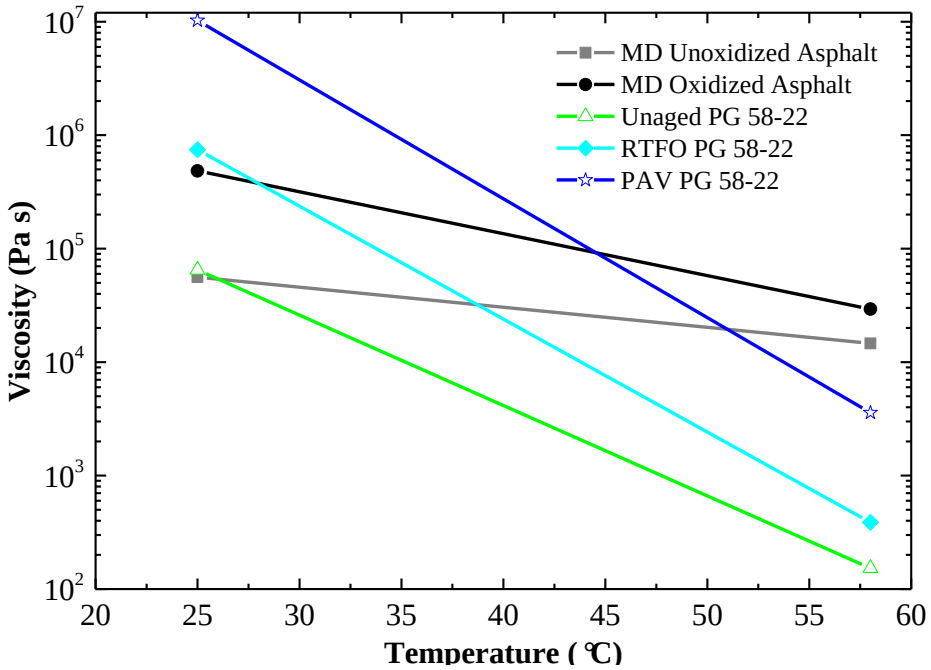

Figure 6.11 Zero shear viscosity of Asphalt before and after oxidative aging under different temperatures

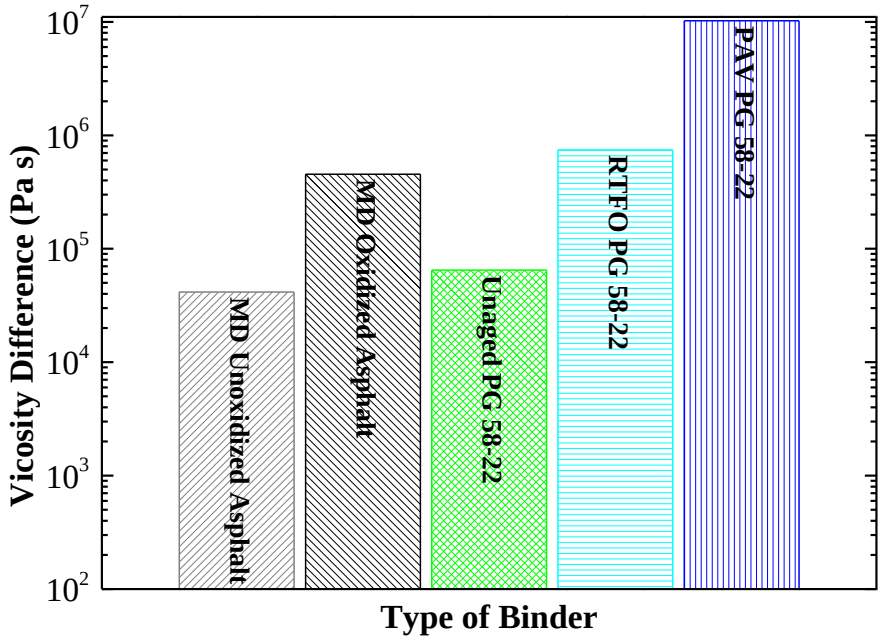

Figure 6.12 Zero shear viscosity difference of asphalt between the values under 25 ℃ and 58 ℃

6.5 Conclusions

Asphalt density is temperature dependent. Generally, density of both unoxidized and oxidized asphalt decreases with an increase in temperature. The density of asphalt increases with an increase in the degree of oxidation. Both the MD simulation and experimental pycnometer test results show that higher oxidized asphalt possesses higher density than the unoxidized asphalt. This indicates that the density of asphalt is sensitive to temperature. Therefore, the temperature factor should be considered when calculating the optimum density of asphalt pavement and testing the density of newly paved asphalt pavement for quality control. The experimental results are consistent with MD simulation results, which validate the reliability of MD simulations.

Isothermal compressibility and bulk modulus are also very sensitive to temperature. Generally, oxidized asphalt has a lower isothermal compressibility and higher bulk modulus than unoxidized asphalt under different temperatures. This proves that hardening happened after asphalt oxidation. The different change trends of isothermal compressibility and bulk modulus between unoxidized and oxidized asphalts under different temperatures indicates glass transition behavior changed after asphalt oxidation.

The calculations of zero shear viscosities from both MD simulations and laboratory tests by DSR tests show that the zero shear viscosity increased with an increase in the degree of oxidation and deceased with an increase in temperature. This further proves that hardening happens in asphalt during oxidation. Moreover, zero shear viscosity decreases more substantially for the oxidized/aged asphalts at higher temperature. The viscosity difference between the two considered temperatures increases with an increase in the

degree of oxidation. This indicates that the oxidized/aged asphalt is more sensitive to temperature than the unoxidized/unaged asphalt regarding viscosity change.

CHAPTER 7

MOISTURE IMPACTS ON ASPHALT BEFORE AND AFTER OXIDATIVE AGING

This chapter is part of a paper entitled "A Study of Moisture Impacts on Asphalt Before and After Oxidation Using Molecular Dynamics Simulations" under review *In Transportation Research Record: Journal of the Transportation Research Board*, which was also accepted for presentation at *Transportation Research Board (TRB) 95th Annual Meeting* with Manuscript Number "16-5680" (Pan et al. 2016b). This chapter is also part of an accepted book chapter, with ID: 131114-042703, entitled "Molecular Dynamics Simulation of Asphaltic Material: Molecular Dynamics Simulations of Oxidative Aging of Asphalt Molecules under Stress and Moisture" in *Handbook of Research on Advanced Computational Techniques for Simulation-Based Engineering*, which will be published on November 30th, 2015 (Tarefder et al. 2015).

Moisture damage is a major damage for asphalt pavement, which is caused by water penetrating into the asphalt-aggregate system and results in rheological property change of the asphalt binder, which shortens the binder's service life and debonds the asphalt from aggregates to accelerate pavement distresses (Chindaprasirt et al. 2009; Ma et al. 2011). Therefore, this chapter is aimed to investigate the impacts of moisture on asphalt before and after oxidative aging using MD simulation.

7.1 Simulation Parameters

For all the MD simulations, system pressure was set at 101.325 kPa (1.0 atm) and system temperature was set at 25 ℃. As stated in Chapter 3, the MD simulation systems were first relaxed using a canonical ensemble, known as NVT ensemble. The simulation time step was set at 0.1 fs with simulation duration of 20 ps (200,000 running steps). An isothermal-isobaric ensemble, also called NPT ensemble, was then used to simulate the realistic asphalt systems and to obtain the densities of asphalt systems. The simulation time step under the NPT ensemble was set at 0.5 fs with simulation duration of 500 ps (1,000,000 running steps) to guarantee the system could reach equilibrium. Water molecules were added into the asphalt simulation boxes before and after oxidation for moisture impact analyses.

First, density simulations for both unoxidized and oxidized asphalt systems with moisture inclusion were conducted by following the same procedure as aforementioned. 1% to 10% moisture contents by the mass of simulation box were considered with a content increment of 2.5%. The range was chosen considering the average moisture content for asphalt binder mix from blending with aggregate to laying the asphalt-aggregate mix down to the road by paver, which is from 0% to 10%, according to Frazier Parker's (Parker 1996) study.

Then, bulk modulus is used to measure a material's resistance to uniform compression. The bulk modulus of asphalt before and after oxidative aging was calculated by Equation (4.1) as discussed in Chapter 4 (Tildesley and Allen 1987). The bulk modulus was calculated for both unoxidized and oxidized asphalt systems at moisture content of 0%

and 5%, respectively, using the data from the last 1,000,000 density simulation steps (500 ps) as aforementioned. All the calculation values were converged after the simulations.

Finally, the MD simulations for zero shear viscosity calculation under 0% and 5% moisture content were conducted under an NPT ensemble after the density simulations, with time step of 0.5 fs and simulation duration of 1 ns (2,000,000). As previously mentioned, zero shear viscosity is a measure of the viscosity of a material when a shear stress is acting on it at a shear rate of almost zero, which is an indicator for both stiffness of asphalt binder and its resistance to permanent deformation under long term loading (De Visscher et al. 2004). The calculation method for zero shear viscosity is shown by Equation (4.2) in Chapter 4.

7.2 Simulation Results and Discussions

7.2.1 Moisture Impact on Density of Asphalt Before and After Oxidative Aging

As previously mentioned in Chapter 3 and Chapter 4, all the density simulations reached equilibrium after 400,000 running steps for density simulation without any moisture inclusion. This is also the same for all other MD simulations with moisture inclusion. The average density value during the last 200,000 running steps was used for further analysis. Figure 7.1 shows the density changes of both unoxidized and oxidized asphalt under different moisture content. It can be seen that the density of oxidized asphalt is constantly higher than the unoxidized asphalt with and without moisture inclusion. The moisture impact on asphalt density within 10% moisture inclusion is not significant, since the density differences for both unoxidized and oxidized asphalts are within 15 kg m-3.

However, the density fluctuations of oxidized asphalt is larger the unoxidized asphalt under different moisture contents. Specifically, for both the unoxidized and oxidized asphalts, density initially increases with an increase in moisture content and starts decreasing at certain moisture content. The maximum density of unoxidized asphalt is at 1% moisture content, while it is at 5% moisture content for the oxidized asphalt. The MD simulation results indicate that water affects more on oxidized asphalt regarding density change.

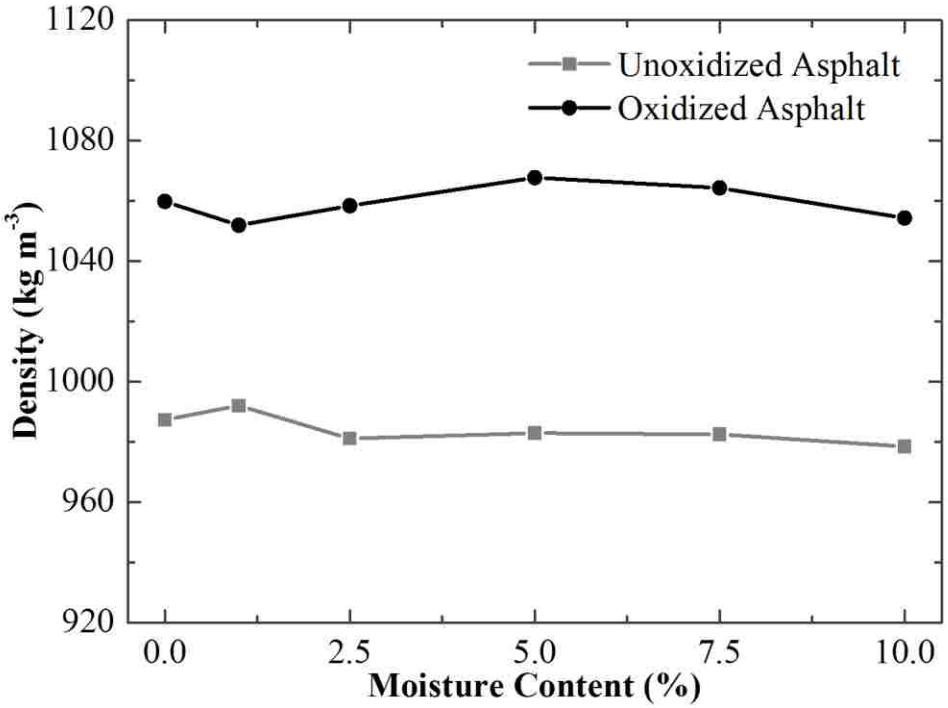

Figure 7.1 Density changes of unoxidized and oxidized asphalts under different moisture contents

7.2.2 Moisture Impact on Bulk Modulus of Asphalt Before and After Oxidative Aging

Figure 7.2 shows the simulation results of bulk modulus calculation for both unoxidized asphalt and oxidized asphalt at 0% and 5% moisture content. It can be seen that all the

simulations reach equilibrium after 450 ps. The average bulk modulus value during the last 50 ps is used for further analysis. Figure 7.3 shows the comparison of bulk modulus values between unoxidized and oxidized asphalts under different moisture contents. It can be seen that bulk modulus of both unoxidized and oxidized asphalt decreases with an increase in moisture content. Without any moisture inclusion, the oxidized asphalt possesses higher bulk modulus than the unoxidized asphalt. However, after 5% moisture inclusion, the bulk modulus of oxidized asphalt is lower than the unoxidized asphalt. This indicates that oxidized asphalt is more sensitive to moisture, which affects oxidized asphalt in a more negative way.

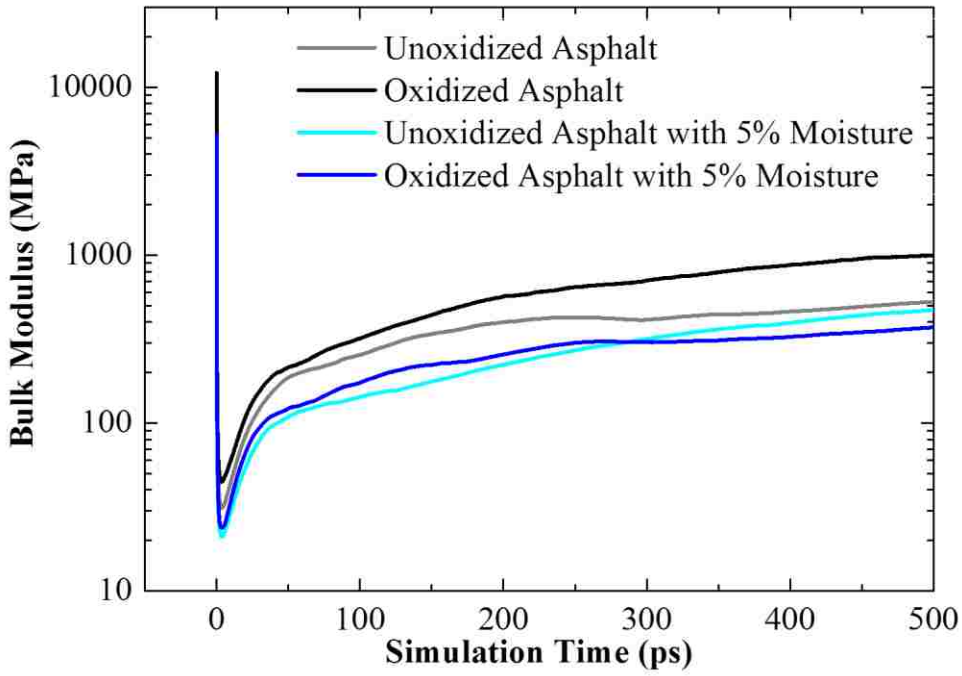

Figure 7.2 Bulk modulus calculation results of asphalt before and after oxidative aging

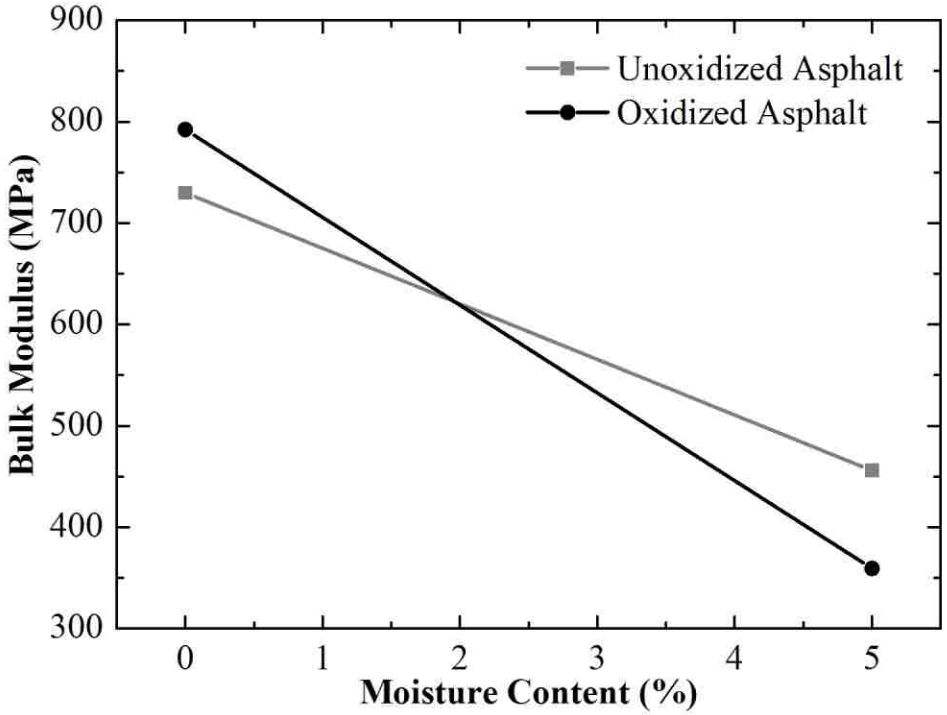

Figure 7.3 Bulk modulus changes of unoxidized and oxidized asphalts under different moisture contents

7.2.3 Moisture Impact on Zero Shear Viscosity of Asphalt Before and After Oxidative Aging

Figure 7.4 shows the simulation results of zero shear viscosities for the asphalt system before and after oxidative aging under different moisture contents. It can be seen that all the simulation reach equilibrium after 850 ps. The average zero shear viscosity value during the last 50 ps is used for further analysis. The zero shear viscosities of both unoxidized and oxidized asphalt under 0% and 5% moisture content are shown in Figure 7.5. It can be seen that the viscosity of oxidized asphalt is much higher than the unoxidized asphalt at 0% moisture content. The increase of viscosity with no moisture inclusion indicates that hardening happened in asphalt during oxidation and asphalt is stiffer after oxidative aging. However, after 5% moisture inclusion, the viscosity of

oxidized asphalt becomes lower than the unoxidized asphalt. Moreover, the viscosities of both unoxidized and oxidized asphalts decrease substantially with an increase in moisture content and the viscosity of oxidized asphalt decreases faster than the unoxidized asphalt. As the same as impact on bulk modulus, moisture affects oxidized asphalt in a more negative way regarding zero shear viscosity change.

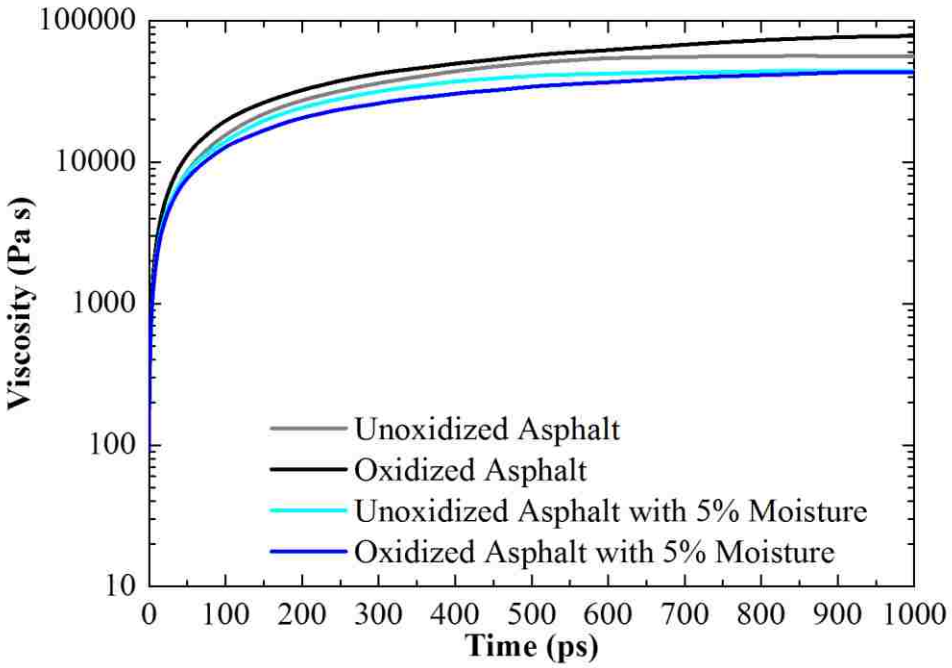

Figure 7.4 Zero shear viscosity calculation results of asphalt before and after oxidative aging

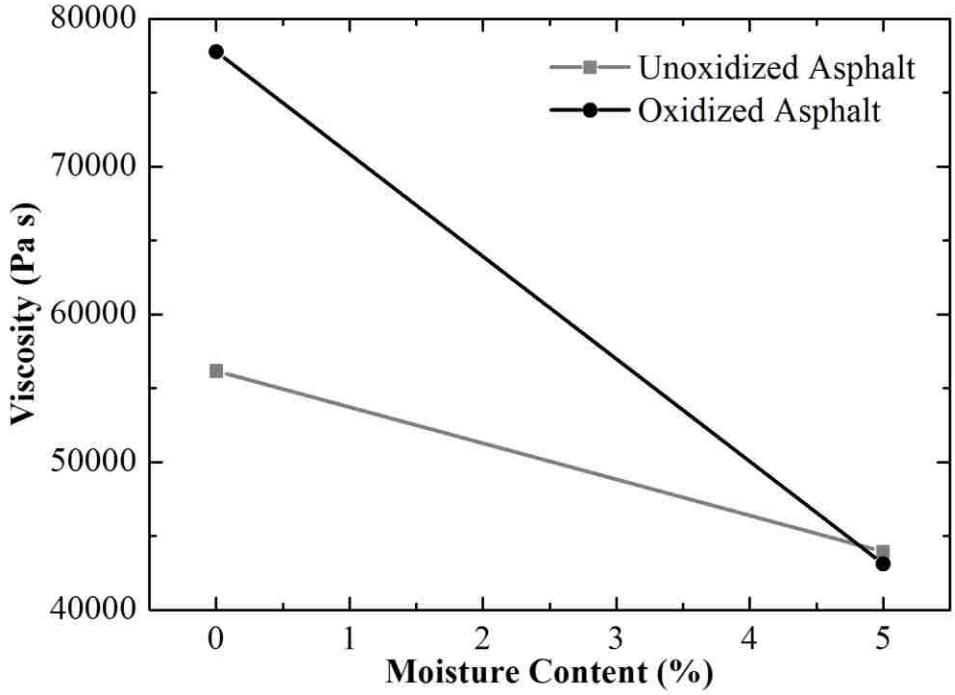

Figure 7.5 Zero shear viscosity changes of unoxidized and oxidized asphalts under different moisture contents

7.3 Laboratory Validation

7.3.1 Moisture Conditioning for Asphalt Binders

In this study, asphalt binders were placed in a humidity controlling chamber for 16 days for moisture conditioning. ASTM E104 (2012), *Standard Practice for Maintaining Constant Relative Humidity by Means of Aqueous Solutions*, was followed using an aqueous solution of salt to create a constant relative humidity (RH) in an enclosed chamber under constatnt temperature. The relative humidity is defined as the ratio of the partial pressure of water vapor to the equilibrium vapor pressure of water at the same temperature. Sodium Chloride (NaCl) was chosen to create the aqueous solutions due to its chemical stability, which was mixed with distilled water in desiccator at room temperature approximately 22 ℃. Figure 7.6 shows the desiccator with asphalt binder

samples for moisture conditioning. The aqueous solution used is in supersaturation condtion that is necessary for thermodynamics equilibrium condition at the room temperature. RH of the Sodium Chloride solution varies from 73.9% to 75.7% at the temperature range of 5 ℃ to 80 ℃. In this study, the RH value of Sodium Chloride solution was constant at 22 ℃ after 5 days, which was 71%.

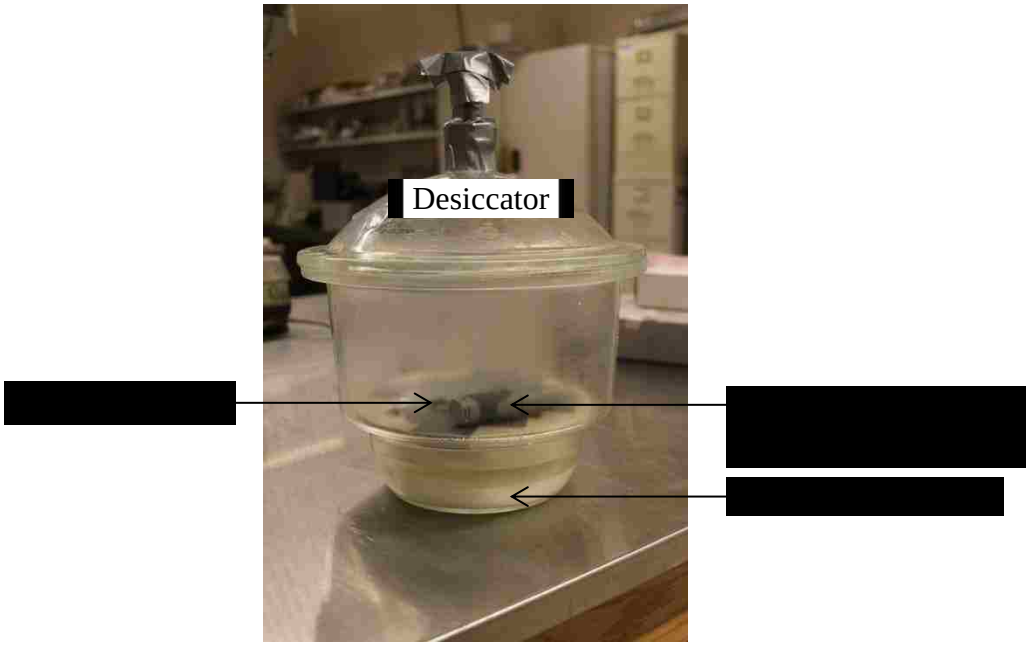

Figure 7.6 Laboratory setup for moisture conditioning

7.3.2 Dynamic Shear Rheometer (DSR) Testing for Zero Shear Viscosity of Asphalt Before and After Moisture Inclusion

In this study, PG 58-22 asphalt binder was used for zero shear viscosity testing using DSR at 25 ℃. Asphalt sample was conditioned in the desiccator for 16 days under moisture. The weight of sample before and after moisture conditioning was measured and moisture content was calculated. The moisture content in asphalt binder was 5%. The

DSR test procedures and calculation method for zero shear viscosity of asphalt binder are the same as previously mentioned.

Figure 7.7 shows the results of static creep tests for PG 58-22 binder before and after 5% of moisture inclusion at 25 ℃ using DSR. Figure 7.8 shows the zero shear viscosity value vs. moisture content calculated from MD simulations and laboratory tests. It can be seen that the simulation result is consistent with laboratory testing results. The zero shear viscosity of asphalt binder decreases with an increase in moisture content. Moisture adversely affects the viscosity of asphalt binder.

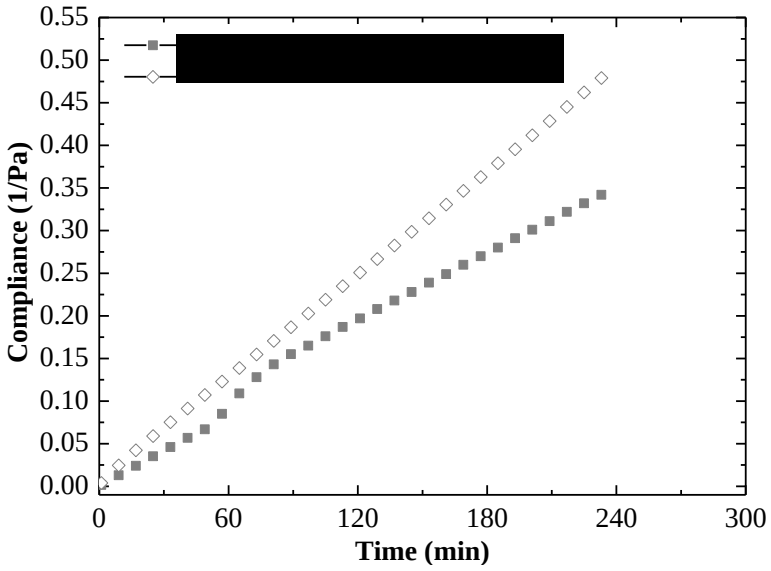

Figure 7.7 Creep test results from DSR

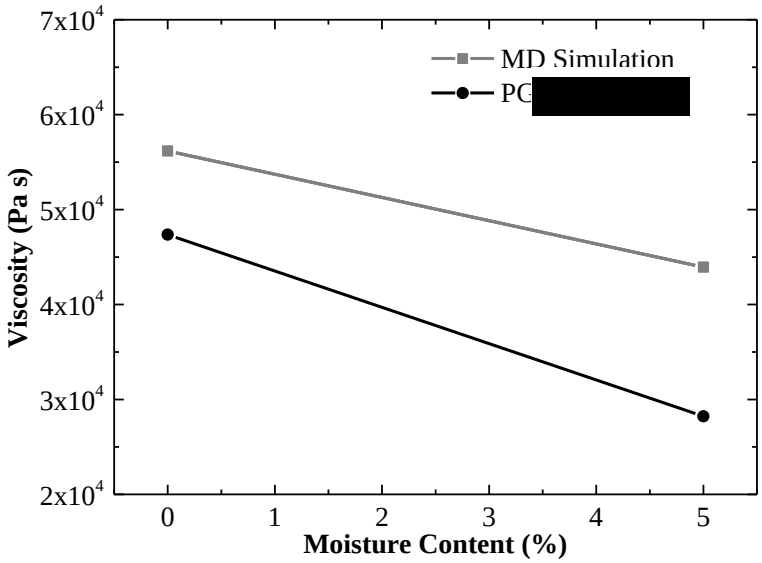

Figure 7.8 Zero shear viscosity vs. moisture content from MD simulations and experiments

7.3.3 Nanoindentation Testing for the Nanomechanical Evaluation of Asphalt Before and After Moisture Inclusion

7.3.3.1 Nanoindentation

In a nanoindentation test, an indenter tip of a known modulus of elasticity and geometry is loaded to penetrate a sample surface and then unloaded. Modulus, such as elastic modulus *E*, of the sample is determined from the load-displacement data and the area of contact at full load is determined from the measured depth of penetration and the known geometry of the indenter tip. The sample hardness is then calculated via dividing the maximum load by the contact area.

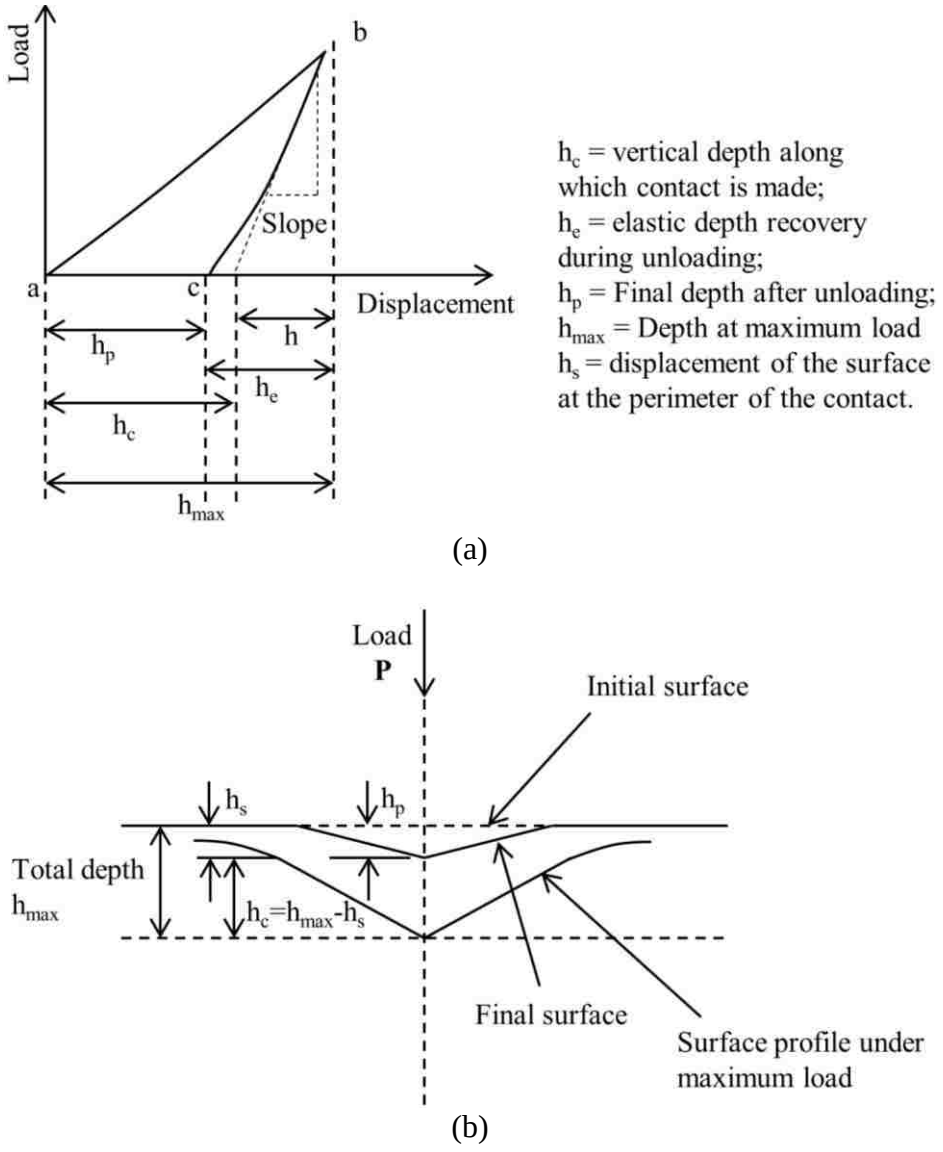

Figure 7.9 Schematic of nanoindentation test: (a) load vs. displacement curve and (b) surface profile during nanoindentation

Figure 7.9(a) and (b) shows the schematic of nanoindentation test. During the test, a sitting load is typically applied initially to facilitate a contact between the tip and the sample surface. As shown in Figure 7.9(a), the load increases gradually from point *a* to *b* and the tip is unloaded at the maximum load point *b*. The unloading curve from point *b* does not return back to *a* due to plastic deformation of an elastoplastic material. The

slope of the unloading curve at point *b* is usually equal to the slope of the loading curve at point *a* (Tarefder and Faisal 2013b). The surface profile during nanoindentation is shown in Figure 7.9(b), which is a function of the penetration depth during loading and unloading. The vertical depth between the indenter and the sample is calculated by:

$$h_c = h_{\max} - h_s \tag{7.1}$$

where, h_c is the vertical depth along which the contact is made between the indenter and the sample, h_{max} is the total depth of nanoindentation at a maximum load, h_s is the depth of the surface at the perimeter of the indenter contact.

The depth of impression recovered is calculated by:

$$h_e = h_{\max} - h_p \tag{7.2}$$

where, h_e is the depth of impression recovered, h_{max} is the total depth of nanoindentation at a maximum load, h_P is the total depth of indentation that is unrecovered.

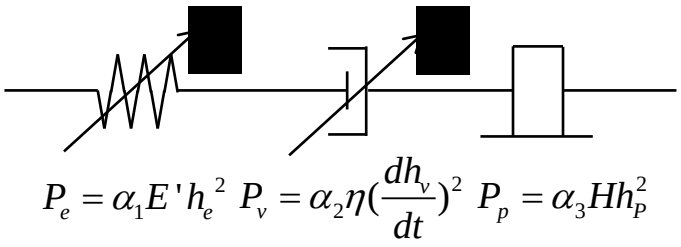

Figure 7.10 Spring-Dashpot-Rigid (SDR) element model

Since asphalt is a visco-elastoplastic material, a Spring-Dashpot-Rigid (SDR) model was used for the calculation of asphalt's modulus, hardness and viscosity. The model was used by Tarefder and Faisal (2013b) for asphalt materials and they proved that it is in a good agreement with nanoindentation data. Figure 7.10 shows the SDR model (Olesiak et al. 2010; Oyen and Cook 2003). Load-displacement relation of spring is defined as:

$$P_e = k_Q h_e^2 \tag{7.3}$$

where, P_e is the load on the spring, h_e is the displacement in the spring, k_Q is the quadratic stiffness, which is identified with the plain strain modulus of the material, E' [$E' = E/(1-\nu^2)$, here ν is Poisson's ratio], via geometric considerations: $k_Q = \alpha_1 E'$, and $\alpha_1 = \pi/(2\cot\psi)$.

The dashpot is defined as:

$$P_v = \mu_Q \left(\frac{dh_v}{dt}\right)^2 \tag{7.4}$$

where, P_v is the load on the dashpot, h_v is the displacement in the dashpot, μ_Q is the quadratic viscous coefficient. The coefficient is the product of geometric term α_2 and a material property: $\mu_Q = \alpha_2 \eta$. Here, η is the apparent viscosity of the material and $\alpha_1 = \alpha_2$.

The third element is defined by a rigid body that can bear substantial plastic deformation beneath the indenter. The express is:

$$P_p = \alpha_3 H h_P^2 \tag{7.5}$$

where, P_p and h_p are the load and displacement on the rigid body element, respectively, H is the plastic deformation resistance or hardness of the materials, and $\alpha_3 = \pi \, tan^2\psi$, which is a dimensionless geometry parameter for sharp indentation with effective included angle 2ψ.

Therefore, the total displacement is the sum of all the three elements' displacements as shown below:

$$h = h_e + h_v + h_p \tag{7.6}$$

Load in the elements can be written as:

$$P = P_e = P_v = P_p \tag{7.7}$$

The form of SDR model is described below:

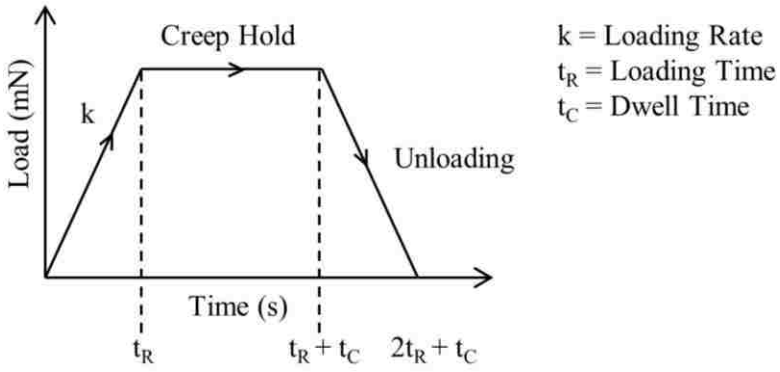

Figure 7.11 Schematic of a trapezoidal indentation load

First, a trapezoidal indentation load is considered with constant loading and unloading rate k, as shown in Figure 7.11. It can be seen that the creep hold or dwell time t_c is

applied at the maximum load and t_R represents loading and unloading time. The slope of the loading curve can be expressed as:

$$P(t) = kt \tag{7.8}$$

$$\frac{dP}{dt} = \frac{dP_e}{dt} = \frac{dP_v}{dt} = \frac{dP_p}{dt} = k; \quad 0 \le t \le t_R \tag{7.9}$$

Substituting the slope value in Equation (7.9) gives:

$$\frac{dh}{dt} = \frac{(kt)^{1/2}}{(\alpha_2 \eta)^{1/2}} + \frac{1}{(kt)^{1/2}} \frac{k}{2(\alpha_1 E')^{1/2}} + \frac{1}{(kt)^{1/2}} \frac{k}{2(\alpha_3 H)^{1/2}} \tag{7.10}$$

Integrating Equation (7.10) gives:

$$h^{LOAD}(t) = (kt)^{1/2} \left(\frac{2t}{3(\alpha_2 \eta)^{1/2}} + \frac{1}{(\alpha_1 E')^{1/2}} + \frac{1}{(\alpha_3 H)^{1/2}} \right) \tag{7.11}$$

Second, creep curve is used to calculate the slope during holding time, which can be expressed as:

$$\frac{dP}{dt} = 0; \quad t_R \le t \le t_c + t_R \tag{7.12}$$

Substituting the slope value in Equation (7.12) and then integrating the resulting equation gives:

$$h^{CREEP}(t) = \int_{t_R}^{t_C + t_R} \frac{(P_{\max})^{1/2}}{(\alpha_2 \eta)^{1/2}} dt \tag{7.13}$$

$$h^{CREEP}(t) = \frac{(P_{\max})^{1/2}}{(\alpha_2 \eta)^{1/2}}(t - t_R) + h^{LOAD}(t_R) \tag{7.14}$$

where, P_{max} is the peak load.

Finally, unloading curve is used to calculate the slope during unloading time, which can be expressed as:

$$\frac{dP}{dt} = -k; \quad t_R + t_C \le t \le 2t_R + t_C \tag{7.15}$$

The assumptions of perfect plasticity that forces the plastic element to be suppressed on unloading is $dh_p/dt = 0$. Thus the unloading constitutive equation is:

$$\frac{dh}{dt} = \frac{[k(2t_R + t_C - t)]^{1/2}}{(\alpha_2 \eta)^{1/2}} - \frac{1}{[k(2t_R + t_C - t)]^{1/2}} \frac{k}{2(\alpha_1 E')^{1/2}} + 0 \tag{7.16}$$

Integrating Equation (7.16) gives:

$$h^{UNLOAD}(t) = (k)^{1/2}\left(\frac{t_R^{3/2} - (2t_R + t_C - t)^{3/2}}{\frac{3}{2(\alpha_2 \eta)^{1/2}}} + \frac{(2t_R + t_C - t)^{1/2} - t_R^{1/2}}{(\alpha_1 E')^{1/2}}\right) + h^{CREEP}(t_R + t_C) \tag{7.17}$$

Equations (7.11), (7.14) and (7.17) define the entire displacement-time history of a nanoindentation test of asphalt binder using trapezoidal loading.

7.3.3.2 Nanoindentation Procedures and Parameter Determination

PG 58-22 binder before and after moisture inclusion was used for the nanoindentation test in this study at 25 ℃. Figure 7.12 shows a laboratory prepared asphalt binder film on

glass substrate with 12.7 mm × 12.7 mm (0.5 in ×0.5 in) surface area selected, which is encompassed by high temperature resistant tape. Berkovich tips were used for asphalt testing due to its non-adherence to asphalt binder (Tarefder and Faisal 2013a; b; c). Three binder samples were used for the nanoindentation tests.

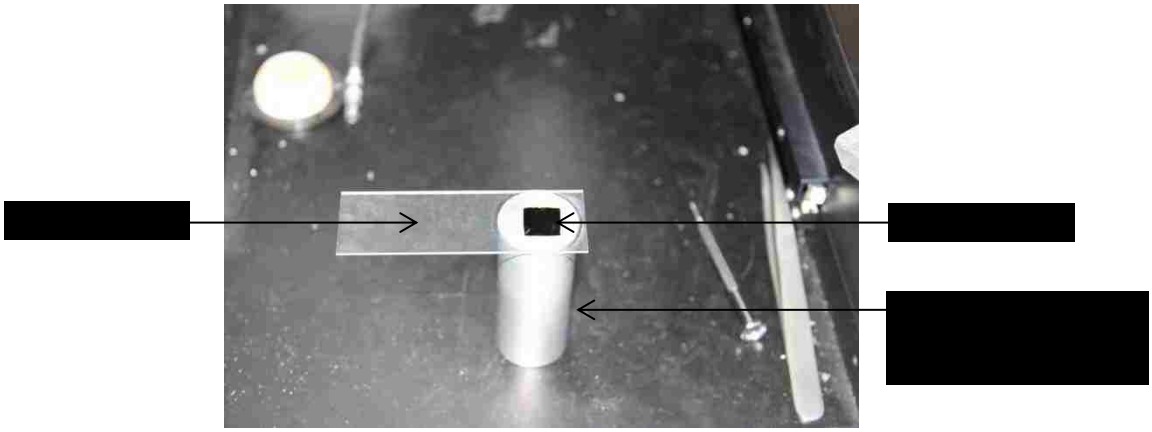

Figure 7.12 Binder sample prepared for nanoindentation

A sitting load of 0.01 mN was initially applied for each indentation, which was applied to satisfy proper contact between the binder and the nanoindenter. A maximum load of 0.05 mN was applied with the same loading and unloading rate of 0.002 mN/sec. A creep or dwell time of 200 sec was applied after the maximum load. The loading and unloading rate and dwell time selected were for minimizing the viscous effect of asphalt binder and the pile up effect of asphalt binder around the indenter tip (Faisal et al. 2015).

The nanoindentation testing data is used to fit the above Equations (7.11), (7.14) and (7.17). The indentation viscosity η was obtained by fitting the displacement data into Equation (7.14) and then the plain strain modulus E' were obtained by fitting the unloading data into Equation (7.17) and Equation (7.11) was used to acquire the hardness *H*. The curve fitting of the displacement-time history was done in MATLAB using

nonlinear least square fitting. Average value of each the parameter from the three asphalt samples were used to represent the plain strain modulus, hardness and indentation viscosity of asphalt.

7.3.3.3 Results and Discussions

Figure 7.13 shows one example of the comparison between laboratory result and fitting result of SDR model of asphalt binder after moisture conditioning at 71% RH. It can be seen that the SDR model successfully captured the viscoelastic response of the asphalt material.

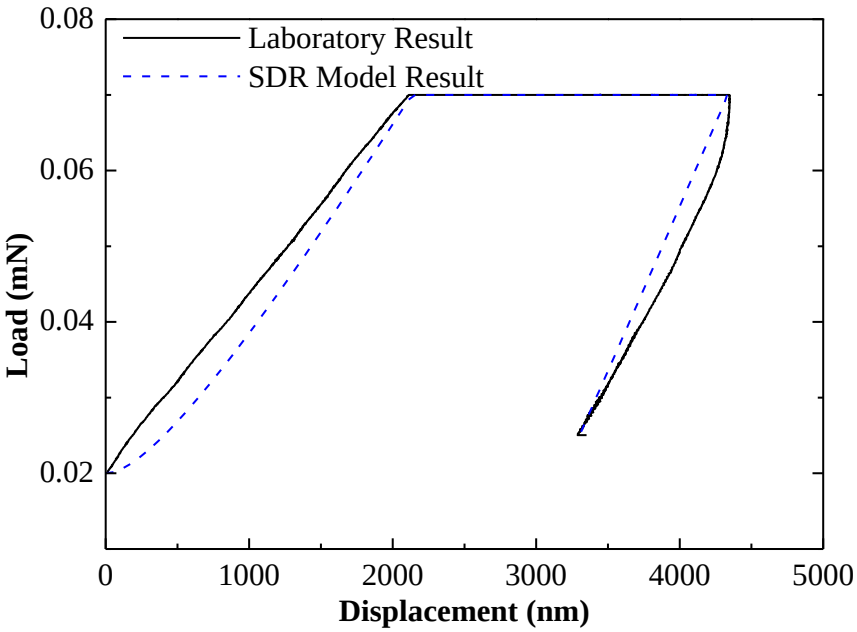

Figure 7.13 Laboratory result and fitting result of SDR model of asphalt binder after moisture conditioning at 71% RH

Figure 7.14 shows the results of plain strain modulus, hardness and indentation viscosity of asphalt binder before and after moisture conditioning at 71% RH. It can be seen that all the parameters shows a decreasing trend after moisture inclusion. The results are

consistent with DSR test results and MD simulation results for asphalt binder after moisture inclusion which show that the bulk modulus and zero shear viscosity of asphalt decrease with an increase in the moisture content in the asphalt. This indicates that moisture negatively affects the properties of asphalt by decreasing the strength of asphalt.

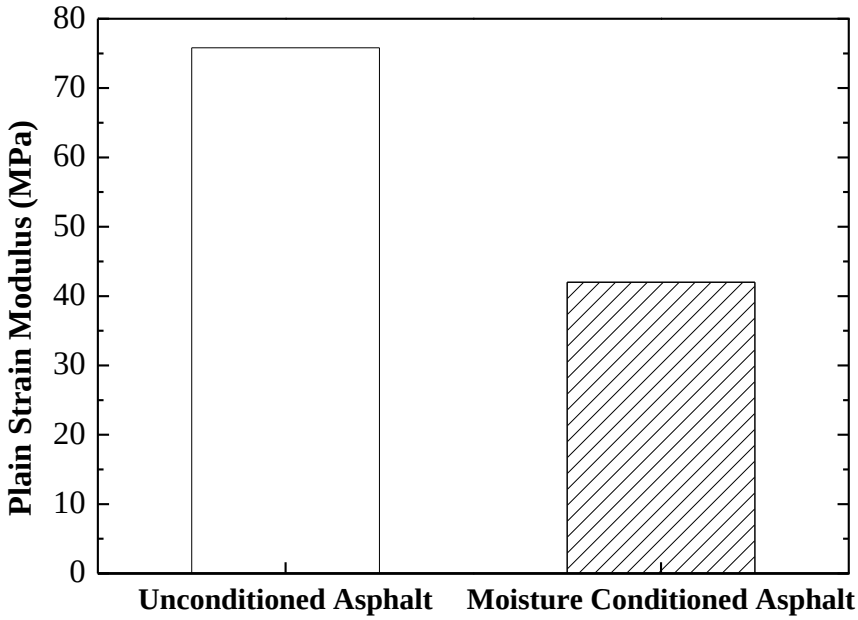

(a)

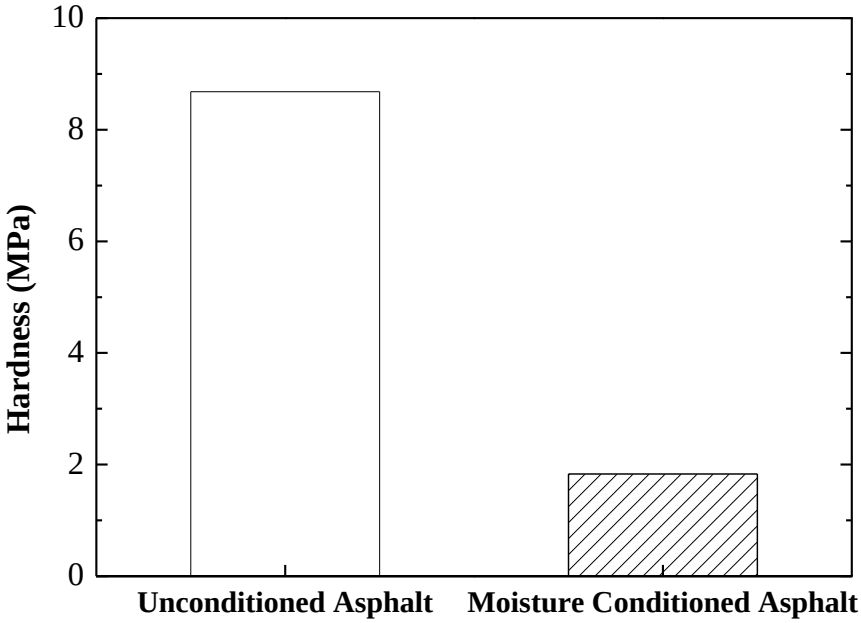

(b)

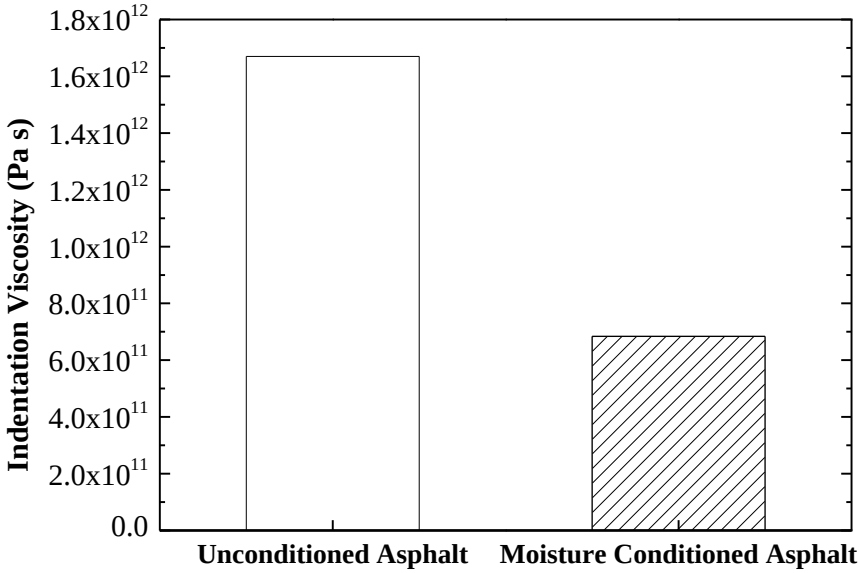

(c)

Figure 7.14 Comparison of plain strain modulus (a), hardness (b), and indentation viscosity (c) of asphalt before and after moisture conditioning

7.3 Conclusions

Conclusions are as follows:

- The moisture impact on the density of asphalt before and after oxidation is not significant. Density of oxidized asphalt is constantly higher than the unoxidized asphalt under different moisture contents and the density fluctuations of oxidized asphalt is larger the unoxidized asphalt. This indicates that asphalt is more sensitive to moisture inclusion after oxidative aging regarding density change.

- The bulk modulus of oxidized asphalt is higher than the unoxidized asphalt before any moisture inclusion. This proves that the hardening happened in asphalt during oxidation. However, the bulk modulus of oxidized asphalt decreases faster than the unoxidized asphalt after moisture inclusion, which is lower than the unoxidized asphalt

after 5% moisture added into the simulation systems. This indicates that moisture adversely impacts more on oxidized asphalt regarding bulk modulus change.

- As the same impact on bulk modulus of asphalt before and after oxidative aging, moisture affects the zero shear viscosity of oxidized asphalt in a more negative way. The zero shear viscosity of oxidized asphalt is much higher than the unoxidized asphalt before any moisture inclusion due to the increase of hardness and stiffness in asphalt after oxidative aging. However, after 5% moisture inclusion, the zero shear viscosity of oxidized asphalt becomes lower than the unoxidized asphalt. This partially explains the moisture damage mechanism on asphalt-aggregate mixtures that the moisture debonds asphalt from aggregate by lowering the viscosity of asphalt.

- The moisture negatively affects the properties of asphalt regarding modulus, hardness and viscosity from the results of both MD simulations and laboratory tests. MD simulations and DSR tests show that the bulk modulus and zero shear viscosity of asphalt decrease with an increase in moisture content in asphalt. Nanoindentation results from SDR model further prove that moisture inclusion in asphalt decreased the modulus, hardness and viscosity of asphalt. This indicates that moisture negatively affects the properties of asphalt by decreasing the strength of asphalt.

CHAPTER 8

CONCLUSIONS AND RECOMMENDATIONS

8.1 General

In this dissertation, the oxidative aging behavior of asphalt is studied using MD simulation in the perspective of molecular scale. The oxidation mechanism of asphalt is discussed and asphalt models before and after oxidative aging are developed for MD simulation. The relationships between internal property changes in asphalt (energy change, property change in molecular scale) and external property changes (physical, thermodynamic, mechanical and rheological property change) of the asphalt due to oxidation are investigated. The experimental testing is also conducted to validate the MD simulations. Results verify the reliability of MD simulations.

MD simulations are used in this study to understand the fundamental material science of asphalt and the understandings and findings of this study can be used to help improve/modify molecular composition of asphalt to resist oxidation and moisture damage in the future. Moreover, the developed asphalt models can be used for predict performance of asphalt at microscopic level in the future.

8.2 Conclusions

8.2.1 Relationships Between Internal Intermolecular Interactions and External Properties of Asphalt Due to Oxidative Aging

Oxidized functional groups in asphalt molecules increase the strength of intermolecular bonds of asphalt, which causes agglomeration of the system and further contributes to the hardening of the oxidized asphalt. The internal property change is consistent with the external physical and rheological property change after oxidation, which is revealed by the increase of density, bulk modulus and viscosity. Specifically, it can be concluded that the internal energy changes, especially for higher magnitude of intermolecular and lower kinetic energies, are responsible for the hardening of oxidized asphalt, and the higher potential energies and for oxidized asphalt further proves that oxidation increases the polarity of molecules in asphalt and forms strongly interacting components.

8.2.2 Mechanical Properties of Asphalt Before And After Oxidative Aging

For both unoxidized and oxidized asphalts under different compressive and tensile stress rates, the deformation increases faster with the increase of stress rates. The hardening of oxidized asphalt is also revealed by its mechanical property change. Overall, the oxidized asphalt deforms slower and less than the unoxidized asphalt under both compressive and tensile stresses.

The comparison between different compressive and tensile stress rates applied on both unoxidized and oxidized asphalts shows that asphalts under different tensile stress rates fail faster than under the same magnitudes of compressive stress rates.

The trend of the simulation results of asphalt systems under compression is consistent with the trend of laboratory test results obtained by the study of Tarefder and Faisal (2013a) about the nanoindentation behavior of long-term aged asphalt under different compressive loading rates.

8.2.3 Asphalt Property Changes Before and After Oxidative Aging under Different Temperatures

Asphalt density is temperature dependent. Generally, density of both oxidized asphalt and unoxidized asphalt decreases with an increase in temperature. Oxidized asphalt has higher density than unoxidized asphalt but decreases slightly slower than unoxidized asphalt. This might be caused by the hardening of asphalt after oxidation.

Isothermal compressibility and bulk modulus are also very sensitive to temperature. Generally, oxidized asphalt has a lower isothermal compressibility and higher bulk modulus than unoxidized asphalt under different temperatures. This proves that hardening happened after asphalt oxidation. The different change trends of isothermal compressibility and bulk modulus between unoxidized and oxidized asphalts under different temperatures indicate glass transition behavior changed after asphalt oxidation.

The calculations of zero shear viscosities from MD simulations show that the zero shear viscosity increases with an increase in the degree of oxidation and deceases with an increase in temperature. This further proves that hardening happens in asphalt during oxidation. Moreover, zero shear viscosity decreases more substantially for the oxidized

asphalts at higher temperature. This indicates that the oxidized asphalt is more sensitive to temperature than the unoxidized asphalt regarding viscosity change.

Laboratory pycnometer testing results for unaged, RTFO aged and PAV aged asphalts are consistent with the MD simulation results that the density of asphalt increases with an increase in the degree of oxidation and temperature adversely affects the densities of both unaged and aged asphalts, which decrease with an increase in temperature. The calculations of zero shear viscosities from laboratory tests by DSR tests are also in good agreement with the MD simulation results. The viscosity difference between the two considered temperatures (25 ℃ and 58 ℃) increases with an increase in the degree of oxidation in asphalt.

8.2.4 Moisture Impacts on Asphalt Before and After Oxidative Aging

The moisture impact on the density of asphalt before and after oxidation is not significant. Density of oxidized asphalt is constantly higher than the unoxidized asphalt under different moisture contents and the density fluctuations of oxidized asphalt is larger the unoxidized asphalt. This indicates that asphalt is more sensitive to moisture inclusion after oxidative aging regarding density change.

The bulk modulus of oxidized asphalt is higher than the unoxidized asphalt before any moisture inclusion. This proves that the hardening happened in asphalt during oxidation. However, the bulk modulus of oxidized asphalt decreases faster than the unoxidized asphalt after moisture inclusion, which is lower than the unoxidized asphalt after 5%

moisture added into the simulation systems. This indicates that moisture adversely impacts more on oxidized asphalt regarding bulk modulus change.

As the same impact on bulk modulus of asphalt before and after oxidative aging, moisture affects the zero shear viscosity of oxidized asphalt in a more negative way. The zero shear viscosity of oxidized asphalt is much higher than the unoxidized asphalt before any moisture inclusion due to the increase of hardness and stiffness in asphalt after oxidative aging. However, after 5% moisture inclusion, the zero shear viscosity of oxidized asphalt becomes lower than the unoxidized asphalt. This partially explains the moisture damage mechanism on asphalt-aggregate mixtures that the moisture debonds asphalt from aggregate by lowering the viscosity of asphalt.

Generally, the moisture negatively affects the properties of asphalt regarding modulus, hardness and viscosity from the results of both MD simulations and laboratory tests. MD simulations and DSR tests show that the bulk modulus and zero shear viscosity of asphalt decrease with an increase in moisture content in asphalt. Nanoindentation results from SDR model further prove that moisture inclusion in asphalt decreases the modulus, hardness and viscosity of asphalt. This indicates that moisture negatively affects the properties of asphalt by decreasing the strength of asphalt.

8.3 Recommendations for Further Study

Asphalt behavior before and after oxidative aging is investigated in this study. MD simulations are used to understand how the molecular performance in asphalt before and

after oxidative aging affects the physical, thermodynamic, mechanical and rheological properties of asphalt. Some recommendations for further study are made as follows:

- The asphalt models before and after oxidative aging are developed according to literature review. For further study, more chemical tests need to be done to study the components and molecular structures in asphalt before and after oxidation and aging to improve the models.

- According to this study, asphalt's density is significantly sensitive to temperature. The temperature factor should be considered when calculating the optimum density of asphalt pavement and testing the density of newly paved asphalt pavement for quality control. For further study, more MD simulations and laboratory tests can be done to understand the precise relationship between density of asphalt and temperature by developing a density-temperature model for asphalt.

- According to this study, oxidized asphalt is more susceptible to moisture damage. This indicates that reclaimed asphalt pavement (RAP) should not be widely used in asphalt pavement in humid area due to stronger moisture impacts on aged binders. For further study, more laboratory tests can be done to study the differences of moisture impacts on asphalt binders with different degree of oxidative aging.

- Only the oxidative aging behavior of asphalt binder is studied in this dissertation. The adhesion strength of asphalt on aggregate before and after oxidative aging is not investigated. Moreover, what is the moisture effect on the bonding strength between asphalt and aggregate before and after oxidative aging is still uncertain. For further study,

asphalt-aggregate interface models before and after oxidative aging can be developed to study these issues using MD simulations.

REFERENCES

Andersen, H. C. (1980). "Molecular Dynamics Simulations at Constant Pressure and/or Temperature." *The Journal of Chemical Physics*, 72(4), 2384–2393.

Artok, L., Su, Y., Hirose, Y., Hosokawa, M., Murata, S., and Nomura, M. (1999). "Structure and Reactivity of Petroleum-Derived Asphaltene." *Energy & Fuels*, American Chemical Society, 13(2), 287–296.

ASTM International. (2009a). *ASTM D4124 - 09 Standard Test Method for Separation of Asphalt into Four Fractions*. West Conshohocken.

ASTM International. (2009b). *ASTM D70, Standard Test Method for Density of Semi-Solid Bituminous Materials (Pycnometer Method)*. West Conshohocken.

ASTM International. (2012). *ASTM E104-02 Standard Practice for Maintaining Constant Relative Humidity by Means of Aqueous Solutions*. West Conshohocken.

Bardon, C., Barre, L., Espinat, D., Guille, V., Li, M. H., Lambard, J., Ravey, J. C., Rosenberg, E., and Zemb, T. (1996). "The Colloidal Structure of Crude Oils and Suspensions of Asphaltenes and Resins." *Fuel Science and Technology International*, Taylor & Francis, 14(1-2), 203–242.

Berendsen, H. J. C., Postma, J. P. M., van Gunsteren, W. F., DiNola, A., and Haak, J. R. (1984). "Molecular Dynamics with Coupling to an External Bath." *Journal of Chemical Physics*, 81, 3684–3690.

Besson, J., Cailletaud, G., Chaboche, J.-L., and Forest, S. (2010). *Non-Linear Mechanics of Materials*. Springer Netherlands, Dordrecht.

Biro, S., Gandhi, T., and Amirkhanian, S. (2009). "Determination of Zero Shear Viscosity of Warm Asphalt Binders." *Construction and Building Materials*, Elsevier Ltd, 23(5), 2080–2086.

Bodan, A. N. (1982). "Polyquasispherical Structure of Petroleum Asphalts." *Chemistry and Technology of Fuels and Oils*, Kluwer Academic Publishers-Plenum Publishers, 18(12), 614–618.

Branthaver, J. F., Petersen, J. C., Robertson, R. E., Duvall, J. J., Kim, S. S., Harnsberger, P. M., Mill, T., Ensley, E. K., Barbour, F. A., and Schabron, J. F. (1993). *Binder Characterization and Evaluation, Volume 2: Chemistry*. SHRP Report A-368. Washington, DC: Strategic Highway Research Program, National Research Council.

Brown, T. L., LeMay, H. E., Bursten, B. E., Murphy, C., and Woodward, P. (2011). *Chemistry: The Central Science*. Prentice Hall.

Callister, W. D., and Rethwisch, D. G. (2012). *Fundamentals of Materials Science and Engineering: an Integrated Approach*. John Wiley & Sons, Hoboken, NJ.

Chindaprasirt, P., Hatanaka, S., Mishima, N., Yuasa, Y., and Chareerat, T. (2009). "Effects of Binder Strength and Aggregate Size on the Compressive Strength and Void Ratio of Porous Concrete." *International Journal of Minerals, Metallurgy and Materials*, 16(6), 714–719.

Ciccotti, G., and Ryckaert, J. P. (1986). "Molecular Dynamics Simulation of Rigid Molecules." *Computer Physics Reports*, 4(6), 346–392.

Claudy, P., Letoffe, J. M., King, G. N., and Plancke, J. P. (1992). "Characterization of Asphalts Cements by Thermomicroscopy and Differential Scanning Calorimetry: Correlation to Classic Physical Properties." *Fuel Science and Technology International*, Taylor & Francis, 10(4-6), 735–765.

Corbett, L. W. (1965). "Manufacture of Petroleum Asphalt." *Bituminous Materials: Asphalts, Tars and Pitches*, A. J. Hoiberg, ed., Interscience Publishers, New York, 81–122.

Corbett, L. W. (1969). "Composition of Asphalt Based on Generic Fractionation , Using Solvent Deasphaltening, Elution-Adsorption Chromatography, and Densimetric Characterization." *Analytical Chemistry*, 41(4), 576–579.

Dwiggins, C. W. (1965). "A Small Angle X-Ray Scattering Study of the Colloidal Nature of Petroleum." *The Journal of Physical Chemistry*, American Chemical Society, 69(10), 3500–3506.

E, W. (2011). *Principles of Multiscale Modeling*. Cambridge University Press, New York, NY.

Espinat, D., Rosenberg, E., Scarsella, M., Barre, L., Fenistein, D., and Broseta, D. (1998). "Colloidal Structural Evolution from Stable to Flocculated State of Asphaltene Solutions and Heavy Crudes." *Structures and Dynamics of Asphaltenes SE - 5*, O. Mullins and E. Sheu, eds., Springer US, 145–201.

European Committee for Standardization. (2000). *EN 12597: Bitumen and Bituminous Binders – Terminology*.

Faisal, H. M., Hossain, M. I., and Tarefder, R. A. (2015). "Nanomechanical Evaluation of Vapor-Conditioned and Unconditioned Asphalt." *Transportation Research Board 94th Annual Meeting*, Washington, DC, Jan. 11th-15th.

Fraaije, J. (Hans) G. E., Nath, S. K., Male, J. van, Becherer, P., Wolterink, J. K., Handgraaf, J.-W., Case, F., Tanase, C., and Gracia, R. S. (2014). "Culgi Manual 8.0." Culgi, The Netherlands.

Fried, J. R. (2007). "Chapter 4 Computational Parameters." *Physical Properties of Polymers Handbook*, J. E. Mark, ed., Springer, New York, NY, 59–65.

Gilman, J. J. (2009). *Chemistry and Physics of Mechanical Hardness*. John Wiley & Sons, Inc., Hoboken, NJ.

Giuliani, F., Merusi, F., and Antunes, I. (2006). "Creep Flow Behavior of Asphalt Rubber Binder–the Zero Shear Viscosity Analysis." *Proceedings of the Asphalt Rubber*.

Gordon, P. (2003). “Influence of Simulation Details on Thermodynamic and Transport Properties in Molecular Dynamics of Fully Flexible Molecular Models.” *Molecular Simulation*, 29(8), 479–487.

Greenfield, M. L. (2011). “Molecular Modelling and Simulation of Asphaltenes and Bituminous Materials.” *International Journal of Pavement Engineering*, 12(4), 325–341.

Greenfield, M. L., and Zhang, L. (2009). *Final Report - Developing Model Asphalt Systems Using Molecular Simulation*. Kingston, RI.

Groenzin, H., and Mullins, O. C. (2000). “Molecular Size and Structure of Asphaltenes from Various Sources.” *Energy & Fuels*, American Chemical Society, 14(3), 677–684.

Hansen, J. S., Lemarchand, C. A., Nielsen, E., Dyre, J. C., and Schrøder, T. (2013). “Four-component United-atom Model of Bitumen.” *Journal of Chemical Physics*, 138(9), 5–13.

Henaut, I., Barre, L., Argillier, J.-F., Brucy, F., and Bouchard, R. (n.d.). “Rheological and Structural Properties of Heavy Crude Oils in Relation With Their Asphaltenes Content.” Society of Petroleum Engineers.

Hossain, M. I., and Tarefder, R. A. (2013). “Quantifying Moisture Damage at Mastic–Aggregate Interface.” *International Journal of Pavement Engineering*, 1–16.

Islam, R. M., Faisal, H. M., and Tarefder, R. A. (2015). “Determining Temperature and Time Dependent Poisson’s Ratio of Asphalt Concrete Using Indirect Tension Test.” *Fuel*, 146, 119–124.

Jiménez-Mateos, J. M., Quintero, L. C., and Rial, C. (1996). “Characterization of Petroleum Bitumens and Their Fractions by Thermogravimetric Analysis and Differential Scanning Calorimetry.” *Fuel*, 75(15), 1691–1700.

Jones, D. R. (1993). *SHRP Materials Reference Library: Asphalt Cements: A Concise Data Compilation (Vol. 1)*. Washington, DC: Strategic Highway Research Program, National Research Council.

Koots, J. A., and Speight, J. G. (1975). “Relation of Petroleum Resins to Asphaltenes.” *Fuel*, 54(3), 179–184.

Leach, A. R. (2001). *Molecular Modelling: Principles and Applications*. Prentice Hall.

Lemarchand, C. A., Bailey, N. P., Todd, B. D., Daivis, P. J., and Hansen, J. S. (2015). “Non-Newtonian Behavior and Molecular Structure of Cooee Bitumen under Shear Flow: A Non-equilibrium Molecular Dynamics Study.” *The Journal of Chemical Physics*, 142(244501), 1–17.

Lemarchand, C. A., Schrøder, T. B., Dyre, J. C., and Hansen, J. S. (2013). “Cooee Bitumen: Chemical Aging.” *Journal of Chemical Physics*, 139(12), 1–12.

Lemarchand, C. A., Schrøder, T. B., Dyre, J. C., and Hansen, J. S. (2014). "Cooee Bitumen . II . Stability of Linear Asphaltene Nanoaggregates." *Journal of Chemical Physics*, 141(144308), 1–15.

Lesueur, D. (2009). "The Colloidal Structure of Bitumen: Consequences on the Rheology and on the Mechanisms of Bitumen Modification." *Advances in Colloid and Interface Science*, Elsevier B.V., 145(1-2), 42–82.

Lesueur, D., Gerard, J., and Claudy, P. (1997). "Relationships Between the Structure and the Mechanical Properties of Paving Grade Asphalt Cements." *Journal of the Association of Asphat Paving Technologists*, 66, 486–507.

Lesueur, D., Gerard, J., Claudy, P., Letoffe, J., Planche, J., and Martin, D. (1996). "A Structure-Related Model to Describe Asphalt Linear Viscoelasticity." *Journal of Rheology*, 40(5).

Li, D. D., and Greenfield, M. L. (2014). "Chemical Compositions of Improved Model Asphalt Systems for Molecular Simulations." *Fuel*, Elsevier Ltd, 115, 347–356.

Lira-Galeana, C., and Hammami, A. (2000). "Wax Precipitation from Petroleum Fluids: A Review." *Developments in Petroleum Science*, T. F. Yen and G. V. Chilingarian, eds., Elsevier B.V., 557–608.

Lu, Y., and Wang, L. (2010). "Nanoscale Modelling of Mechanical Properties of Asphalt–Aggregate Interface Under Tensile Loading." *International Journal of Pavement Engineering*, 11(5), 393–401.

Ma, T., Huang, X., Mahmoud, E., and Garibaldy, E. (2011). “Effect of Moisture on the Aging Behavior of Asphalt Binder.” *International Journal of Minerals, Metallurgy, and Materials*, 18(4), 460–466.

Mannan, U. A., Islam, M. R., Weldegiorgis, M., and Tarefder, R. A. (2015). “Experimental Investigation on Rheological Properties of Recycled Asphalt Pavement Mastics.” *Applied Rhelogy*, 25(2), 1–13.

Mart ń-Martínez, F. J., Fini, E. H., and Buehler, M. J. (2015). “Molecular Asphaltene Models Based on Clar Sextet Theory.” *RSC Advances*, 5(1), 753–759.

Mason, T., and Lin, M. (2003). “Asphaltene Nanoparticle Aggregation in Mixtures of Incompatible Crude Oils.” *Physical Review E*.

Mayo, S. L., Olafson, B. D., and Goddard III, W. A. (1990). “DREIDING: A Generic Force Field for Molecular Simulations.” *The Journal of Chemical Physics*, 94(26), 8897–8909.

MOPAC 2012 Software Manual. (2012). Stewart Computational Chemistry, Colorado Springs.

MOPAC Guide. (2010). 2010 Schrodinger, LLC., Colorado Springs.

Mortazavi, M., and Moulthrop, J. S. (1993). *SHRP Materials Reference Library*. SHRP Report A-646. Washington, D.C.: Strategic Highway Research Program, National Research Council.

Mullins, O. C. (2010). “The Modified Yen Model †.” *Energy & Fuels*, 24(4), 2179–2207.

Murgich, J., Rodr ǵuez, and Aray, Y. (1996). “Molecular Recognition and Molecular Mechanics of Micelles of Some Model Asphaltenes and Resins.” *Energy & Fuels*, American Chemical Society, 10(1), 68–76.

Netzel, D. A., and Rovani, J. F. (2007). “Direct Separation and Quantitative Determination of (n -, Iso-)Alkanes in Neat Asphalt Using Urea Adduction and High-Temperature Gas Chromatography (HTGC) †.” *Energy & Fuels*, 21(1), 333–338.

Nicholls, J. C. (Ed.). (1998). *Asphalt surfacings*. CRC Press, New York, NY.

Olesiak, S. E., Oyen, M. L., and Ferguson, V. L. (2010). “Viscous-elastic-plastic Behavior of Bone Using Berkovich Nanoindentation.” *Mechanics of Time-Dependent Materials*, 14(2), 111–124.

Overfield, R. E., Sheu, E. Y., Sinha, S. K., and Liang, K. S. (1989). “SANS Study of Asphaltene Aggregation.” *Fuel Science and Technology International*, Taylor & Francis, 7(5-6), 611–624.

Oyen, M. L., and Cook, R. F. (2003). “Load – displacement behavior during sharp indentation of viscous – elastic – plastic materials.” *Journal of Materials Research*, 18(1), 139 – 150.

Pan, J., and Tarefder, R. A. (2015a). "Investigation of Asphalt Aging Behaviour Due to Oxidation Using Molecular Dynamics Simulation." *Molecular Simulation*, (August), 1–12.

Pan, J., and Tarefder, R. A. (2015b). "Behavior of Aged and Unaged Asphalt Binders Under Mechanical Loading Inside a Molecular Dynamic Simulation Box." *Transportation Research Board 94th Annual Meeting*, Washington, DC, Jan. 11th-15th.

Pan, J., and Tarefder, R. A. (2015c). "A Study of Temperature and Moisture Impacts on Asphalt Before and After Oxidation Using Molecular Dynamics Simulations." *Computational Materials Science*, Submitted(on June 30, 2015), Manuscript Number: COMMAT–D–15–01027.

Pan, J., Tarefder, R. A., and Mannan, U. A. (2016a). "Investigation of Oxidation Effect on the Properties of Asphalt under Different Temperatures Using Molecular Simulation and Laboratory Testing." *Transportation Research Board 95h Annual Meeting*, Washington, DC, Jan. 10th-14th, Paper Number: 16–5680.

Pan, J., Tarefder, R. A., and Hossain, M. I. (2016b). "A Study of Moisture Impacts on Asphalt Before and After Oxidation Using Molecular Dynamics Simulations." *In Transportation Research Record: Journal of the Transportation Research Board*, Submitted(on August 1, 2015), Paper Number: 16–5840.

Pan, T., Lu, Y., and Lloyd, S. (2012a). "Quantum-Chemistry Study of Asphalt Oxidative Aging: an XPS-Aided Analysis." *Industrial & Engineering Chemistry Research*, 51(23), 7957–7966.

Pan, T., Lu, Y., and Wang, Z. (2012b). "Development of an Atomistic-Based Chemophysical Environment for Modelling Asphalt Oxidation." *Polymer Degradation and Stability*, Elsevier Ltd, 97(11), 2331–2339.

Parker, F. (1996). *Residual Moisture in Hot Mix Asphalt Concrete*. Auburn University, Highway Research Center, Auburn, AL.

Petersen, J. C. (1984). "Chemical Composition of Asphalt as Related to Asphalt Durability: State of the Art." *Transportation Research Record*, Washington, DC, (999), 13–30.

Petersen, J. C. (1986). "Quantitative Functional Group Analysis of Asphalts Using Differential Infrared Spectrometry and Selective Chemical Reactions - Theory and Application." *Transportation Research Record*, Washington, DC, (1096), 1–11.

Petersen, J. C. (2009). *A Review of the Fundamentals of Aspahlt Oxidation: Chemical, Physicochemical, Physical Property, and Durability Relationships*. *Transportation Research E-Circular E-C140*, Transportation Research Board, Washington, DC.

Petersen, J. C., and Glaser, R. (2011). "Asphalt Oxidation Mechanisms and the Role of Oxidation Products on Age Hardening Revisited." *Road Materials and Pavement Design*, 12(4), 795–819.

Ravey, J. C., Ducouret, G., and Espinat, D. (1988). “Asphaltene Macrostructure by Small Angle Neutron Scattering.” *Fuel*, 67(11), 1560–1567.

Read, J., and Whiteoak, D. (2003). *The Shell Bitumen Handbook*. Thomas Telford Publishing, London.

Roberts, F. L., Prithvi, S., Kandhal, E., Brown, R., Dah-Yinn, L., and Kennedy, T. W. (1996). *Hot Mix Asphalt Materials, Mixture Design, and Constrution*. *Hot Mix Asphalt Materials, Mixture Design, and Constrution*, NAPA Research and Education Foundation, Lanham, MD.

Saether, E., Yamakov, V., and Glaessgen, E. H. (2009). “An Embedded Statistical Method for Coupling Molecular Dynamics and Finite Element Analyses.” *International Journal for Numerical Methods in Engineering*, 78(11), 1292–1319.

Schmidt, R., and Santucci, L. (1966). “A Practical Method for Determining the Glass Transition Temperature of Asphalts and Calculation of Their Low Temperature Viscosities.” *Assoc Asphalt Paving Technol Proc*.

Shenoy, A. (2002). “Model-fitting the Master Curves of the Dynamic Shear Rheometer Data to Extract a Rut-controlling Term for Asphalt Pavements.” *Journal of Testing and Evaluation*, American Society for Testing and Materials, 30(2), 95–102.

Sheppard, D., Terrell, R., and Henkelman, G. (2008). “Optimization methods for finding minimum energy paths.” *The Journal of chemical physics*, 128(13), 134106.

Simanzhenkov, V., and Idem, R. (2003). *Crude oil chemistry*. Marcel Dekker, Inc., New York, NY.

Solar, M., Meyer, H., Gauthier, C., Fond, C., Benzerara, O., Schirrer, R., and Baschnagel, J. (2012). "Mechanical Behavior of Linear Amorphous Polymers: Comparison Between Molecular Dynamics and Finite-Element Simulations." *Physical Review E*, 85(021808), 1–14.

Speight, J. G. (1999). *The Chemistry and Technology of Petroleum*. Marcel Dekker, Inc., New York.

Speight, J. G. (2004). "Petroleum Asphaltenes - Part 1: Asphaltenes, Resins and the Structure of Petroleum." *Oil & Gas Science and Technology*, 59(5), 467–477.

Stewart, J. J. P. (2013). "Optimization of Parameters for Semiempirical Methods VI: More Modifications to the NDDO Approximations and Re-optimization of Parameters." *Journal of Molecular Modeling*, 19(1), 1–32.

Storm, D. A., Edwards, J. C., DeCanio, S. J., and Sheu, E. Y. (1994). "Molecular Representations of Ratawi and Alaska North Slope Asphaltenes Based on Liquid- and Solid-State NMR." *Energy & Fuels*, American Chemical Society, 8(3), 561–566.

Tarefder, R. A., and Arisa, I. (2011). "Molecular Dynamic Simulations for Determining Change in Thermodynamic Properties of Asphaltene and Resin Because of Aging." *Energy & Fuels*, 25(5), 2211–2222.

Tarefder, R. A., and Faisal, H. (2013a). “Effects of Dwell Time and Loading Rate on the Nanoindentation Behavior of Asphaltic Materials.” *Journal of Nanomechanics and Micromechanics,* 3(2), 17–23.

Tarefder, R. A., and Faisal, H. M. (2013b). “Modeling Nanoindentation Creep Behavior of Asphalt Binder.” *Advances in Civil Engineering Materials, ASTM*, 2(1), 418–440.

Tarefder, R. A., Pan, J., and Hossain, M. I. (2015). “Molecular Dynamics Simulation of Asphaltic Material: Molecular Dynamics Simulations of Oxidative Aging of Asphalt Molecules under Stress and Moisture.” *Handbook of Research on Advanced Computational Techniques for Simulation-Based Engineering,* P. Samui, ed., IGI Global, Hershey, PA, USA (Accepted with Manuscript Number: 131114-042703).

Tarefder, R. A., and Yousefi, S. S. (2015). “Rheological Examination of Aging in Polymer-Modified Asphalt.” 04015112, 1–12.

Tarefder, R., and Faisal, H. (2013c). “Nanoindentation Characterization of Asphalt Concrete Aging.” *Journal of Nanomechanics and Micromechanics*, American Society of Civil Engineers, 4(1), A4013003.

Tildesley, D. J., and Allen, M. P. (1987). *Computer Simulation of Liquids*. Clarendon, Oxford.

Traxler, R. N. (1962). *Temperature-Viscosity Data on Asphalt Cements*. College Station, TX: Texas Transportatin Institute, A. & M. College of Texas.

Turner, T. F., and Branthaver, J. F. (1997). "DSC Studies of Asphalts and Asphalts Components." *Asphalt Science and Technology*, A. M. Usmani, ed., Marcel Dekker, Inc., New York, 59–101.

De Visscher, J., Soenen, H., Vanelstraete, A., and Redelius, P. (2004). "A Comparison of the Zero Shear Viscosity from Oscillation Tests and the Repeated Creep Test." *Proceedings of 3rd Eurasphalt & Eurobitume Congress*, 1501–1513.

Wu, H. A., Liu, G. R., Han, X., and Wang, X. X. (2006). "An Atomistic Simulation Method Combining Molecular Dynamics with Finite Element Technique." *Chaos, Solitons & Fractals*, 30(4), 791–796.

Yen, T. F. (1992). "The Colloidal Aspect of a Macrostructure of Petroleum Asphalt." *Fuel Science and Technology International*, Taylor & Francis, 10(4-6), 723–733.

Yen, T. F., Erdman, J. G., and Pollack, S. S. (1961). "Investigation of the Structure of Petroleum Asphaltenes by X-Ray Diffraction." *Analytical Chemistry*, American Chemical Society, 33(11), 1587–1594.

Zhang, L., and Greenfield, M. L. (2007a). "Analyzing Properties of Model Asphalts Using Molecular Simulation." *Energy & Fuels*, 21(3), 1712–1716.

Zhang, L., and Greenfield, M. L. (2007b). "Relaxation Time, Diffusion, and Viscosity Analysis of Model Asphalt Systems Using Molecular Simulation." *The Journal of Chemical Physics*, 127(194502), 1–13.

Zienkiewicz, O., and Taylor, R. (2000). *The Finite Element Method: Solid Mechanics*. Butterworth-Heinemann, Oxford.